

UiO : **University of Oslo**

Lars Magnus Valnes

# **Patient-specific Modeling of the Human Brain using Magnetic Resonance Imaging**

**Thesis submitted for the degree of Philosophiae Doctor**

Department of Mathematics

The Faculty of Mathematics and Natural Sciences

Department of Numerical Analysis and Scientific Computing  
Simula Research Laboratory



**2020**

© Lars Magnus Valnes, 2020

*Series of dissertations submitted to the  
Faculty of Mathematics and Natural Sciences, University of Oslo  
No. 2216*

ISSN 1501-7710

All rights reserved. No part of this publication may be  
reproduced or transmitted, in any form or by any means, without permission.

Cover: Hanne Baadsgaard Utigard.  
Print production: Representralen, University of Oslo.

# Preface

This thesis is submitted in partial fulfillment of the requirements for the degree of *Philosophiae Doctor* at the University of Oslo. The research presented here is conducted under the supervision of professor Kent-Andre Mardal, PhD Erika Lindstrøm, professor Per Kristian Eide, chief research scientist Marie E. Rognes and associate professor Unn Haukvik.

The thesis is a collection of three papers and a book excerpt that are presented in a practical order. The recurring theme is the usage of magnetic resonance imaging (MRI) in computational modeling of the human brain. The papers and the book excerpt are preceded by an introductory chapter that relates them together and provides background information and motivation for the work. The first and second paper cover interdisciplinary studies with MRI analysis performed by the author. Then, we have the book excerpt focusing on the approaches and software that were developed for this thesis and future work in bio-mechanical brain modeling. The third paper combines the first paper and the book excerpt into a computational relevant study.

## Acknowledgements

This thesis is the result of four years at Department of Mathematics. It has been a time with great colleagues, ski trips and social events. Firstly I would like to thank my supervisors, Kent-Andre Mardal, Erika Lindstrøm, Marie E. Rognes, Per Kristian Eide and Unn Haukvik. I would like to thank Marie E. Rognes and Simula Research Laboratory for arranging a weekly journal club that was interesting and educational for my thesis. Furthermore, I would like to thank PhD Travis Thompson for his efforts in co-writing the initial book manuscript. I would also like to thank PhD Anders Dale for providing guidance during my visits to his lab in San Diego. Next, I would like to thank my office neighbours, PhD Diako Darian and Tormod Landet for great company. Finally, I would like to thank my family and friends for unconditional support.

✿ **Lars Magnus Valnes**  
Oslo, December 2019



# List of Papers & Book Excerpt

## Paper I

Ringstad, G., Valnes, L. M., Dale, A. M., Pripp, A. H., Vatnehol, S.-A. S., Emblem, K. E., Mardal, K.-A., and Eide, P. K. “Brain-wide glymphatic enhancement and clearance in humans assessed with MRI”. in: *JCI insight* vol. 3, no. 13 (2018)

## Paper II

Eide, P. K., Valnes, L. M., Pripp, A. H., Mardal, K.-A., and Ringstad, G. “Delayed clearance of cerebrospinal fluid tracer from choroid plexus in idiopathic normal pressure hydrocephalus”. In: *Journal of Cerebral Blood Flow & Metabolism* (2019), p. 0271678X19874790

## Book Excerpt III

Kent-Andre Mardal, Marie E. Rognes, Travis B. Thompson and Lars M. Valnes ‘An introduction to meshing and mathematical modeling for the human brain: From magnetic resonance images to finite element simulations’.  
*in preparation for submission.*

## Paper IV

Lars Magnus Valnes, Sebastian K. Mitusch, Geir Ringstad, Per Kristian Eide, Simon W. Funke, Kent-Andre Mardal. ‘Can diffusion alone explain brain-wide distribution of CSF tracers within 24 hours?’  
*in preparation for submission.*

The published papers are reprinted with permission from <publisher(s)>. All rights reserved.



# Contents

|   |            |
|---|------------|
| Preface   | i          |
| List of Papers & Book Excerpt   | iii        |
| Contents  | v          |
| <b>1 Introduction</b>   | <b>1</b>   |
| 1.1 Motivation and aim . . . . .  | 1          |
| 1.2 Brain anatomy . . . . .   | 2          |
| 1.3 Normal pressure hydrocephalus . . . . .   | 6          |
| 1.4 Possible pathology of dementia . . . . .  | 6          |
| 1.5 Magnetic resonance imaging . . . . .  | 8          |
| 1.6 MRI in neuroscience . . . . .   | 9          |
| 1.7 Bio-mechanical modeling . . . . .   | 9          |
| 1.8 Porous media modeling . . . . .   | 13         |
| 1.9 Modeling of waste clearance . . . . .   | 14         |
| 1.10 Diffusion equation . . . . .   | 16         |
| 1.11 Extracellular diffusion modeling . . . . .   | 16         |
| 1.12 Finite element method . . . . .  | 17         |
| 1.13 Adjoint state method . . . . .   | 17         |
| 1.14 Computational geometries . . . . .   | 18         |
| 1.15 Summary of papers . . . . .  | 19         |
| 1.16 Other contributions . . . . .  | 25         |
| 1.17 Future work and outlook . . . . .  | 25         |
| References . . . . .  | 26         |
| <b>Papers &amp; Book Excerpt</b>  | <b>38</b>  |
| <b>I Brain-wide glymphatic enhancement and clearance in humans assessed with MRI</b>                                      | <b>39</b>  |
| <b>II Delayed clearance of cerebrospinal fluid tracer from choroid plexus in idiopathic normal pressure hydrocephalus</b> | <b>57</b>  |
| <b>III An introduction to basic meshing and mathematical modeling for the human brain</b>                                 | <b>69</b>  |
| <b>IV Can diffusion alone explain brain-wide distribution of CSF tracers within 24 hours?</b>                             | <b>163</b> |



# List of Abbreviations

|        |   |
|--------|---|
| ADC    | Apparent Diffusion Coefficient            |
| ASL    | Arterial Spin Labeling                    |
| CNS    | Central Nervous System                    |
| CSF    | Cerebrospinal Fluid                       |
| CT     | Computerized Tomography                   |
| DTI    | Diffusion Tensor Imaging                  |
| ECS    | Extracellular Space                       |
| EFV    | Endoscopic Fourth Ventriculostomy         |
| ETV    | Endoscopic Third Ventriculostomy          |
| FEM    | Finite Element Method                     |
| fMRI   | functional Magnetic Resonance Imaging     |
| FSI    | Fluid-Structure Interaction               |
| iNPH   | idiopathic Normal Pressure Hydrocephalus  |
| IPAD   | Intramural Perarterial Drainage           |
| ISF    | Interstitial Fluid                        |
| MRI    | Magnetic Resonance Imaging                |
| MPET   | Multi-network Poroelasticity Theory       |
| PC-MRI | Phase Contrast Magnetic Resonance Imaging |
| PDE    | Partial Differential Equations            |
| PVS    | Paravascular Space                        |
| REF    | Reference Group                           |
| SAS    | Subarachnoid Space                        |
| SMC    | Smooth Muscle Cells                       |
| SVMTK  | Surface Volume Meshing Toolkit            |
| VMTK   | Vascular Modelling Toolkit                |



# Chapter 1

## Introduction

### 1.1 Motivation and aim

Dementia is a devastating neurodegenerative disease that had an estimated global cost of 818 billion USD in 2015 [76]. It was estimated in [85] that the number of patients diagnosed with dementia in Europe will increase from 6 million in 2010 to 14 million in 2050. This makes dementia a major concern for the future health-care, and continued research can help to combat this trend.

Dementia research covers many different forms of research fields, for example genetics [53], clinical trials [132], and pharmacology [90]. The research often utilizes imaging techniques to visualize the brain, and larger studies often include patient cohorts by the hundreds. Thus, processing software have been used to analyze larger cohorts, for instance 1100 participants in [38]. The processing software also allows for accurate data comparison between studies, since it removes human bias and errors.

A new hypothesis has been proposed concerning the cause of dementia [62], and it suggests that dementia is essentially a fluid mechanical problem. Although controversial, this hypothesis is widespread, with over 1500 citations since it was published in 2012 [47], creating new avenues for bio-mechanical research of the brain.

The approach of computational bio-mechanics has become well established in cardiovascular research through the years, with studies modeling the heart [6], aneurysms [70] and blood clots [83]. Modeling can provide supplementary information that can be useful in evaluating problems in a clinical setting. The research has also developed tools and methods, which can be applied to other fields of bio-mechanics. Therefore, with the new hypothesis, it seems appropriate to establish and use bio-mechanical modeling in the brain.

Currently, there is a gap between bio-mechanical research and other research fields focusing on the brain, such as biochemistry and electrophysiology, which have been well established. In particular, the advanced imaging processing tools have not been fully utilized. Therefore, this thesis aims to shorten this gap, by introducing methods and proceedings that can be of aid. This thesis has three main objectives

- Use semi-automatic processing software with high-throughput to analyze data (Paper I and Paper II).
- Develop tools and approaches concerning medical images and processing software to make bio-mechanical models with patient-specific meshes for large cohorts (Book Excerpt III).

## 1. Introduction

---

- Make use of the developed tools and approaches to perform relevant bio-mechanical simulations (Paper IV).

The introduction will contain information that can be of use when reading this thesis. We will include a brief introduction to the brain anatomy, terminology and brain related characteristics in the next section. This will mainly be based on medical textbooks, but also referenced articles. Then, we will introduce two different waste clearing hypotheses by Iliff et al. [62] and Carare et al. [18].

We will provide a short introduction on the imaging technique magnetic resonance imaging (MRI), and on the MRI processing software FreeSurfer. However, these elements will be covered in more detail in Book Excerpt III. Finally, we will also describe the current state of bio-mechanical modeling and waste clearance in the brain.

### 1.2 Brain anatomy

In this section, we will go through some basic brain anatomy. We start with the brain anatomy and terminology, before continuing with the fluid flow in and around the brain. Most of the information provided in this section is from the medical textbook "Human Anatomy and Physiology" [78] if not otherwise specified.

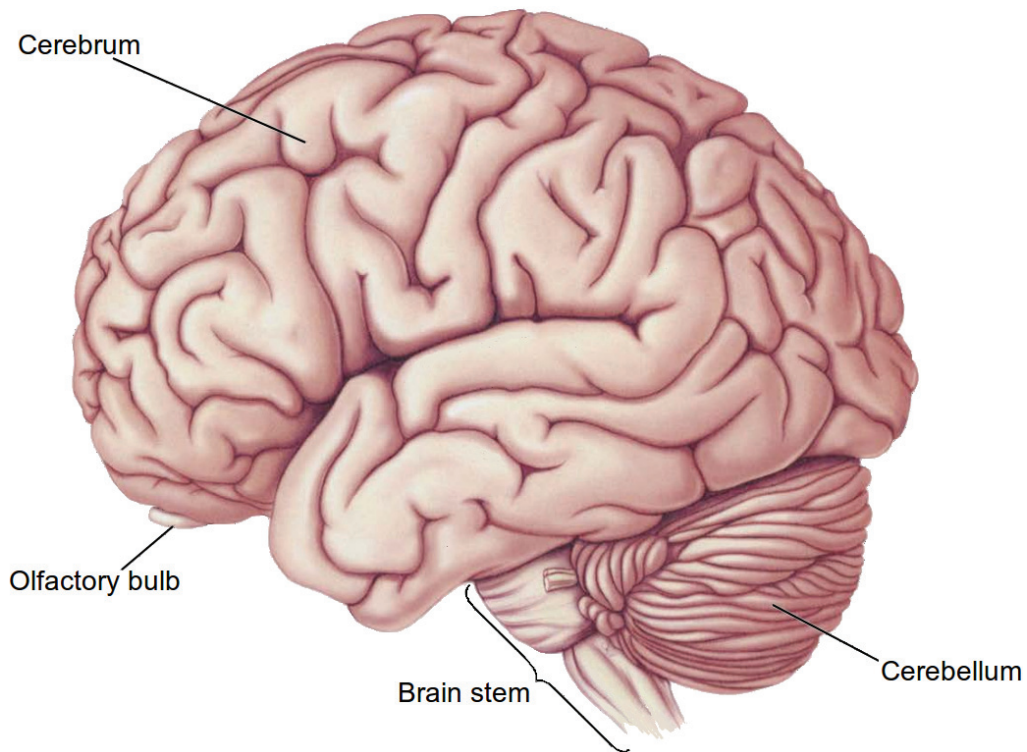


Figure 1.1: The image shows the main components of the brain: Cerebrum, Cerebellum and Brain stem. (Image taken from Bear [9])

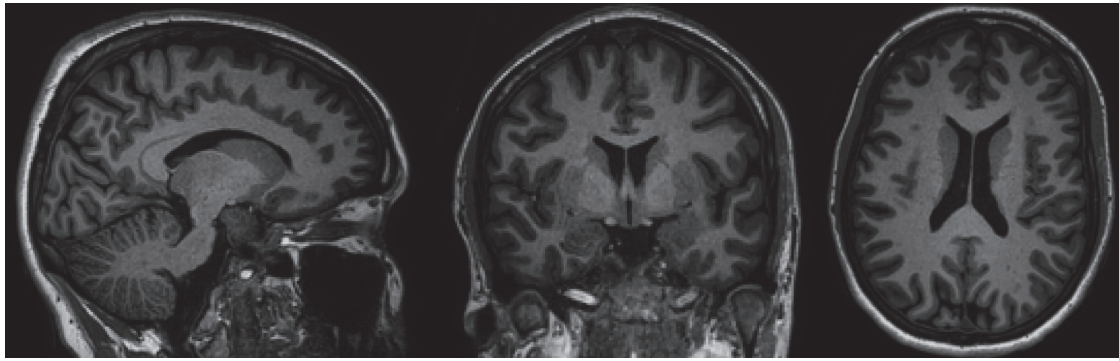


Figure 1.2: The image shows the different views dependent on the slice direction, ordered from left to right; sagittal view, coronal view and axial view.

The brain is an organ of the central nervous system (CNS), and consists of the cerebrum, the cerebellum and the brain stem, see Figure 1.1. The brain has high metabolism and constitutes up to 20% of the basal metabolism [82]. Furthermore, it receives 15% of the cardiac output and 20 % of total body basal oxygen consumption [109]. The brain together with the spinal cord makes up the human CNS.

The cerebrum is the largest part of the brain, and consists of two cerebral hemispheres. These hemispheres are joined at the brain stem, and are connected via commissural nerve tracts, with the largest being the corpus callosum. We divide each hemisphere into four regions; frontal, occipital, parietal and temporal lobe. Additionally, MRI brain images are represented as a collection of planar images slices of the brain, and the labeling of these slices is dependent on the slice direction, see Figure 1.2. The side-view of the brain is known as the sagittal view, the front view is known as the coronal view, and the above view is known as the axial view.

## Brain tissue

We distinguish between two types of tissue in the cerebrum, namely white and gray matter. The cortical gray matter is often referred to as the cerebral cortex, and is formed as a layer around the white matter. We also have sub-cortical gray matter, which is also found within the white matter and close to the brain stem. The sub-cortical gray matter consists of important structures, such as the basal ganglia, the hippocampus and amygdalae to name a few. In general, the gray matter tissue consists of neurons, arteries, veins and supportive glia cells, such as astrocytes and ependymal cells. The cerebral cortex has a unique structure with multiple folds, and the ridge and furrow are respectively known as gyrus and sulcus, see Figure 1.3.

In the white matter tissue we find axons, which connect the neurons in the gray matter. These axons create tracts inside the white matter, resulting in an anisotropic structure in the white matter [20]. We often denote the white and gray tissue as the brain parenchyma. The brain cells make up a solid structure in

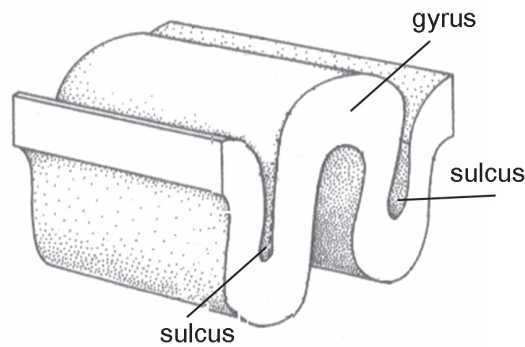


Figure 1.3: The image shows the folding of the cerebral cortex with sulcus and gyrus.(Image from Wikimedia Commons [130])

the tissue, and the narrow spaces between the cells are known as the extracellular space (ECS), which is filled with interstitial fluid (ISF).

### **Meninges**

The brain is protected by the skull and layers of meninges, which are located between the skull and the brain. The meninges consist of three membranes; the pial, the arachnoid and the dura, which are shown in Figure 1.4.

The region between the arachnoid and the pial membrane is known as the subarachnoid space (SAS). The SAS space is filled with cerebrospinal fluid (CSF), which consists of 99% water [17], and is important for regulating the brain functions [110]. The SAS stretches along the spine down to the lumbar region, and it is also connected to the ventricular system in the cerebrum through the cisterna magna.

### **Ventricular system**

The ventricular system consists of four connected compartments that are filled with CSF. These compartments are known as the two lateral, 3rd and 4th ventricles, as shown in Figure 1.5. Figure 1.5 also illustrates the perceived understanding of the CSF circulation in the brain. The production of CSF was estimated to be around 500 ml/day [49], and the CSF is thought to be mainly produced in the choroid plexus. The choroid plexus consists of blood vessels and specialized ependymal cells and is present in each of the ventricles. We will go in more detail about the functions of the choroid plexus in Paper II. In the traditional view by Cushing et al. [23], the CSF is produced by the choroid plexus in the lateral ventricles. It flows into the 3rd ventricle and into the cerebral aqueduct, which is the narrow channel between the 3rd and 4th ventricles. Then the CSF flows from the 4th ventricle and into the SAS, and is later absorbed by

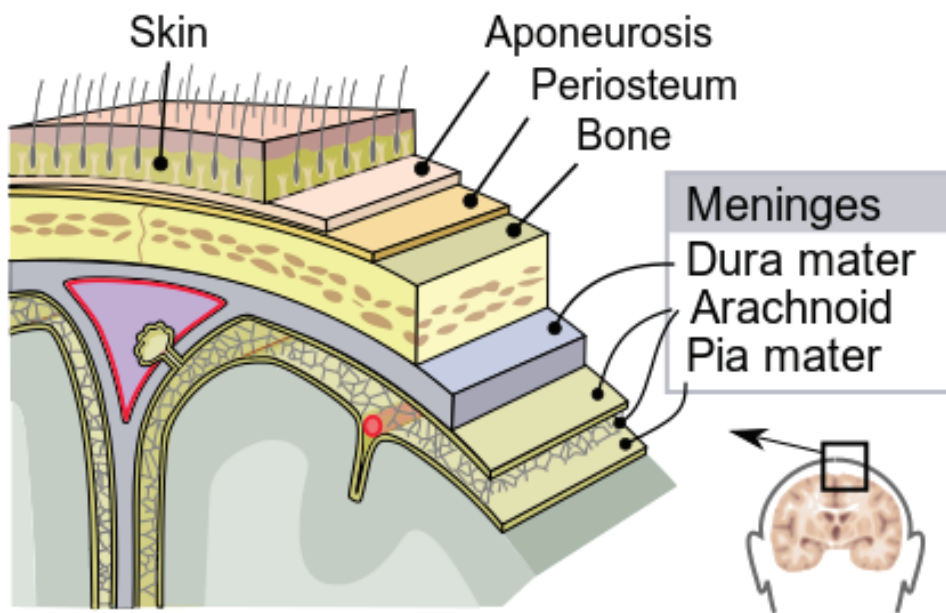


Figure 1.4: The image shows the structure from the skull to the cerebrum, including the meninges; dura mater, arachnoid and pia mater. (Image from Wikimedia Commons [130])

the arachnoid granulations near the upper skull, and also into superior sagittal sinus.

### Peri- and paravascular spaces

Peri- and paravascular spaces are small fluid-filled spaces that exist around the perforating vessels. These spaces are also called Virchow-Robin spaces after being described by Virchow [129] and Robin [99] in the middle of the 19th century, and knowledge has since improved and changed. The terms perivascular and paravascular are often used interchangeably, which can cause some confusion, since the terms can also describe two different types of fluid-filled pathways. In Bakker et al. [7], the perivascular space is described as a space within basement membrane between the smooth muscle cells (SCM) of arterioles and arteries. While the paravascular (PVS) describes the channels outside the SMC, enclosed by the pial membrane and glial limitans formed by astrocyte end feet, which separates the PVS from the brain parenchyma. The reported characteristic gap height of the PVS spaces is  $10\mu\text{m}$  [5, 87], while the basement membrane has a reported thickness of approximately  $100\text{ nm}$  [28, 105]. There is still some debate about the connection between the SAS and the PVS. In Iliff et al. [62], the SAS and PVS were reported to be separated by a thin pial sheet. While in the work of Bedussi et al. [10], the SAS and PVS were considered a single compartment, and the PVS were regions in the SAS with lower resistance to flow.

## 1. Introduction

---

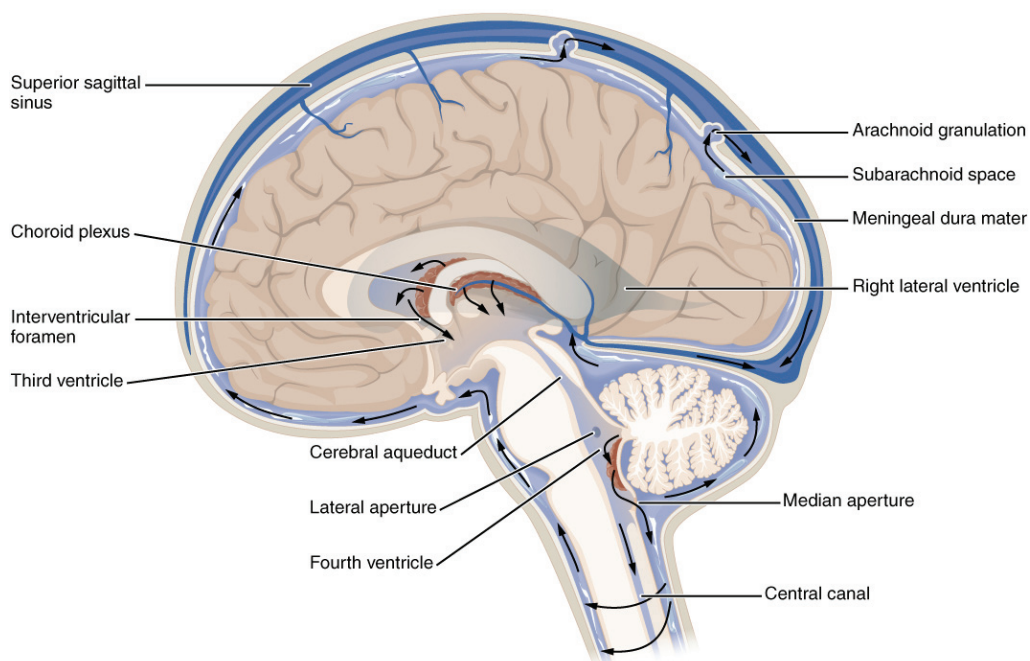


Figure 1.5: The image illustrates the traditional view by Cushing et al. [23] on the circulation of the CSF in and around the brain parenchyma. (Image from Wikimedia Commons [130])

### 1.3 Normal pressure hydrocephalus

In this thesis we will mainly focus on a patient-cohort, diagnosed with a subtype of dementia known as idiopathic Normal Pressure Hydrocephalus (iNPH). The disease is most common in elderly adults, with a reported prevalence of probable iNPH 21.9/100 000 in the general population, and 181.7/100 000 for the age-group 70-79 years [15]. Furthermore, it has similarities with other neurodegenerative diseases, such as Alzheimer’s disease [107]. Patients with iNPH have excess amounts of CSF in the lateral ventricles and that causes them to expand, shown in Figure 1.6. There are three symptoms associated with iNPH, namely gait disturbance, urinary incontinence and dementia [96].

Unlike most types of dementia, early onset of iNPH can be reversed, but requires surgery, known as shunting. The surgeon places a catheter in the lateral ventricles that drains the excess CSF into the abdomen. The patients with shunting surgery had a varied response rate from 15% to 98% [50, 123], and the mean rate of complications related to shunting was estimated to be 38% based on 44 articles [52]. Shunting surgery is highly risky, and finding a new bio-marker can greatly improve the shunting success rate.

### 1.4 Possible pathology of dementia

The cause of dementia and Alzheimer’s disease is still unknown, but studies have reported that Alzheimer’s disease is linked to the accumulation of harmful

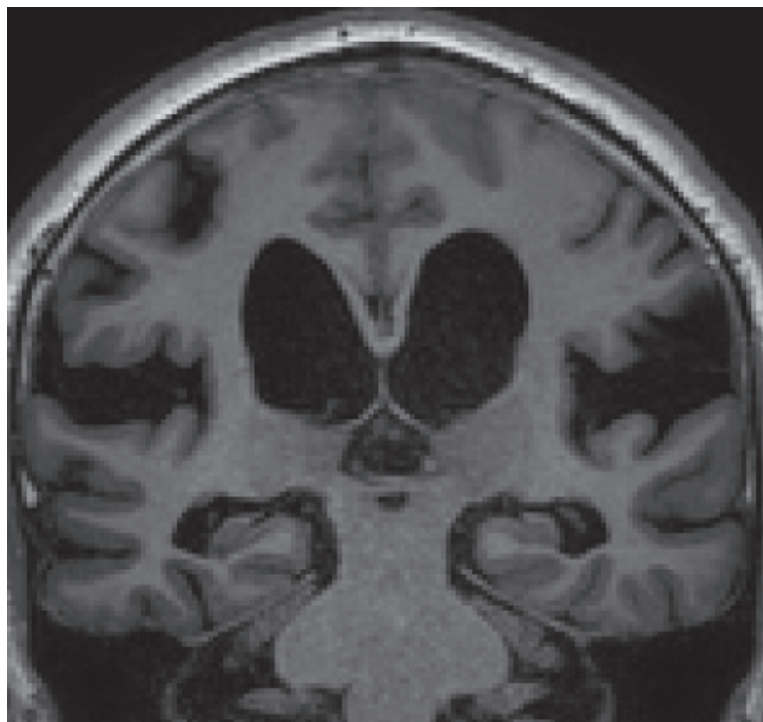


Figure 1.6: The image shows in a coronal MRI slice the enlarged ventricles of a person diagnosed with iNPH.

proteins, such as amyloid-beta and tau in the brain [8, 51]. This accumulation of amyloid-beta will create amyloid-beta plaques, which are believed to be responsible for the pathology of Alzheimer's disease. The presence of amyloid-beta plaques was detected in 42% of patients with possible iNPH [73], and 75% with severe iNPH dementia [46].

We produce these proteins as a by-product of the metabolism, but the proteins are normally cleared from the brain. In the rest of the body, the lymphatic vessels clear the waste proteins, but there are no lymphatic vessel in the brain parenchyma [2]. Since the brain has a high metabolism [82], there must be some mechanism for clearing the harmful waste proteins.

In 2012, Iliff et al. [61] proposed a new hypothesis of the waste clearance from the brain, denoted as the glia-lymphatic or "glymphatic" system. The paper details the observations that tracers injected into the cistern magna in the SAS, which quickly entered the cerebrum tissue, and similar observations was also reported by Rennels et al. [97] in 1985.

The proposed hypothesis [65] claims that there is a CSF influx in the PVS along the arteries in the brain. In the PVS, the CSF and ISF are mixed through low-resistant pathways known as astroglial AQP-4 channels. Then, in cerebrum tissue, a bulk flow in the ECS transports the waste from arterial capillaries to venous capillaries. The waste proteins are cleared along the paravenous spaces, the hypothesis is illustrated in Figure 1.7. The influx along the penetrating arteries have recently been supported by in-vivo observations in rats [80].

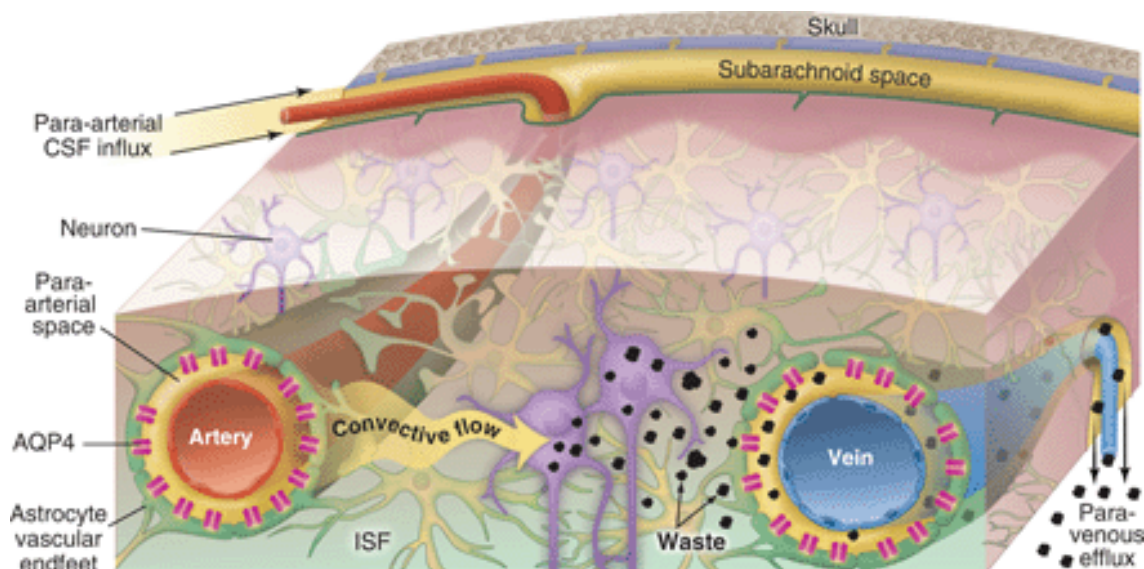


Figure 1.7: The image illustrates the waste clearance according to the glymphatic hypothesis. The glymphatic system works with the following process; a CSF influx from the SAS along the para-arterial space of an artery; mixing of CSF and ISF through AQP-4 channels; a convective flow from the artery to the vein that transports waste from the ECS to the paravenous space; clearing of waste from the brain parenchyma with a paravenous efflux. ( Image taken from Jessen et al. [65])

The glymphatic hypothesis suggests that dementia can be caused by insufficient clearing of waste from the brain parenchyma, such as amyloid-beta, which causes the creation of plaques. Thus, understanding the fluid interaction in the brain can help create new methods to counteract the progression of dementia. However, the waste clearance of the brain is still debated, and there are conflicting hypotheses. One of these hypotheses was based on the work of Carare et al. [18], and called the intramural periarterial drainage (IPAD). This hypothesis states that the waste and interstitial fluid are eliminated from the brain along the basement membranes of capillaries and arteries, thus along the periarterial space and not along the PVS. In this hypothesis, it is believed that Alzheimer's disease is caused by the stiffening of the arterial walls. This is mostly due to aging and arteriosclerosis, and causes the waste clearance of IPAD to fail. This leads to accumulation of amyloid-beta in the arterial walls, which is supported by observations of vascular deposition of the amyloid-beta protein in the perivascular spaces [68].

### 1.5 Magnetic resonance imaging

In this section, we will go through some basic principles of MRI, based on the books [9, 74]. Furthermore, we will only mention a few applications, since the applications will be more detailed in Book Excerpt III.

MRI is a tomographic technique, which uses a stable hydrogen nuclei as the source for obtaining information. This makes MRI preferable to other techniques, such as X-ray and computerized tomography (CT), which uses radiation to obtain information. The MRI technique utilizes the fact that the hydrogen nuclei has two energy states related to the magnetic moment of the nuclei. In general, these energy states are evenly distributed, but by applying a strong external magnetic field, the magnetic moments of the nuclei will become parallel after a time  $T_1$ , known as the longitudinal relaxation time. Then we use electromagnetic waves with the Larmor resonance frequency to excite hydrogen atoms so that we can measure the spatial distribution of hydrogen atoms. This causes the MRI-signal to have different signal values based on the hydrogen content, which makes it suitable to distinguish between different types of soft tissues, like gray and white matter.

MRI was introduced in the 1980's as a diagnostic tool, and has become important in diagnosing patients with neurodegenerative disease. The MRI technique has also provided different modalities of MRI images, such as T1-weighted MRI, functional-MRI (fMRI), Diffusion Tensor Imaging (DTI), Arterial Spin Labeling (ASL) and Phase Contrast MRI (PC-MRI), which provide additional information. As mentioned, we will go in more detail about the MRI modalities in Book Excerpt III.

## 1.6 MRI in neuroscience

The different modalities make MRI attractive for neuroscience, and since it is non-invasive, it allows for longitudinal studies with many participants. However, the manual analysis of a single participant can take a long time, therefore image analysis and software has been developed. Among the developed tools, we have 3D-Slicer [35], FSL [64], and FreeSurfer [37] to name a few.

The software FreeSurfer is a central part of this thesis, as analyzing tool and a starting point for developing additional tools for bio-mechanical modeling. FreeSurfer provides a highly autonomous process that divides the brain into different regions, displayed in Figure 1.8, called segmentation [27]. This makes it possible to effectively analyze larger data sets, and also removing the cognitive bias in the segmentation. Additionally, FreeSurfer can also be used for estimating the thickness of the cerebral cortex, longitudinal analysis, fMRI analysis and group analysis. This has contributed to the use of FreeSurfer in a variety of research, ranging from schizophrenia [111] and dementia [72] to mild traumatic brain injury [138].

## 1.7 Bio-mechanical modeling

Bio-mechanical modeling is a valuable resource that can provide a unique perspective on the understanding of human physiology. It helps medical doctors and researchers to evaluate surgical implants, to tailor new medical equipment and to determine the best possible treatment. This is based on the fact that

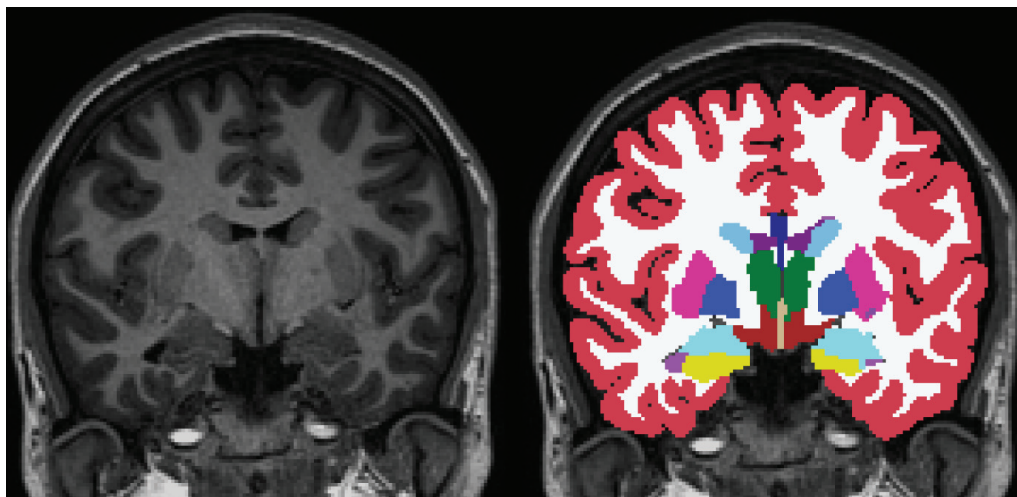


Figure 1.8: The image shows the automatic segmentation done by FreeSurfer.

computational models does not pose a risk to the patient and can effectively provide supplementary information that can be used for disease investigations and risk assessments.

The fundamental framework of bio-mechanical modeling has been detailed in the books by Fung [39, 40], who pioneered the field. This framework has since lead to bio-mechanics becoming a well-established tool in cardiovascular research with books by Quarteroni [93] and Holzapfel et al. [58] that detail the bio-mechanical methods for cardiovascular modeling.

Developed methods in cardiovascular modeling have dealt with similar mathematical difficulties that are currently present for brain modeling, such as fluid flow, fluid-structure interactions (FSI), medical parameters, boundary conditions and tissue modeling. Therefore, we will demonstrate bio-mechanical methods for brain modeling by using established cardiovascular models as reference. We will focus on models constructed using partial differential equations (PDE), which consist of unknown functions with multiple variables and their partial derivatives. PDEs are commonly used to model mechanical problems, such as fluid flow with incompressible Navier-Stokes equations and solid deformations with linear elasticity. We can solve PDEs with different methods, like finite differences, finite elements and finite volumes to name a few, which are well documented in the mathematical literature and a brief overview of the finite element method will be given in Section 1.12.

Soft tissue deformations are a central part of bio-mechanics, and in this section we will detail some of the developed models. The construction of tissue models requires solid mathematical foundation and we have two different types of theory for handling deformations; infinitesimal elasticity theory for small deformation and finite elasticity theory for larger deformations. For small deformations, soft tissue can be approximated with linear elasticity and the infinitesimal elasticity theory [113]. However, this is not the case for larger deformations of soft tissue, which exhibit non-linear mechanical properties. The mechanical properties of the

brain tissue have been investigated with experimental studies, and have reported that the brain tissue can be considered extremely soft, i.e highly non-linear and viscoelastic [16]. This is due to the fact that the brain tissue can be considered biphasic with 79% water by weight content [137] and exhibits hyperelastic properties [67]. The Ogden model is a hyperelastic model that is frequently used to model tissue by expressing the strain-energy as a non-linear summation of the principal stretches [89]. We also have more tailored models, such as the Holzapfel–Ogden model [59], which is used to model soft fiber tissue, for example the heart wall (myocardium) [131]. Furthermore, the water content in soft tissue makes it exhibit both fluid and solid mechanical behavior, like creep under constant load and relaxation under constant displacement. Therefore, viscoelastic tissue models have also been developed and used, for example the quasi-linear viscoelasticity model [41, 92] and generalized elastic-Maxwell model [56, 57, 136]. Developed soft tissue models have been used to simulate deformations in the brain tissue in [81, 84, 100].

In this thesis, we want to create a model for the waste clearance in the brain, and therefore we need to determine a model that will fit with the soft tissue deformations. The model will be used to investigate the waste clearance over several cardiac cycles, so the blood flow will cause deformations due to pressure differences in the brain. Previously, we described the brain as extremely soft, but the solid deformations in the brain during a cardiac cycle are small. This is based on recent measurements, which reported that the Young’s modulus for the brain is in the range 1-4.2 kPa [16, 67] and that the pulsatile pressure difference over a cardiac cycle within the brain did not exceed 50 Pa [128]. By Hooke’s Law, the maximum strain can be approximated to be around 0.05, which is in the regime of small deformations. Thus, we can model the waste clearance in the brain using linear elasticity and infinitesimal elastic theory. This means that we can simulate the flow and deformations in the brain with a linear poro-elastic model, which we will cover in Section 1.8.

Blood flow is frequently modeled in cardiovascular research, as it transports nutrients and waste throughout the human body. Hemorheology is the science field that covers blood flow and the interaction in a blood vessel. In [116] the blood flow was modeled using the incompressible Navier-Stokes equations and solved using the finite element method. We can adapt the blood flow models to simulate the CSF flow in the narrow channels in the brain, such as the cerebral aqueduct and the PVS. This can help us understand the consequences of CSF flow obstructions in the brain, such as aqueductal stenosis [21], Chiari malformation [30] and cysts [75], and evaluate different methods of treatment [69, 104, 125]. Recently, flow modeling in the ECS, PVS and periarterial spaces have become more popular due to the waste clearance hypothesis [28, 55, 106], which we will cover in Section 1.9.

Unlike fluid flow in pipes, the blood vessels consist of a tissue wall that deforms with the pulsative flow. This problem is also present in glymphatic hypothesis, as shown in Figure 1.7, with the PVS encapsulating the arteries. The method to include the solid deformation is known as fluid-structure interaction (FSI) modeling, and a typical FSI model was used in Crosetto et al. [22]. The

## 1. Introduction

---

study constructed a FSI model to simulate, using the finite element method, the blood flow and arterial wall deformation of a healthy aorta. It was reported that the simulation provided better comparison to experimental data than the usage of a rigid wall model. More complex FSI models exist, for example in Borazjani [13] FSI modeling was used to simulate the deformation in the heart during a cardiac cycle. This was done by combining the FSI model with a non-linear elastic model and simulated with the finite element method. Recently, FSI models were implemented to simulate CSF flow in the ECS by solid deformations in [126] and in the PVS due to arterial pulsation in [28]. These studies will be presented in more detail in Section 1.8 and Section 1.9, respectively.

Bio-mechanical models have been further developed with the intent of personalized medicine, which was covered in the review by Taylor et al. [115]. This review details general problems of patient-specific modeling, such as geometries, parameters and boundary conditions, and also highlights application areas like disease research, risk assessments, patient-specific device design and evaluation. Patient-specific risk assessment of aneurysms was studied in Gasser et al. [43] by evaluating the peak wall stress and peak wall rupture risk. This exemplifies that bio-mechanical models can help with assessing the medical situation, but we need methods to handle multiple patients. Large cohort studies have also been done with the risk assessment of the hemodynamics in cerebral artery aneurysms, with 38 aneurysms in [31] and 119 aneurysms in [135]. The first study used a processing software called the vascular modelling toolkit (VMTK) [4] that was developed with the purpose of making computational vascular geometries from medical images. We require similar processing software for the brain in order to perform larger cohort studies. This is in fact one of the aims of this thesis, and we will present the issue in Section 1.14, and more details in Book Excerpt III.

Bio-mechanical models need appropriate material parameters to provide meaningful information, and these parameters are often obtained from animal experiments and ex-vivo mechanical tests. However, mechanical properties in soft tissue may change over time because of aging and diseases, like stiffening (arteriosclerosis) of the arterial wall [79] and accumulation of plaques (atherosclerosis) in the arteries [134]. In this regard, elastography is a highly sought tool, since it allows for measuring mechanical properties in a non-invasive manner. Elastography works by applying a pressure wave into the soft tissue, measuring the response with a tomographic technique and estimating the mechanical properties based on the response. The method has been used with MR [101, 108] and ultrasound [25, 44] on different types of soft tissue, involving the brain [54]. The use of MR-elastography to obtain appropriate material properties may be important, since studies have reported stiffness changes in the brain due to neurodegenerative disease [86], such as multiple sclerosis [133], NPH [34] and different types of dementia [29].

Computer simulations can provide relevant information, but these require that the appropriate initial- and boundary conditions are considered. Boundary conditions for the Navier-Stokes equations include pressure or traction and prescribed velocity profiles at the boundary surface. In many cases, the reported values in the literature are sufficient. However, patient-specific measurements

can provide additional information that can be relevant. In Vinje et al. [128], it was reported that breathing had significant impact on the CSF flow in the cerebral aqueduct. This was investigated by modeling the fluid flow with Navier-Stokes in the cerebral aqueduct using idealized geometries and comparing to both PC-MRI measurements and patient-specific geometries. The study used pressure measurements obtained from two implanted sensors in the brain to impose the boundary conditions.

The measured quantities can also be composite variables, like the flux or the averaged flow rate. In Vignon-Clementel et al. [127] the average flow rate was mapped to a parabolic velocity profile and then used as the inlet boundary condition for the velocity. The appropriate material parameters and boundary conditions can be estimated by testing different values and comparing the results with observations. However, solving the inverse problem can be computationally expensive in terms of time, and variational data assimilation is an alternative.

Variational data assimilation constructs an optimization problem that tries to minimize the difference between the computational simulations and the observational data [19]. The minimization can be solved effectively by computing the descending gradient using the adjoint state method, and variational data assimilation methods have been used in cardiovascular research. In the work of Funke et al. [42] variational data assimilation was used to reconstruct the boundary conditions for blood flow in aneurysms. The assimilation robustness was tested by applying noise to the observations, and it was demonstrated that with appropriate regularization, the model accurately reconstructed the flow even with significant noise. In the work of Finsberg et al. [36], variational data assimilation was used to determine the mechanical properties in a patient-specific model of the heart. This was done for a cohort of patients with heart failure and compared with a healthy control group, and significant difference was reported in estimated contractility between the cohorts. The usage of variational data assimilation and brain modeling will be exemplified in Paper IV and the adjoint state method will be outlined in Section 1.13.

## 1.8 Porous media modeling

In this section, we will cover porous media modeling of brain. The solid deformation and fluid flow in porous media is often modeled using Biot's equations for linear poroelasticity, which are derived from the equations for linear elasticity, Darcy's law, Navier-Stokes and mass conservation. Biot's equations were built so that the solid and the fluid were mixed and existed within the same domain [12], which made it suitable for macroscopic model of porous tissue, like the brain.

Biot's equations can be used to model the brain, but it does not include the interaction between the different fluid compartments in the brain, like CSF, arteries, capillaries and veins. Therefore, in Vardakis et al. [125] a quasi-static extension of Biot's equations was presented and used for brain modeling, called the multi-network poroelasticity theory (MPET). The MPET model consists of momentum balance in the porous medium coupled with continuity equations for

each fluid compartment. The flow between different compartments is regulated by loading terms and it is assumed that the fluid compartments exist everywhere in the computational domain. The MPET model was used in Vardakis et al. [124] with an idealized geometry of the brain and four fluid compartments, CSF, arteries, capillaries and veins. This was done to demonstrate the effect of cerebral aqueduct stenosis and fluid outlet obstruction in 4th ventricle, and the treatment with endoscopic third (ETV) and endoscopic fourth ventriculostomy (EFV). The study concluded that the treatment of EFV was preferred over ETV.

MPET has also been combined with two patient-specific models in Guo et al. [48] to explore the risk factors of early onset of Alzheimer's disease by investigating obstructions of CSF transport. Measurements of the blood flow using ultrasound were used to impose boundary conditions on the arterial blood flow. The study gave detailed description of patient-specific modeling pipeline, with construction of computational meshes using MRI.

Recently, FSI has been implemented with the MPET model in [126] to investigate Alzheimer's disease effects on the hippocampus. The FSI model was used to simulate CSF flow causing solid deformations.

Analysis of the MPET was investigated in [71] by introducing the total pressure, and proved that the MPET was robust for a wide range of equation parameters. In [60] a similar MPET analysis also reported stability for the equation parameters, but used strongly mass-conservative discretizations to obtain the robustness.

### 1.9 Modeling of waste clearance

Waste clearance hypotheses are difficult to verify using in-vivo experiments with human brains, therefore computational models have been used to explore the mechanism of waste clearance. The models often focus on a single element of the waste clearance circulation, and focus mostly one hypothesis. We will look at modeling of the waste clearance hypothesis that involves solute transport in the PVS, periarterial space, SAS and in the ECS.

Solute transport in the ECS was modeled by solving the Navier-Stokes and convection-diffusion equation in Jin et al. [66] with a realistic geometry of the ECS. In the work of Holter et al. [55] the Stokes equations were solved using a specific geometry obtained by scanning a (4070nm, 3690nm, 4080nm) tissue cube from the cerebral cortex of a rat. Both studies tested the required pressure difference to obtain a bulk flow that could clear the waste proteins, and both concluded that the pressure difference required to transport the waste, was unlikely to occur in the ECS. Recently, in the work of Ray et al. [95] simulation was used to estimate the upper limit for superficial convective flow, which was found to be approximately  $50 \mu\text{m}/\text{min}$ . The paper suggests that bulk flow still can contribute in the transportation of large molecules, since the diffusivity decrease with increased molecular mass.

Studies have also investigated the peri- and paravascular spaces and the proposed methods on how the waste is actually cleared from the brain itself.

In the work of Faghieh et al. [32], the plausibility of bulk flow was studied in perivascular, paravascular and paravenous spaces. This was done using a one-dimensional branching model, and it was concluded that circulation driven by steady pressure was implausible in the current model. The study of Rey et al. [98] looked at the solute transport in the PVS by using resistance network model. It was concluded that the diffusion would dominate in the PVS, and contribution from bulk flow would be negligible.

The role of the arterial pulsation was addressed in the work of Iliff et al. [63], which suggests that arterial pulsation facilitates the interaction between the paravascular CSF and the ISF. Thus, several studies have investigated if arterial pulsation could be the driving force for solute transport, and the effect of local arterial pulsation in the spinal cords PVS was examined in Bilston et al. [11]. The fluid dynamics were modeled by the Navier-Stokes equation, and the arterial deformation was modeled as propagating wave resembling systolic pulsation. The study concluded that the arterial pulsation could induce fluid flow in the PVS in the propagating direction of arterial flow.

In Schley et al. [102], the waste clearance purposed by the IPAD hypothesis was investigated. The study used a thin-film flow approximation of incompressible Navier-Stokes equations with two arterial pulsation models; propagating pressure wave and oscillating pressure gradient. The results indicated that during each pulse cycle, the solutes and ISF were transported along the PVS in the reverse direction of the blood flow. In Diem et al. [28] the hypothesis that the arterial pulsations could drive IPAD was tested. For this study, the basement membrane was modeled as a porous medium and approximated with lubrication theory. The model also included a purposed valve mechanism of directional permeability in the porous medium that would ensure net flow in the opposite direction of the blood flow. It was demonstrated that the arterial pulsation created velocities significantly smaller than experimental observations.

Dispersion effects in the PVS were investigated in the work of Asgari et al. [5] with a modified Navier-Stokes equations with Darcy's law for the porous medium coupled with an advection-diffusion equation. The results showed 16% to 50% increase of solute transport in the PVS due to dispersion. Recently, the dispersion enhancement of solute transport in intrathecal, periarterial and paraarterial spaces was studied by Sharp et al. [105]. The study concluded that the solute transport would have a negligible enhancement in the periarterial space. In the PVS, the paraarterial space had more potential for enhancement, while the solute transport in the paravenous spaces was predicted to be unlikely due to low pulse pressure.

Recently, the IPAD hypothesis was tested with the addition of vasomotion of blood vessels in Aldea et al. [3]. Vasomotion describes the spontaneous oscillation in the blood vessel walls that is independent of the heart beat [1, 88]. The study used a porous-elastic model of the basement membrane with variable permeability, and a vascular tone wave was used to model the vasomotion. The study concludes that vasomotion driven IPAD is the only mechanism that could produce the resulting flow rates that could explain the current experimental observations.

It was reported in [14] that for experiments performed on rabbits, the CSF is drained into the cervical lymph nodes, located in the neck. This connects the SAS and the lymphatic system, which is a possible pathway for clearing waste transported from brain into the SAS. Patient-specific modeling of the CSF flow in the inferior cranial space of the SAS, which included the 4th ventricle and cerebral aqueduct, was done in [69]. The results demonstrated that there was negligible net flow over one cardiac cycle in the cerebral aqueduct. In Vinje et al. [128] the respiration was reported to be the main cause for fluid movement in the cerebral aqueduct, and not the arterial pulsation.

We have outlined studies that have modeled the waste clearance in the brain, and this was done by investigating the solute transport. The solute transport was first hypothesized to be caused by bulk flow, but the focus has since shifted to enhanced diffusion due to solid deformations. This was studied in the PVS with a FSI model, in the ECS and the periarterial space with a poro-elastic model. There are still questions regarding the strength of the diffusion enhancement, thus we will in Paper IV investigate if solute diffusion alone can explain the solute transport in the brain parenchyma.

### 1.10 Diffusion equation

We will model the transport of a solute using the diffusion equation with no convective flow. The diffusion equation can be derived from the continuity equation and Fick's first law. Fick's first law states that the transport of a solute is defined as

$$j = -D\nabla c \quad (1.1)$$

with  $c$  denoting the solute concentration,  $j$  the concentration flux and  $D$  the diffusion coefficient. Combined with the continuity equation

$$\frac{\partial c}{\partial t} + \nabla \cdot j = 0, \quad (1.2)$$

we can derive the diffusion equation

$$\frac{\partial c}{\partial t} = \nabla \cdot (D\nabla c). \quad (1.3)$$

### 1.11 Extracellular diffusion modeling

The CSF tracer analyzed in Paper I, gave a strong indication of a brain-wide waste clearance. This means that an evaluation of the glymphatic hypothesis can be done with a macroscopic model. The diffusion of solutes in the extracellular space has been studied in pharmacology, and an extensive framework with experimental verification was detailed in the seminal paper by Syková et al. [114].

In the seminal paper, the diffusion in a porous media is considered a hindered diffusion in the macroscale, with its own diffusion coefficient. This coefficient is

referred to as the effective or apparent diffusion coefficient (ADC), and it can be derived from experiments. The apparent and the free diffusion coefficients are related by

$$\lambda^2 = \frac{D_{free}}{D_{ADC}}, \quad (1.4)$$

with  $\lambda$  known as the tortuosity. The tortuosity is a material parameter, and it has been measured to be around 1.5-1.7 in the white matter tissue [114].

## 1.12 Finite element method

We will use the finite element method (FEM) with the software FEniCS [77] to solve (1.3). FEM is detailed in numerous books, for example [94], so we will only give a brief description of the fundamental steps for the method. It is a numerical method used for solving PDEs by constructing a linear system, which is done by finding the weak formulation and the discretization of the computational domain. We can find the weak formulation of a PDE by multiplying the equation with a partial continuous function, and doing integration by parts. The computational domain may exist in both a spatial and temporal sense, and the discretization of the temporal domain can for example be done with backwards Euler method. The spatial discretization with FEM consists of dividing the computational geometry into smaller elements, like tetrahedrons and cubes, which are connected by shared vertices. On each element, the PDE function is approximated with a polynomial, for example first order Lagrangian. Then, by utilizing the Gaussian quadrature rules, we can integrate the weak formulation over each element. The connections between elements make it possible to construct a linear system that we can solve with numerical methods. The details on modeling and solving the diffusion equation with FEniCS will be provided in Book Excerpt III.

## 1.13 Adjoint state method

In Paper IV we will exemplify the usage of variational assimilation with PDE-constraint optimization. PDE-constraint optimization methods have been well documented with several books, like [26], for minimizing a functional subjected to a PDE for a set of variables. The PDE may also depend on the optimization parameters, so it is preferable to use the reduced functional. Therefore, an effective method was needed for minimizing a reduced functional, and iterative optimization algorithms can do this with the descending gradient, like the conjugate gradient method. The numerical approximation of descending gradient, the tangent linear solutions, would require solving a linear system for each optimization variable, which can be computational expensive compared to the adjoint state method. The adjoint state method works by solving a single linear system to find the adjoint solution, which can be used to obtain the descending gradient. We used dolfin-adjoint [33] to construct and solve the adjoint problem.

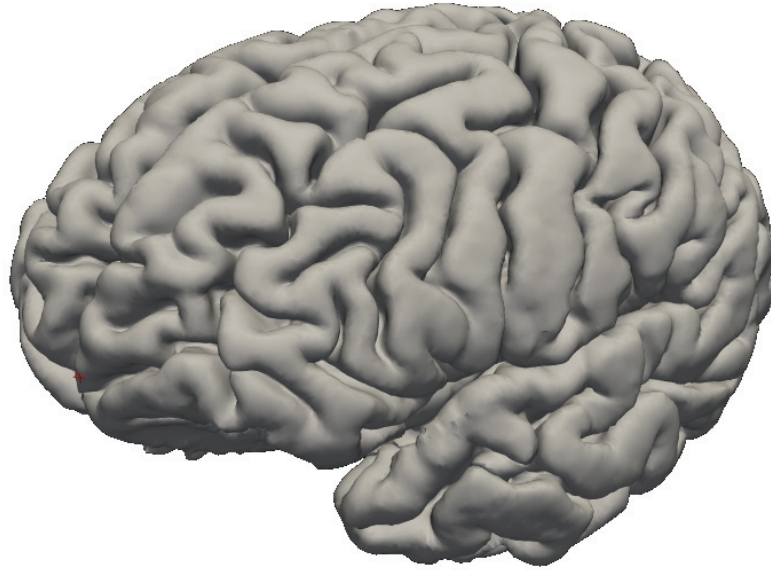


Figure 1.9: The image shows the left pial surface generated by FreeSurfer during the segmentation process.

### 1.14 Computational geometries

The FEM requires a computational grid (mesh) of smaller elements that represents an approximation of the geometry, and the cerebral cortex has a complex structure with gyri and sulci, see Figure 1.3. These details are hard to include in the mesh, and often require higher resolution to accurately depict. Furthermore, although the shape of the brain is similar between persons, there are possible anomalies such as cysts, tumors and obstructions that might impact the computational results. Therefore, creating patient-specific meshes were highly preferable, and methods to make high detailed meshes were investigated. The segmentation process in FreeSurfer generates surfaces of the white and cortical gray matter for each cerebral hemisphere that can be used to measure the cerebral cortex [24], see Figure 1.9. We considered these surfaces as the starting point for creating patient-specific volume meshes.

There are different programs that can be used for creating computational volume meshes, such as Gmsh [45], ITK [103] and previously mentioned VMTK. However, they are not specifically made for creating patient-specific computational mesh of the brain. Therefore, we developed a Python module called surface volume meshing tool-kit (SVMTK) [117] for this purpose and thesis. We developed the module with the intent of handling large cohorts with semi-automatic scripts to create computational meshes. The module offers an effective Python wrapping of necessary C++ functions and classes in the computational geometry algorithms library (CGAL) [91] to construct a volume mesh from surfaces. In our

case, these surfaces were created by FreeSurfer, and we combined these surface to create subdomains representing white and gray matter in the constructed mesh. However, the surfaces generated by FreeSurfer can be unsuitable for constructing meshes, and thus the module was made to handle different types of problems that can occur. These can for instance be; gray matter surfaces extending into the dura mater, non-anatomical features due to surface self-intersections, overlapping surfaces and sharp edges. We will go through the entire process in more detail in Book Excerpt III, including necessary repairing steps.

## 1.15 Summary of papers

### **Paper I: Brain-wide glymphatic enhancement and clearance in humans assessed with MRI**

Administration of drugs into the SAS can be a great opportunity to increase the effectiveness of the drug delivery. In fact, the administration of drugs intravenously has low success rate because of the blood-brain barrier and the fact that the blood vessels only occupy 3% of the brain. Thus intrathecal treatment may provide an effective method for drug delivery into the brain.

Animal studies have reported that there is communication between the SAS and the perivascular compartments of the brain. The observations in animal studies have not been translated to humans, and have not demonstrated enhancement in deep brain white matter.

The study consisted of 17 individuals that were divided into 2 cohorts. The first cohort was made of 8 individuals that were considered close to healthy and were used as a reference group (REF), while the second cohort had 9 patients who were diagnosed with iNPH. The participants were subjected to a baseline MRI scan before the CSF tracer was administrated with a lumbar puncture. Then, the participants underwent several MRI scans 1-2 hours after the injection, followed by MRI scans at 2-4 hours, 4-6 hours, 6-9 hours, 24 hours and up to 48 hours. The baseline MRI was segmented using the software FreeSurfer, and all MRIs for each participant were aligned to the baseline. This made it possible to measure signal change in several regions of the brain, and determine the presence of tracer using statistical analysis.

The results suggest a brain-wide clearance of the brain. Furthermore, there were some important differences between reference subjects and the patients with iNPH. The MRI of the reference participants indicated no tracer after 48 hours, but in iNPH there were still CSF tracer present after 48 hours.

In conclusion, the study demonstrated a brain-wide enrichment of a CSF tracer that was administered intrathecally in humans. The CSF tracer distributed centripetally from the cerebrum surface towards deeper structures

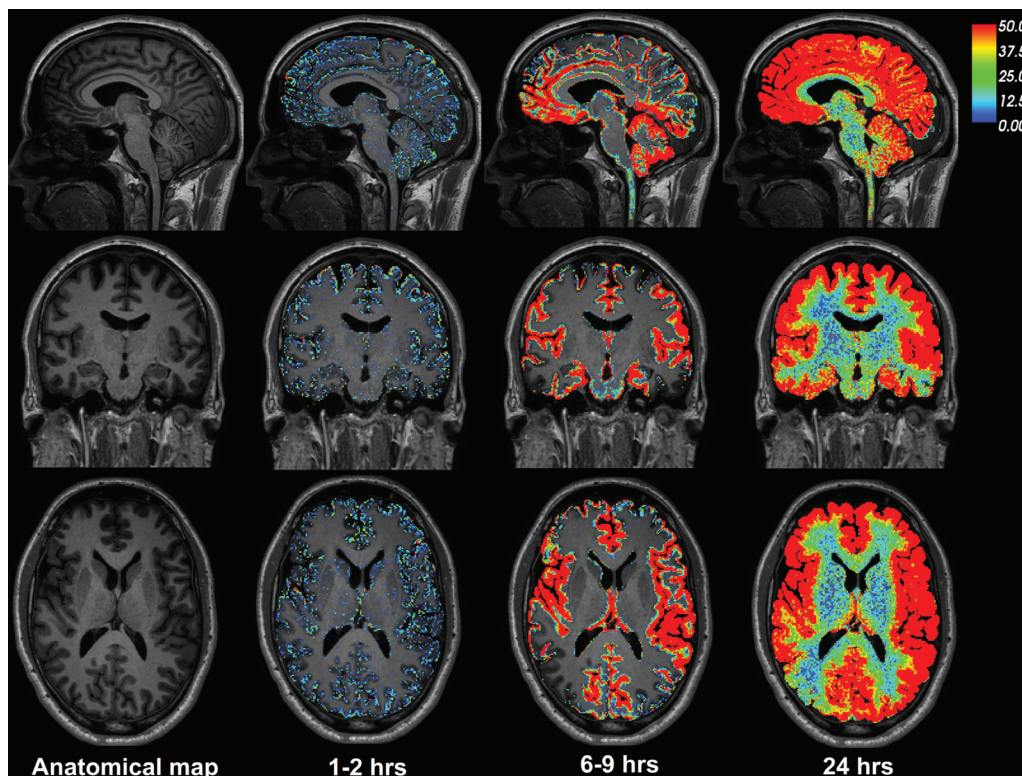


Figure 1.10: CSF tracer enrichment over time in one REF subject. The brain-wide enrichment of CSF tracer over time is shown for one REF individual. The percentage change in signal unit ratio is indicated at the color scale. CSF tracer enrichment occurred in a centripetal pattern at a rate exceeding the expected for pure diffusion, suggesting an important role of bulk flow for transport of substances through the brain.

in the brain. Vascular pulsations seem to play an important role for the tracer entry into the brain parenchyma. The delayed clearance of tracers from the brain parenchyma in patients diagnosed with iNPH, suggests that intrathecal contrast-enhanced MRI could be used to diagnose preclinical neurodegenerative diseases.

### **Paper II: Delayed clearance of cerebrospinal fluid tracer from choroid plexus in idiopathic normal pressure hydrocephalus**

Impaired clearance of amyloid-beta from choroid plexus is one proposed mechanism behind amyloid deposition in Alzheimer's disease. This study investigated if the clearance from choroid plexus is altered in iNPH patients by using CSF tracer as a surrogate marker of a metabolic waste product.

The study participants were divided into two cohorts, the first cohort consisted of 8 participants who were considered close to healthy and used as a reference group (REF), while the second cohort had 9 patients who were diagnosed with iNPH. The participants all started with a baseline MRI scan before the CSF tracer Gadovist was administered with a lumbar

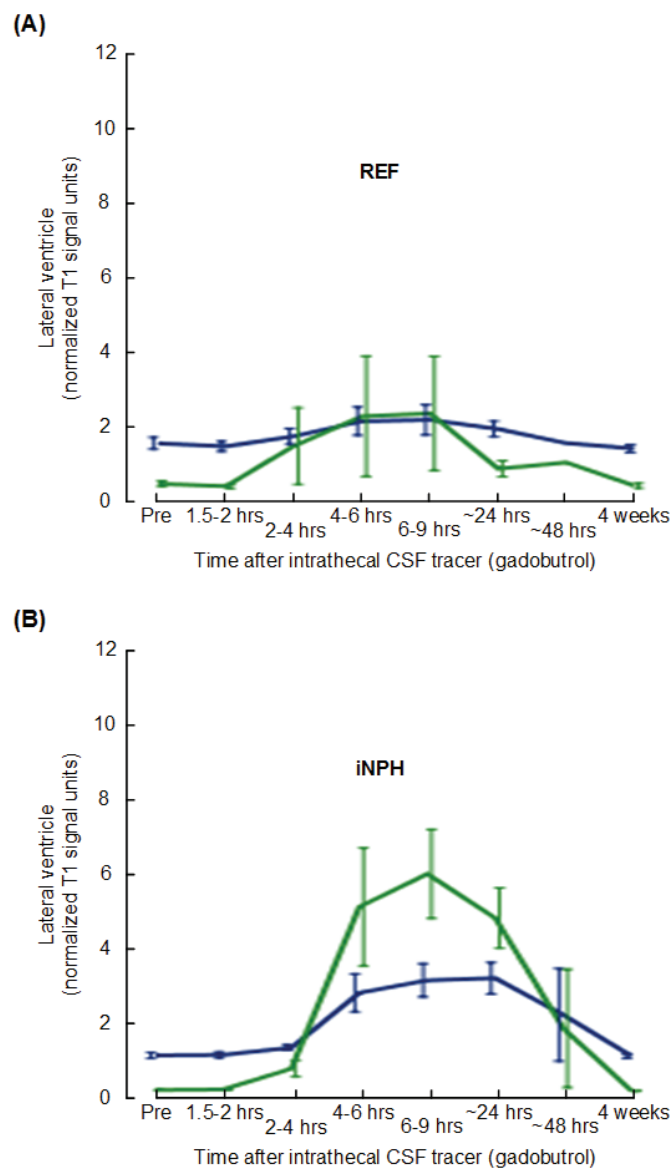


Figure 1.11: The images show CSF tracer enrichment in choroid plexus and CSF of lateral ventricle in the REF and iNPH cohorts. Trend plots of signal unit ratios are shown for choroid plexus (blue lines) and CSF (green lines) within lateral ventricle of (a) REF and (b) iNPH patients. The trend plots are shown as mean standard error.

puncture. Then, the participants underwent several MRI scans within 1-2 hours after the injection, followed by MRI scans in the time intervals 2-4 hours, 4-6 hours, 6-9 hours, 24 hours and up to 48 hours. The baseline MR images were segmented with the software FreeSurfer, and the MRI images for each participant were aligned with the baseline MRI. In cases with iNPH patients, T2-weighted MRI images were used to correct segmentation error in the lateral ventricles.

The results showed that the normalized T1 signal increased to the maximum values within the choroid plexus and the CSF in the lateral ventricles 6-9 hours after injection of gadobutrol. There were significant differences between the cohorts during the enhancement phase after 4-6 hours and 6-9 hours, and during the clearance phase at 24 hours after injection. In particular, the difference after 24 hours indicated that there was a delayed clearance of CSF tracer from the choroid plexus in iNPH.

In conclusion, the results suggest that the CSF tracer agent gadobutrol is absorbed by the choroid plexus. Furthermore, patients with iNPH had the CSF tracer cleared with a slower rate compared to the reference cohort. This suggests that neurodegeneration in iNPH may be caused by delayed CSF clearance of brain metabolism through the choroid plexus. There were discussions of a follow up computational study, like Paper IV for Paper I, to simulate the enrichment of the choroid plexus. However, no significant delay was observed between the enrichment of lateral ventricles and choroid plexus, which made it difficult to construct a computational model.

### **Book Excerpt III: An introduction to meshing and mathematical modeling for the human brain: From magnetic resonance images to finite element simulations**

This text is a book manuscript excerpt covering three chapters, numbered 2,3 and 4, which describes methods using MRI images to create computational models of the human brain. It consists of tools, code and data so that the reader can reproduce the results presented in the book, but the MRI data will not be provided in this excerpt, due to privacy requirements.

Chapter 2 begins with a mathematical introduction to the diffusion equation as a bio-mechanical model relating the different parameters to measurable data. We continue with a brief of brain anatomy, illustrated using MRI to familiarize the reader with the format. Then, we present some of the MRI modalities, and how it can be used in relation to the bio-mechanical modeling. The chapter finishes with an overview of the tools, like FreeSurfer and FEniCS, which were used throughout the book. This section includes a detailed installation guide with code and references.

Chapter 3 begins with the details of the procedure on how to create computational meshes from a T1-weighted MRI. T1-weighted MRI is used to create segmentation and surfaces by using the software FreeSurfer, but the resulting surfaces can have variable quality. Thus, we continue with different ways to improve the surfaces with SVMTK, which include smoothing, remeshing and boolean operations to name a few. Then we go through how the Python module SVMTK is used to create a volume mesh from the surfaces. The chapter ends with a detailed example on the computational modeling of the diffusion equation with the produced volume mesh, and a detailed description on the implementation of SVMTK.

Chapter 4 details the procedure to create a mesh with multiple subdomains. This procedure uses the surfaces of the cerebral cortex and the white matter



Figure 1.12: The image shows a clip of the mesh constructed using the pial and white surfaces for each hemisphere, with the lateral ventricles removed.

of each hemisphere generated by FreeSurfer. The lateral ventricle surfaces are not automatically produced by FreeSurfer, therefore the chapter will cover this procedure in detail. Then, we will go through the subdomain function and how to assign each subdomain with an integer tag. The chapter will also cover how to remove a subdomain from the volume mesh, like the lateral ventricles. The last section covers the methods to convert the subdomain cell marking and the facet marking between subdomains into FEniCS using mesh conversion tools.

#### **Paper IV: Can diffusion alone explain brain-wide distribution of CSF tracers within 24 hours?**

Waste clearance of the brain has received more attention after the hypothesis of the glymphatic system. The hypothesis links neurodegenerative diseases, like Alzheimer's disease and iNPH, to the inadequate clearance of harmful proteins from the brain parenchyma.

The waste clearance in the glymphatic hypothesis is based on the transportation of waste through a bulk flow in extracellular space in the brain. Recently, computational studies looked at the possibility of bulk flow in extracellular and paravascular spaces, and the results indicate that a bulk flow was very unlikely. Thus, the purpose for this paper is to explore if the CSF tracer distribution seen in Paper I can be explained by diffusion alone.

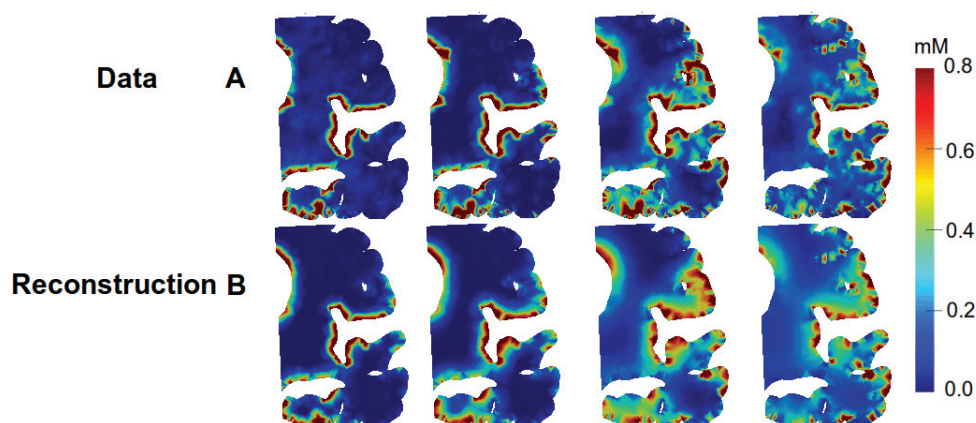


Figure 1.13: The image displays observations from MR images and computational reconstruction of the same observations at time-points 2 hours, 6 hours, 24 hours and 48 hours after the first observation with MRI contrast agent. Row A) shows the MRI observations. Row B) shows the reconstructed observations with  $\alpha = 0.0001$ ,  $\beta = 10.0$ ,  $\gamma = 1.0$  and 48 time-steps. The color-bar was restricted to the range (0.0-0.8) .

This study obtained brain MRI observation of CSF tracer in one patient diagnosed with iNPH at several time points. Boundary constrained PDE optimization was selected to compute the ADC based on the MRI observations. The optimization was done by minimizing a functional that was constructed with three regularization parameters; spatial, temporal and gradient regularization. The finite element method software FEniCS in combination with dolfin-adjoint was used to solve the problem, and meshes were constructed using the baseline MRI.

The robustness of the method was tested using a synthetic test case with a large range of computational parameters, which also included adding artificial noise to the manufactured simulations. Additionally, methods for reducing the noise in the MRI data were also tested with Gaussian smoothing and value projection onto the boundary. We estimated the concentration distributions based on MR images obtained at different points in times. The method was used with the concentration distributions to compute the ADC for gray and white matter, which was compared with the ADC estimated with free diffusion coefficient and the tortuosity obtained from DTI.

The results of the synthetic test case showed high accuracy reconstruction of the ADC and robustness to noise. The results were consistent for a large range of regularization parameters and showed good convergence in the relative error to less than 5%. ADC computed with the MRI observation were  $2.2 \times 10^{-4} \text{ mm}^2/\text{s}$  in the white matter and  $1.8 \times 10^{-4} \text{ mm}^2/\text{s}$  in the gray matter. These values were compared to the ADC estimated using

DTI, which were  $1.10 \times 10^{-4}$  mm<sup>2</sup>/s in white matter and  $1.26 \times 10^{-4}$  mm<sup>2</sup>/s in gray matter. As an effect of the Gaussian smoothing, the computed ADC in the gray matter was on average 250% times higher than ADC estimated using DTI. While the values in the white matter were more consistent, the method of projecting values onto the boundary gave ADC of 5% lower ADC than estimated with DTI.

In conclusion, the methodology was tested with a synthetic test case and the results showed robustness for a large range of parameters and noise. The computed ADC in gray matter and the white matter were respectively 23% and 82% higher than the estimated ADC using DTI, indicating enhancement of solute transport. This could be due to the iNPH diagnosis of the patient, which caused large variance of values in the DTI. Therefore, the next step is to determine to what extent the methodology is able to discriminate between healthy and impaired clearance.

## 1.16 Other contributions

In addition to the presented papers and the book excerpt, the PhD also included co-authoring the following articles [111, 112, 128] proceedings [112], poster presentation [118], oral presentation at international conferences [119, 122] and at national workshops [120, 121].

## 1.17 Future work and outlook

In this thesis, we used MRI processing software FreeSurfer, which we later combined with bio-mechanical modeling. Although we have covered the objectives of this thesis, there is still a gap between bio-mechanical brain modeling and other bio-mechanical fields of modeling. Therefore, we will in this section cover some of the future additions and improvements. The papers Paper I and Paper II had 17 participants, so increasing the number of participants would be a natural step forward. There are also other improvements possible, such as the distribution of MRI during the first 48 hours period. This can be more difficult to achieve, due to logistics, but optimization of the scan times can provide more information. In the Book Excerpt III, we detailed the process of making a patient-specific geometry, but we did not include different MRI modalities, like elastography and DTI, in the computational model. Therefore, the next step should aim at including different MRI modalities to bio-mechanical model. This presents another problem of MRI resolution that is dependent on the MRI modality. Therefore, we need to have a proper approach to combining different MRI modalities. The methodology presented in Paper IV was only applied to a single person, thus the next step would involve applying the same methodology on two different cohorts, a reference cohort and an iNPH cohort, to see if the methodology can discriminate between the cohorts.

### References

- [1] Aalkjær, C., Boedtkjer, D., and Matchkov, V. “Vasomotion—what is currently thought?” In: *Acta Physiologica* vol. 202, no. 3 (2011), pp. 253–269.
- [2] Abbott, N. J. “Evidence for bulk flow of brain interstitial fluid: significance for physiology and pathology”. In: *Neurochemistry international* vol. 45, no. 4 (2004), pp. 545–552.
- [3] Aldea, R. et al. “Cerebrovascular smooth muscle cells as the drivers of intramural periarterial drainage of the brain”. In: *Frontiers in aging neuroscience* vol. 11 (2019), p. 1.
- [4] Antiga, L. et al. “An image-based modeling framework for patient-specific computational hemodynamics”. In: *Medical & biological engineering & computing* vol. 46, no. 11 (2008), p. 1097.
- [5] Asgari, M., De Zélicourt, D., and Kurtcuoglu, V. “Glymphatic solute transport does not require bulk flow”. In: *Scientific reports* vol. 6 (2016), p. 38635.
- [6] Baccani, B. et al. “Fluid dynamics of the left ventricular filling in dilated cardiomyopathy”. In: *Journal of biomechanics* vol. 35, no. 5 (2002), pp. 665–671.
- [7] Bakker, E. N. et al. “Lymphatic clearance of the brain: perivascular, paravascular and significance for neurodegenerative diseases”. In: *Cellular and molecular neurobiology* vol. 36, no. 2 (2016), pp. 181–194.
- [8] Ballatore, C., Lee, V. M.-Y., and Trojanowski, J. Q. “Tau-mediated neurodegeneration in Alzheimer’s disease and related disorders”. In: *Nature Reviews Neuroscience* vol. 8, no. 9 (2007), p. 663.
- [9] Bear, M. F. *Neuroscience : exploring the brain*. eng. 3rd ed. Philadelphia: Lippincott Williams & Wilkins, 2007.
- [10] Bedussi, B. et al. “Paravascular channels, cisterns, and the subarachnoid space in the rat brain: a single compartment with preferential pathways”. In: *Journal of Cerebral Blood Flow & Metabolism* vol. 37, no. 4 (2017), pp. 1374–1385.
- [11] Bilston, L. E. et al. “Arterial pulsation-driven cerebrospinal fluid flow in the perivascular space: a computational model”. In: *Computer Methods in Biomechanics & Biomedical Engineering* vol. 6, no. 4 (2003), pp. 235–241.
- [12] Biot, M. A. “General theory of three-dimensional consolidation”. In: *Journal of applied physics* vol. 12, no. 2 (1941), pp. 155–164.
- [13] Borazjani, I. “Fluid–structure interaction, immersed boundary-finite element method simulations of bio-prosthetic heart valves”. In: *Computer Methods in Applied Mechanics and Engineering* vol. 257 (2013), pp. 103–116.

- 
- [14] Bradbury, M., Cserr, H., and Westrop, R. “Drainage of cerebral interstitial fluid into deep cervical lymph of the rabbit”. In: *American Journal of Physiology-Renal Physiology* vol. 240, no. 4 (1981), F329–F336.
- [15] Brean, A. and Eide, P. “Prevalence of probable idiopathic normal pressure hydrocephalus in a Norwegian population”. In: *Acta neurologica Scandinavica* vol. 118, no. 1 (2008), pp. 48–53.
- [16] Budday, S. et al. “Mechanical characterization of human brain tissue”. In: *Acta biomaterialia* vol. 48 (2017), pp. 319–340.
- [17] Bulat, M. and Klarica, M. “Recent insights into a new hydrodynamics of the cerebrospinal fluid”. In: *Brain research reviews* vol. 65, no. 2 (2011), pp. 99–112.
- [18] Carare, R. et al. “Solutes, but not cells, drain from the brain parenchyma along basement membranes of capillaries and arteries: significance for cerebral amyloid angiopathy and neuroimmunology”. In: *Neuropathology and applied neurobiology* vol. 34, no. 2 (2008), pp. 131–144.
- [19] Chabiniok, R. et al. “Multiphysics and multiscale modelling, data–model fusion and integration of organ physiology in the clinic: ventricular cardiac mechanics”. In: *Interface focus* vol. 6, no. 2 (2016), p. 20150083.
- [20] Chenevert, T. L., Brunberg, J. A., and Pipe, J. G. “Anisotropic diffusion in human white matter: demonstration with MR techniques in vivo.” In: *Radiology* vol. 177, no. 2 (1990), pp. 401–405.
- [21] Cinalli, G. et al. “Failure of third ventriculostomy in the treatment of aqueductal stenosis in children”. In: *Journal of neurosurgery* vol. 90, no. 3 (1999), pp. 448–454.
- [22] Crosetto, P. et al. “Fluid–structure interaction simulation of aortic blood flow”. In: *Computers & Fluids* vol. 43, no. 1 (2011), pp. 46–57.
- [23] Cushing, H. et al. “The third circulation and its channels”. In: *Lancet* vol. 2 (1925), pp. 851–857.
- [24] Dale, A. M., Fischl, B., and Sereno, M. I. “Cortical surface-based analysis: I. Segmentation and surface reconstruction”. In: *Neuroimage* vol. 9, no. 2 (1999), pp. 179–194.
- [25] De Korte, C. L. and Van Der Steen, A. F. “Intravascular ultrasound elastography: an overview”. In: *Ultrasonics* vol. 40, no. 1-8 (2002), pp. 859–865.
- [26] De los Reyes, J. C. *Numerical PDE-constrained optimization*. Springer, 2015.
- [27] Desikan, R. S. et al. “An automated labeling system for subdividing the human cerebral cortex on MRI scans into gyral based regions of interest”. In: *Neuroimage* vol. 31, no. 3 (2006), pp. 968–980.
- [28] Diem, A. K. et al. “Arterial pulsations cannot drive intramural periarterial drainage: significance for A $\beta$  drainage”. In: *Frontiers in neuroscience* vol. 11 (2017), p. 475.

- [29] ElSheikh, M. et al. “MR elastography demonstrates unique regional brain stiffness patterns in dementias”. In: *American Journal of Roentgenology* vol. 209, no. 2 (2017), pp. 403–408.
- [30] Elster, A. D. and Chen, M. “Chiari I malformations: clinical and radiologic reappraisal.” In: *Radiology* vol. 183, no. 2 (1992), pp. 347–353.
- [31] Evju, Ø. et al. “Robustness of common hemodynamic indicators with respect to numerical resolution in 38 middle cerebral artery aneurysms”. In: *PloS one* vol. 12, no. 6 (2017), e0177566.
- [32] Faghih, M. M. and Sharp, M. K. “Is bulk flow plausible in perivascular, paravascular and paravenous channels?” In: *Fluids and Barriers of the CNS* vol. 15, no. 1 (2018), p. 17.
- [33] Farrell, P. E. et al. “Automated derivation of the adjoint of high-level transient finite element programs”. In: *SIAM Journal on Scientific Computing* vol. 35, no. 4 (2013), pp. C369–C393.
- [34] Fattahi, N. et al. “MR elastography demonstrates increased brain stiffness in normal pressure hydrocephalus”. In: *American Journal of Neuroradiology* vol. 37, no. 3 (2016), pp. 462–467.
- [35] Fedorov, A. et al. “3D Slicer as an image computing platform for the Quantitative Imaging Network”. In: *Magnetic resonance imaging* vol. 30, no. 9 (2012), pp. 1323–1341.
- [36] Finsberg, H. et al. “Estimating cardiac contraction through high resolution data assimilation of a personalized mechanical model”. In: *Journal of computational science* vol. 24 (2018), pp. 85–90.
- [37] Fischl, B. “FreeSurfer”. In: *Neuroimage* vol. 62, no. 2 (2012), pp. 774–781.
- [38] Fjell, A. M. et al. “Accelerating cortical thinning: unique to dementia or universal in aging?” In: *Cerebral cortex* vol. 24, no. 4 (2012), pp. 919–934.
- [39] Fung, Y.-c. *Biomechanics: mechanical properties of living tissues*. Springer Science & Business Media, 2013.
- [40] Fung, Y.-c. *Biomechanics: motion, flow, stress, and growth*. Springer Science & Business Media, 2013.
- [41] Fung, Y.-C. B. “Stress-strain-history relations of soft tissues in simple elongation”. In: *Biomechanics its foundations and objectives* (1972), pp. 181–208.
- [42] Funke, S. W. et al. “Variational data assimilation for transient blood flow simulations: Cerebral aneurysms as an illustrative example”. In: *International journal for numerical methods in biomedical engineering* vol. 35, no. 1 (2019), e3152.
- [43] Gasser, T. C. et al. “Biomechanical rupture risk assessment of abdominal aortic aneurysms: model complexity versus predictability of finite element simulations”. In: *European Journal of Vascular and Endovascular Surgery* vol. 40, no. 2 (2010), pp. 176–185.

- 
- [44] Gennisson, J.-L. et al. “Ultrasound elastography: principles and techniques”. In: *Diagnostic and interventional imaging* vol. 94, no. 5 (2013), pp. 487–495.
- [45] Geuzaine, C. and Remacle, J.-F. “Gmsh: A 3-D finite element mesh generator with built-in pre-and post-processing facilities”. In: *International journal for numerical methods in engineering* vol. 79, no. 11 (2009), pp. 1309–1331.
- [46] Golomb, J. et al. “Alzheimer’s disease comorbidity in normal pressure hydrocephalus: prevalence and shunt response”. In: *Journal of Neurology, Neurosurgery & Psychiatry* vol. 68, no. 6 (2000), pp. 778–781.
- [47] *Google Scholar*. <https://scholar.google.com>. Accessed: 19-September-2019.
- [48] Guo, L. et al. “Subject-specific multi-poroelastic model for exploring the risk factors associated with the early stages of Alzheimer’s disease”. In: *Interface focus* vol. 8, no. 1 (2017), p. 20170019.
- [49] Guyton, A. C. and Hall, J. E. “Textbook of medical physiology. 11th”. In: *WB Saunders Company, Philadelphia* (2006).
- [50] Halperin, J. J. et al. “Practice guideline: Idiopathic normal pressure hydrocephalus: Response to shunting and predictors of response: Report of the Guideline Development, Dissemination, and Implementation Subcommittee of the American Academy of Neurology”. In: *Neurology* vol. 85, no. 23 (2015), pp. 2063–2071.
- [51] Hardy, J. A. and Higgins, G. A. “Alzheimer’s disease: the amyloid cascade hypothesis”. In: *Science* vol. 256, no. 5054 (1992), pp. 184–186.
- [52] Hebb, A. O. and Cusimano, M. D. “Idiopathic normal pressure hydrocephalus: a systematic review of diagnosis and outcome”. In: *Neurosurgery* vol. 49, no. 5 (2001), pp. 1166–1186.
- [53] Heston, L. L. et al. “Dementia of the Alzheimer type: clinical genetics, natural history, and associated conditions”. In: *Archives of General Psychiatry* vol. 38, no. 10 (1981), pp. 1085–1090.
- [54] Hiscox, L. V. et al. “Magnetic resonance elastography (MRE) of the human brain: technique, findings and clinical applications”. In: *Physics in Medicine & Biology* vol. 61, no. 24 (2016), R401.
- [55] Holter, K. E. et al. “Interstitial solute transport in 3D reconstructed neuropil occurs by diffusion rather than bulk flow”. In: *Proceedings of the National Academy of Sciences* vol. 114, no. 37 (2017), pp. 9894–9899.
- [56] Holzapfel, G. A., Gasser, T. C., and Stadler, M. “A structural model for the viscoelastic behavior of arterial walls: continuum formulation and finite element analysis”. In: *European Journal of Mechanics-A/Solids* vol. 21, no. 3 (2002), pp. 441–463.

- [57] Holzapfel, G. A. and Gasser, T. C. “A viscoelastic model for fiber-reinforced composites at finite strains: Continuum basis, computational aspects and applications”. In: *Computer methods in applied mechanics and engineering* vol. 190, no. 34 (2001), pp. 4379–4403.
- [58] Holzapfel, G. A. and Ogden, R. W. *Biomechanics of soft tissue in cardiovascular systems*. Vol. 441. Springer, 2014.
- [59] Holzapfel, G. A. and Ogden, R. W. “Constitutive modelling of passive myocardium: a structurally based framework for material characterization”. In: *Philosophical Transactions of the Royal Society A: Mathematical, Physical and Engineering Sciences* vol. 367, no. 1902 (2009), pp. 3445–3475.
- [60] Hong, Q. et al. “Conservative discretizations and parameter-robust preconditioners for Biot and multiple-network flux-based poroelasticity models”. In: *Numerical Linear Algebra with Applications* vol. 26, no. 4 (2019), e2242.
- [61] Iliff, J. J. and Nedergaard, M. “Is there a cerebral lymphatic system?” In: *Stroke* vol. 44, no. 6\_suppl\_1 (2013), S93–S95.
- [62] Iliff, J. J. et al. “A paravascular pathway facilitates CSF flow through the brain parenchyma and the clearance of interstitial solutes, including amyloid  $\beta$ ”. In: *Science translational medicine* vol. 4, no. 147 (2012), 147ra111–147ra111.
- [63] Iliff, J. J. et al. “Cerebral arterial pulsation drives paravascular CSF–interstitial fluid exchange in the murine brain”. In: *Journal of Neuroscience* vol. 33, no. 46 (2013), pp. 18190–18199.
- [64] Jenkinson, M. et al. “Fsl”. In: *Neuroimage* vol. 62, no. 2 (2012), pp. 782–790.
- [65] Jessen, N. A. et al. “The glymphatic system: a beginner’s guide”. In: *Neurochemical research* vol. 40, no. 12 (2015), pp. 2583–2599.
- [66] Jin, B.-J., Smith, A. J., and Verkman, A. S. “Spatial model of convective solute transport in brain extracellular space does not support a “glymphatic” mechanism”. In: *The Journal of general physiology* vol. 148, no. 6 (2016), pp. 489–501.
- [67] Kaster, T., Sack, I., and Samani, A. “Measurement of the hyperelastic properties of ex vivo brain tissue slices”. In: *Journal of biomechanics* vol. 44, no. 6 (2011), pp. 1158–1163.
- [68] Keable, A. et al. “Deposition of amyloid  $\beta$  in the walls of human leptomeningeal arteries in relation to perivascular drainage pathways in cerebral amyloid angiopathy”. In: *Biochimica et Biophysica Acta (BBA)-Molecular Basis of Disease* vol. 1862, no. 5 (2016), pp. 1037–1046.
- [69] Kurtcuoglu, V. et al. “Computational investigation of subject-specific cerebrospinal fluid flow in the third ventricle and aqueduct of Sylvius”. In: *Journal of biomechanics* vol. 40, no. 6 (2007), pp. 1235–1245.

- 
- [70] Lasheras, J. C. “The biomechanics of arterial aneurysms”. In: *Annu. Rev. Fluid Mech.* Vol. 39 (2007), pp. 293–319.
- [71] Lee, J. J. et al. “A mixed finite element method for nearly incompressible multiple-network poroelasticity”. In: *SIAM Journal on Scientific Computing* vol. 41, no. 2 (2019), A722–A747.
- [72] Lehmann, M. et al. “Atrophy patterns in Alzheimer’s disease and semantic dementia: a comparison of FreeSurfer and manual volumetric measurements”. In: *Neuroimage* vol. 49, no. 3 (2010), pp. 2264–2274.
- [73] Leinonen, V. et al. “Cortical brain biopsy in long-term prognostication of 468 patients with possible normal pressure hydrocephalus”. In: *Neurodegenerative Diseases* vol. 10, no. 1-4 (2012), pp. 166–169.
- [74] Lilley, J. *Nuclear physics: principles and applications*. John Wiley & Sons, 2013.
- [75] Little, J. R. and MacCarty, C. S. “Colloid cysts of the third ventricle”. In: *Journal of neurosurgery* vol. 40, no. 2 (1974), pp. 230–235.
- [76] Livingston, G. et al. “Dementia prevention, intervention, and care”. In: *The Lancet* vol. 390, no. 10113 (2017), pp. 2673–2734.
- [77] Logg, A., Mardal, K.-A., and Wells, G. *Automated solution of differential equations by the finite element method: The FEniCS book*. Vol. 84. Springer Science & Business Media, 2012.
- [78] Marieb, E. N. and Hoehn, K. *Human anatomy & physiology*. Pearson Education, 2007.
- [79] McCully, K. S. “Vascular pathology of homocysteinemia: implications for the pathogenesis of arteriosclerosis.” In: *The American journal of pathology* vol. 56, no. 1 (1969), p. 111.
- [80] Mestre, H. et al. “Flow of cerebrospinal fluid is driven by arterial pulsations and is reduced in hypertension”. In: *Nature communications* vol. 9, no. 1 (2018), p. 4878.
- [81] Mihai, L. A. et al. “A family of hyperelastic models for human brain tissue”. In: *Journal of the Mechanics and Physics of Solids* vol. 106 (2017), pp. 60–79.
- [82] Mink, J. W., Blumenschine, R. J., and Adams, D. B. “Ratio of central nervous system to body metabolism in vertebrates: its constancy and functional basis”. In: *American Journal of Physiology-Regulatory, Integrative and Comparative Physiology* vol. 241, no. 3 (1981), R203–R212.
- [83] Moiseyev, G. and Bar-Yoseph, P. Z. “Computational modeling of thrombosis as a tool in the design and optimization of vascular implants”. In: *Journal of biomechanics* vol. 46, no. 2 (2013), pp. 248–252.
- [84] Morin, F. et al. “Biomechanical modeling of brain soft tissues for medical applications”. In: *Biomechanics of Living Organs*. Elsevier, 2017, pp. 127–146.

- [85] Mura, T., Dartigues, J.-F., and Berr, C. “How many dementia cases in France and Europe? Alternative projections and scenarios 2010–2050”. In: *European journal of neurology* vol. 17, no. 2 (2010), pp. 252–259.
- [86] Murphy, M. C., Huston III, J., and Ehman, R. L. “MR elastography of the brain and its application in neurological diseases”. In: *NeuroImage* (2017).
- [87] NGUY, C. et al. “MRI tracer study of the cerebrospinal fluid drainage pathway in normal and hydrocephalic guinea pig brain”. In: *Tokai J Exp Clin Med* vol. 30, no. 1 (2005), pp. 21–29.
- [88] Nilsson, H. and Aalkjær, C. “Vasomotion: mechanisms and physiological importance”. In: *Molecular interventions* vol. 3, no. 2 (2003), p. 79.
- [89] Ogden, R. W. “Large deformation isotropic elasticity—on the correlation of theory and experiment for incompressible rubberlike solids”. In: *Proceedings of the Royal Society of London. A. Mathematical and Physical Sciences* vol. 326, no. 1567 (1972), pp. 565–584.
- [90] Perry, N. S. et al. “Salvia for dementia therapy: review of pharmacological activity and pilot tolerability clinical trial”. In: *Pharmacology biochemistry and behavior* vol. 75, no. 3 (2003), pp. 651–659.
- [91] Project, T. C. *CGAL User and Reference Manual*. 4.14. CGAL Editorial Board, 2019.
- [92] Puso, M. and Weiss, J. “Finite element implementation of anisotropic quasi-linear viscoelasticity using a discrete spectrum approximation”. In: *Journal of biomechanical engineering* vol. 120, no. 1 (1998), pp. 62–70.
- [93] Quarteroni, A. *Modeling the heart and the circulatory system*. Vol. 14. Springer, 2015.
- [94] Quarteroni, A. and Quarteroni, S. *Numerical models for differential problems*. Vol. 2. Springer, 2009.
- [95] Ray, L., Iliff, J. J., and Heys, J. J. “Analysis of convective and diffusive transport in the brain interstitium”. In: *Fluids and Barriers of the CNS* vol. 16, no. 1 (2019), p. 6.
- [96] Relkin, N. et al. “Diagnosing idiopathic normal-pressure hydrocephalus”. In: *Neurosurgery* vol. 57, no. suppl\_3 (2005), S2–4.
- [97] Rennels, M. L. et al. “Evidence for a ‘paravascular’ fluid circulation in the mammalian central nervous system, provided by the rapid distribution of tracer protein throughout the brain from the subarachnoid space”. In: *Brain research* vol. 326, no. 1 (1985), pp. 47–63.
- [98] Rey, J. and Sarntinoranont, M. “Pulsatile flow drivers in brain parenchyma and perivascular spaces: a resistance network model study”. In: *Fluids and Barriers of the CNS* vol. 15, no. 1 (2018), p. 20.
- [99] Robin, C. “Recherches sur quelques particularités de la structure des capillaires de l’encephale”. In: *J. Physiol. Homme. Anim.* Vol. 2 (1859), pp. 537–548.

- 
- [100] Rooij, R. de and Kuhl, E. “Constitutive modeling of brain tissue: current perspectives”. In: *Applied Mechanics Reviews* vol. 68, no. 1 (2016), p. 010801.
- [101] Sack, I. et al. “MR elastography of the human heart: noninvasive assessment of myocardial elasticity changes by shear wave amplitude variations”. In: *Magnetic Resonance in Medicine: An Official Journal of the International Society for Magnetic Resonance in Medicine* vol. 61, no. 3 (2009), pp. 668–677.
- [102] Schley, D. et al. “Mechanisms to explain the reverse perivascular transport of solutes out of the brain”. In: *Journal of theoretical biology* vol. 238, no. 4 (2006), pp. 962–974.
- [103] Schroeder, W., Ng, L., and Cates, J. “The ITK software guide”. In: (2003).
- [104] Shaffer, N., Martin, B., and Loth, F. “Cerebrospinal fluid hydrodynamics in type I Chiari malformation”. In: *Neurological research* vol. 33, no. 3 (2011), pp. 247–260.
- [105] Sharp, M. K., Carare, R. O., and Martin, B. A. “Dispersion in porous media in oscillatory flow between flat plates: applications to intrathecal, periarterial and paraarterial solute transport in the central nervous system”. In: *Fluids and Barriers of the CNS* vol. 16, no. 1 (2019), p. 13.
- [106] Sharp, M. K. et al. “Peristalsis with oscillating flow resistance: a mechanism for periarterial clearance of amyloid beta from the brain”. In: *Annals of biomedical engineering* vol. 44, no. 5 (2016), pp. 1553–1565.
- [107] Silverberg, G. D. et al. “Alzheimer’s disease, normal-pressure hydrocephalus, and senescent changes in CSF circulatory physiology: a hypothesis”. In: *The Lancet Neurology* vol. 2, no. 8 (2003), pp. 506–511.
- [108] Sinkus, R. et al. “High-resolution tensor MR elastography for breast tumour detection”. In: *Physics in Medicine & Biology* vol. 45, no. 6 (2000), p. 1649.
- [109] Sokoloff, L. “Circulation and energy metabolism of the brain”. In: *Basic neurochemistry* vol. 2 (1989), pp. 338–413.
- [110] Spector, R., Snodgrass, S. R., and Johanson, C. E. “A balanced view of the cerebrospinal fluid composition and functions: focus on adult humans”. In: *Experimental neurology* vol. 273 (2015), pp. 57–68.
- [111] Storvestre, G. B. et al. “A preliminary study of cortical morphology in schizophrenia patients with a history of violence.” In: *Psychiatry research. Neuroimaging* vol. 288 (2019), pp. 29–36.
- [112] Storvestre, G. et al. “M88. Regional Cortical Folding and Thickness Differences Between Schizophrenia Patients With and Without a History of Severe Violence”. In: *Schizophrenia bulletin* vol. 43, no. suppl\_1 (2017), S242–S243.

- [113] Støverud, K. H. et al. “Poro-elastic modeling of syringomyelia—a systematic study of the effects of pia mater, central canal, median fissure, white and gray matter on pressure wave propagation and fluid movement within the cervical spinal cord”. In: *Computer methods in biomechanics and biomedical engineering* vol. 19, no. 6 (2016), pp. 686–698.
- [114] Syková, E. and Nicholson, C. “Diffusion in brain extracellular space”. In: *Physiological reviews* vol. 88, no. 4 (2008), pp. 1277–1340.
- [115] Taylor, C. A. and Figueroa, C. “Patient-specific modeling of cardiovascular mechanics”. In: *Annual review of biomedical engineering* vol. 11 (2009), pp. 109–134.
- [116] Taylor, C. A., Hughes, T. J., and Zarins, C. K. “Finite element modeling of blood flow in arteries”. In: *Computer methods in applied mechanics and engineering* vol. 158, no. 1-2 (1998), pp. 155–196.
- [117] Valnes, L. and Schreiner, J. *Surface Volume Meshing Toolkit*. <https://github.com/SVMTK/SVMTK>. 2019.
- [118] Valnes, L. et al. “Assesment of” glymphatic” system using DTI, CSF tracer and finite element computation”. Poster presented at World Congress of Biomechanics, 8-12 July 2018 in Dublin, Ireland.
- [119] Valnes, L. et al. “Assesment of” glymphatic” system using DTI, CSF tracer and finite element computation”. Oral presentation at ECCM-ECFD, 11-15 June 2018 in Glasgow, Scotland.
- [120] Valnes, L. et al. “Inverse modeling of CSF tracer in the human brain using finite element computation”. Oral presentation at Bio-Mechanics workshop on cell membrane dynamics, micro-circulation and plasticity in tissue, 16-17 November 2018 in Oslo, Norway.
- [121] Valnes, L. et al. “Inverse modeling of CSF tracer in the human brain using finite element computation”. Oral presentation at workshop concerning porous media flow, 8 January 2019 in Oslo, Norway.
- [122] Valnes, L. et al. “Porous Media Modelling of Diffusion in Patient Specific Brain Meshes”. Oral presentation at Nordic Seminar on Computational Mechanics, 26-28 October 2016 in Gothenburg, Sweden.
- [123] Vanneste, J. et al. “Shunting normal-pressure hydrocephalus: Do the benefits outweigh the risks?: A multicenter study and literature review”. In: *Neurology* vol. 42, no. 1 (1992), pp. 54–54.
- [124] Vardakis, J. C., Tully, B. J., and Ventikos, Y. “Exploring the efficacy of endoscopic ventriculostomy for hydrocephalus treatment via a multicompartmental poroelastic model of CSF transport: a computational perspective”. In: *PloS one* vol. 8, no. 12 (2013), e84577.
- [125] Vardakis, J. C., Tully, B. J., and Ventikos, Y. “Multicompartmental poroelasticity as a platform for the integrative modeling of water transport in the brain”. In: *Computer models in biomechanics*. Springer, 2013, pp. 305–316.

- 
- [126] Vardakis, J. C. et al. “Fluid–structure interaction for highly complex, statistically defined, biological media: Homogenisation and a 3D multi-compartmental poroelastic model for brain biomechanics”. In: *Journal of Fluids and Structures* (2019).
- [127] Vignon-Clementel, I. E. et al. “Outflow boundary conditions for 3D simulations of non-periodic blood flow and pressure fields in deformable arteries”. In: *Computer methods in biomechanics and biomedical engineering* vol. 13, no. 5 (2010), pp. 625–640.
- [128] Vinje, V. et al. “Respiratory influence on cerebrospinal fluid flow—a computational study based on long-term intracranial pressure measurements”. In: *Scientific reports* vol. 9, no. 1 (2019), p. 9732.
- [129] Virchow, R. “Ueber die Erweiterung kleinerer Gefäße”. In: *Virchows Archiv* vol. 3, no. 3 (1851), pp. 427–462.
- [130] *W. Commons. Main page.* <http://commons.wikimedia.org>. Accessed: 2019-09-30.
- [131] Wang, H. et al. “A modified Holzapfel-Ogden law for a residually stressed finite strain model of the human left ventricle in diastole”. In: *Biomechanics and modeling in mechanobiology* vol. 13, no. 1 (2014), pp. 99–113.
- [132] Wilcock, G., Möbius, H. J., Stöffler, A., et al. “A double-blind, placebo-controlled multicentre study of memantine in mild to moderate vascular dementia (MMM500)”. In: *International clinical psychopharmacology* vol. 17, no. 6 (2002), pp. 297–305.
- [133] Wuerfel, J. et al. “MR-elastography reveals degradation of tissue integrity in multiple sclerosis”. In: *Neuroimage* vol. 49, no. 3 (2010), pp. 2520–2525.
- [134] Wuyts, F. L. et al. “Elastic properties of human aortas in relation to age and atherosclerosis: a structural model”. In: *Physics in Medicine & Biology* vol. 40, no. 10 (1995), p. 1577.
- [135] Xiang, J. et al. “Hemodynamic–morphologic discriminants for intracranial aneurysm rupture”. In: *Stroke* vol. 42, no. 1 (2011), pp. 144–152.
- [136] Zhang, W., Chen, H. Y., and Kassab, G. S. “A rate-insensitive linear viscoelastic model for soft tissues”. In: *Biomaterials* vol. 28, no. 24 (2007), pp. 3579–3586.
- [137] Zhang, W. et al. “Effect of in vitro storage duration on measured mechanical properties of brain tissue”. In: *Scientific reports* vol. 8, no. 1 (2018), p. 1247.
- [138] Zhou, Y. et al. “Mild traumatic brain injury: longitudinal regional brain volume changes”. In: *Radiology* vol. 267, no. 3 (2013), pp. 880–890.



# **Papers & Book Excerpt**



Paper I

# **Brain-wide glymphatic enhancement and clearance in humans assessed with MRI**

**Geir Ringstad, Lars M. Valnes, Anders M. Dale, Are H. Pripp,  
Svein-Are S. Vatnehol, Kyrre E. Emblem, Kent-Andre Mardal,  
Per K. Eide**



# Brain-wide glymphatic enhancement and clearance in humans assessed with MRI

Geir Ringstad,<sup>1,2</sup> Lars M. Valnes,<sup>3</sup> Anders M. Dale,<sup>4,5,6</sup> Are H. Pripp,<sup>7</sup> Svein-Are S. Vatnehol,<sup>8</sup> Kyrre E. Emblem,<sup>9</sup> Kent-Andre Mardal,<sup>3,10</sup> and Per K. Eide<sup>2,11</sup>

<sup>1</sup>Division of Radiology and Nuclear Medicine, Department of Radiology, Oslo University Hospital – Rikshospitalet, Oslo, Norway. <sup>2</sup>Institute of Clinical Medicine, Faculty of Medicine, and <sup>3</sup>Department of Mathematics, University of Oslo, Oslo, Norway. <sup>4</sup>Department of Neurosciences, <sup>5</sup>Department of Radiology, and <sup>6</sup>Multimodal Imaging Laboratory, UCSD, La Jolla, California, USA. <sup>7</sup>Oslo Centre of Biostatistics and Epidemiology, Research Support Services, Oslo University Hospital, Oslo, Norway. <sup>8</sup>The Intervention Centre, Oslo University Hospital – Rikshospitalet, Oslo, Norway. <sup>9</sup>Department of Diagnostic Physics, Oslo University Hospital, Oslo, Norway. <sup>10</sup>Center for Biomedical Computing, Simula Research Laboratory, Lysaker, Norway. <sup>11</sup>Department of Neurosurgery, Oslo University Hospital – Rikshospitalet, Oslo, Norway.

**To what extent does the subarachnoid cerebrospinal fluid (CSF) compartment communicate directly with the extravascular compartment of human brain tissue? Interconnection between the subarachnoid CSF compartment and brain perivascular spaces is reported in some animal studies, but with controversy, and in vivo CSF tracer studies in humans are lacking. In the present work, we examined the distribution of a CSF tracer in the human brain by MRI over a prolonged time span. For this, we included a reference cohort, representing close to healthy individuals, and a cohort of patients with dementia and anticipated compromise of CSF circulation (idiopathic normal pressure hydrocephalus). The MRI contrast agent gadobutrol, which is confined to the extravascular brain compartment by the intact blood-brain barrier, was used as a CSF tracer. Standardized T1-weighted MRI scans were performed before and after intrathecal gadobutrol at defined time points, including at 24 hours, 48 hours, and 4 weeks. All MRI scans were aligned and brain regions were segmented using FreeSurfer, and changes in normalized T1 signals over time were quantified as percentage change from baseline. The study provides in vivo evidence of access to all human brain subregions of a substance administered intrathecally. Clearance of the tracer substance was delayed in the dementia cohort. These observations translate previous findings in animal studies into humans and open new prospects concerning intrathecal treatment regimens, extravascular contrast-enhanced MRI, and assessment of brain clearance function.**

## Introduction

Knowledge about the access of substances administered in the subarachnoid space to human brain as whole could potentially make new treatments of brain disease. The blood-brain barrier (BBB) represents one of the largest obstacles to effective CNS drug delivery (1), and the compartment within blood vessels merely occupies less than 3% of the total brain volume (2). Thus, new therapeutic CNS drugs generally show lower success rates than those for non-CNS indications (3), while intrathecal treatment regimens have emerged with great promise (4, 5).

Previous animal studies have shown communication between the subarachnoid cerebrospinal fluid (CSF) space and perivascular compartments of the brain (6–10) and spinal cord (11). However, literature reporting human in vivo CSF tracer studies is lacking, and observations made in animals have not been translated into humans. Two recent human studies demonstrated brain parenchyma enhancement subsequent to subarachnoid (intrathecal) administration of a MRI contrast agent, but observations were limited to selected ROIs (12, 13). An MRI study of rats failed to demonstrate enhancement in deep brain white matter (14). Moreover, animal studies report diverging findings regarding the sites of perivascular brain influx and efflux and direction of perivascular flow (7, 15, 16). Animal in vivo observations typically cover extremely limited fields of view, as when utilizing 2-photon microscopy (7).

Furthermore, mechanisms behind transport and clearance of substances within the brain interstitial space are controversial. For a long time, size-dependent diffusion was considered to explain

**Conflict of interest:** The authors have declared that no conflict of interest exists.

**Submitted:** April 6, 2018

**Accepted:** May 31, 2018

**Published:** July 12, 2018

**Reference information:**

*JCI Insight.* 2018;3(13):e121537.

<https://doi.org/10.1172/jci.insight.121537>

insight.121537.

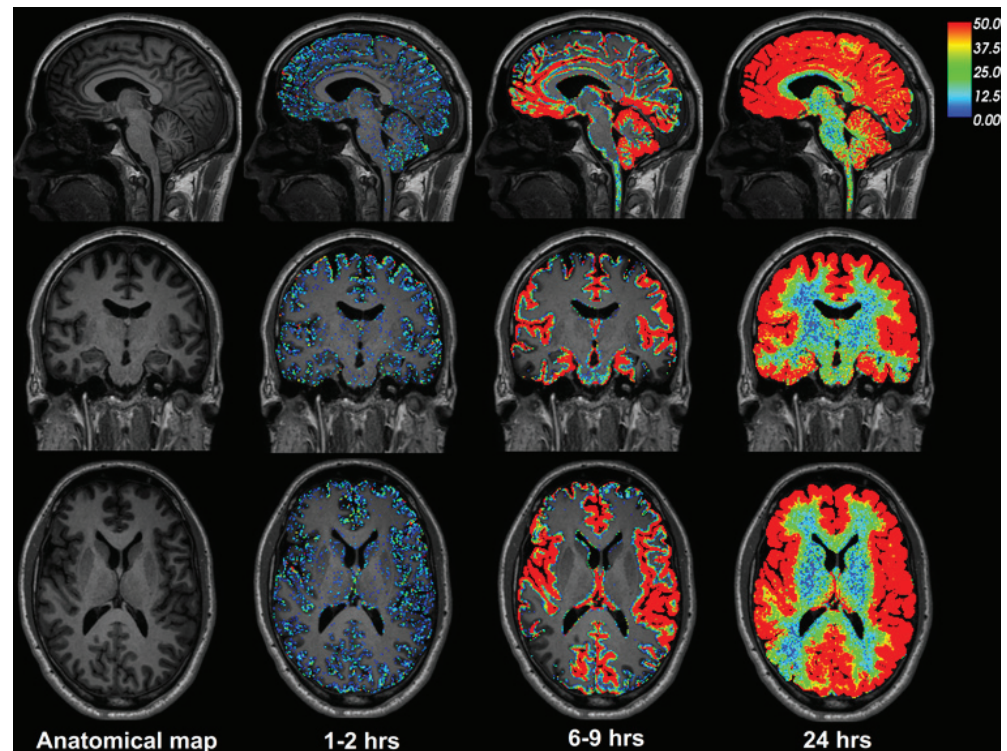


**Figure 1. CSF tracer enrichment over time in one REF subject.** The brain-wide enrichment of CSF tracer over time is shown for one REF individual. The percentage change in signal unit ratio is indicated by the color scale. CSF tracer enrichment occurred in a centripetal pattern at a rate exceeding the expected for pure diffusion, suggesting an important role of bulk flow for transport of substances through the brain. Tracer enrichment occurred primarily, and was most pronounced, in brain regions adjacent to large artery trunks at the surface (6–9 hours), underlining the important role of CSF pulsations for entry of substances into brain tissue perivascular spaces. Note the coronal section (middle row) demonstrating enhancement in the medial temporal lobe adjacent to the circle of Willis and posterior cerebral arteries, in the cingulum adjacent to the location of the anterior cerebral arteries in the anterior interhemispheric fissure, and around the Sylvian fissure, where the middle cerebral artery trunks reside.

interstitial movement of molecules (17). In 2012, a brain-wide pathway for convective transport of waste solutes from the brain was first described and denoted the glymphatic system (7). Net water and solute transport through the extracellular compartment from arterial to venous paravascular spaces was proposed to be dependent on aquaporin-4 (AQP4) water channels and mediated by arterial pulsations (18). Impaired glymphatic function has been suggested to be instrumental in a range of brain diseases; this has been illustrated most in Alzheimer's dementia (7, 19, 20) but has also been shown to be relevant in posttraumatic encephalopathy (21), ageing (22), sleep (23, 24), depression (20), and exercise (25). However, the glymphatic concept has been challenged by several modeling studies that have opposed CSF pulsations as the explanation for net convective interstitial flow (26, 27). Moreover, a later animal study utilized a similar set of experiments as those bringing evidence for a glymphatic system and found, contrary to the previous observations, that interstitial flow could be explained by diffusion alone, independent of AQP4 status (9). Later, several independent groups provided evidence for an important role of AQP4 in glymphatic circulation (28).

To this end, we here show for what we believe to be the first time brain-wide CSF tracer enhancement and clearance in humans. For this, we administered an MRI contrast agent in the subarachnoid CSF compartment, followed by repeated MRI scans at 24 and 48 hours and after 4 weeks. In addition, we found delayed clearance of CSF tracer from the brain in a cohort of patients with dementia and expected CSF circulation failure (idiopathic normal pressure hydrocephalus [iNPH]).

## Results

*Brain-wide distribution of CSF tracer within brain parenchyma in reference subjects.* The study includes 8 reference (REF) individuals who underwent MRI for tentative idiopathic intracranial hypotension due to

**Table 1. Percentage change in signal unit ratio at various time points after i.th. gadobutrol in REF individuals**

| Anatomical region   | Time after i.th. gadobutrol |           |           |           |           |          |          | Significance |
|---|-----------------------------|-----------|-----------|-----------|-----------|----------|----------|--------------|
|   | 1.5–2 hours                 | 2–4 hours | 4–6 hours | 6–9 hours | 24 hours  | 48 hours | 4 weeks  |              |
| [FreeSurfer]  |                             |           |           |           |           |          |          | <0.001       |
| CSF [24]  | 16 ± 20                     | 101 ± 116 | 354 ± 309 | 500 ± 421 | 157 ± 164 | 177      | -8 ± 17  |              |
| Cerebral cortex (gray matter) [1,000–1,035 (left) + 2,000–2,035 (right)]          | -3 ± 7                      | -1 ± 15   | 26 ± 44   | 44 ± 50   | 52 ± 54   | 61       | -6 ± 17  | 0.018        |
| Cerebral white matter [2, 41]   | -3 ± 9                      | -1 ± 18   | 26 ± 40   | 34 ± 46   | 27 ± 33   | 32       | -10 ± 17 | 0.005        |
| Basal ganglia [11, 12, 13, 50, 51, 52]  | -3 ± 8                      | -6 ± 14   | 1 ± 25    | -4 ± 14   | 4 ± 18    | 32       | -8 ± 18  | 0.014        |
| Thalamus [10, 49]   | -2 ± 8                      | -4 ± 15   | 5 ± 26    | 2 ± 18    | 11 ± 21   | 24       | -8 ± 18  | 0.008        |
| Hippocampus, amygdala, accumbens, entorhinal [17, 18, 26, 53, 54, 58, 1006, 2006] | -2 ± 7                      | -1 ± 15   | 28 ± 38   | 43 ± 43   | 42 ± 39   | 40       | -8 ± 17  | 0.004        |
| Cerebellar cortex [8, 47]   | 6 ± 6                       | 12 ± 27   | 45 ± 58   | 67 ± 80   | 53 ± 47   | 90       | -5 ± 18  | 0.003        |
| Cerebellar white matter [7, 46]   | 1 ± 9                       | -3 ± 14   | 3 ± 23    | 2 ± 19    | 15 ± 23   | 33       | -7 ± 18  | 0.009        |

Continuous variables are presented as mean ± SD. Statistical differences were determined by a linear mixed model for repeated measurements.  $n = 8$ . i.th., intrathecal. Numbers given in brackets refer to FreeSurfer predefined numbers for specific brain regions.

CSF leakage (Supplemental Table 1; supplemental material available online with this article; <https://doi.org/10.1172/jci.insight.121537DS1>). CSF leakage was diagnosed in 3 of 8 individuals; no CSF circulation disturbance was identified in the remaining 5 individuals. Even though the REF individuals had some complaints (Supplemental Table 1), we considered this cohort as close to healthy.

Figure 1 illustrates the distribution of CSF tracer in the brain parenchyma of one REF individual (see Supplemental Video 1). The tracer distributed centripetally from cortex to deeper brain regions. Supplemental Figure 1 shows the change in the T1 signal within the CSF space and brain parenchyma following intrathecal gadobutrol. Table 1 presents the percentage change in normalized T1 signal from before CSF tracer administration, including percentage change for cerebral cortex (gray matter), cerebral white matter, basal ganglia, thalamus, limbic structures (hippocampus, amygdala, nucleus accumbens, and entorhinal cortex), cerebellar cortex, and cerebellar white matter. The MRI signal increase was significant at all main locations (Table 1). Figure 2 shows the CSF contrast enrichment after 6–9 hours in coronal MRI sections of 8 REF individuals. As illustrated, the CSF tracer enrichment occurred in a centripetal pattern and primarily in brain regions adjacent to large artery trunks at the surface, i.e., the anterior, middle, and posterior cerebral arteries.

Figure 3 shows the percentage change in normalized T1 signal over time for selected brain subregions, including cerebral cortex (Figure 3A), cerebral white matter (Figure 3B), cerebellar cortex (Figure 3C), cerebellar white matter (Figure 3D), limbic structures (Figure 3E), basal ganglia (Figure 3F), corpus callosum (Figure 3G), and hippocampus (Figure 3H).

The REF individuals showed CSF tracer enrichment in close to all the brain regions studied, as further detailed in Supplemental Table 2.

*Brain-wide distribution of CSF tracer in individuals with iNPH dementia.* The study also includes 9 individuals with a subtype of dementia, denoted as iNPH (Supplemental Table 1). The iNPH patients were older than the REF subjects and presented with other symptoms (Supplemental Table 1). Figure 4 illustrates the color-coded enrichment of CSF tracer in brain parenchyma over time for one iNPH patient (see Supplemental Video 2). Enrichment in the periventricular white matter is a feature typical of iNPH, due to ventricular tracer reflux and transependymal migration, as previously reported (13). Figure 5 shows the CSF contrast enrichment after 6–9 hours in coronal MRI sections of 8 iNPH individuals. As for REF subjects, the CSF tracer enrichment occurred in a centripetal pattern and primarily in brain regions adjacent to large artery trunks at the surface. Table 2 presents the percentage of change in CSF tracer enrichment over time for selected brain regions of the iNPH subjects, including cerebral cortex (gray matter), cerebral white matter, basal ganglia, thalamus, and limbic structures as well as the cerebellar gray and white matter. CSF tracer enrichment was found in all these regions, and all subregions were defined in FreeSurfer (Supplemental Table 3).

*Clearance of CSF tracer in REF subjects and iNPH patients.* Our findings point to some important differences between REF subjects and individuals with iNPH dementia.

As illustrated in Figure 6, as compared with REF subjects, the CSF tracer enrichment in iNPH patients

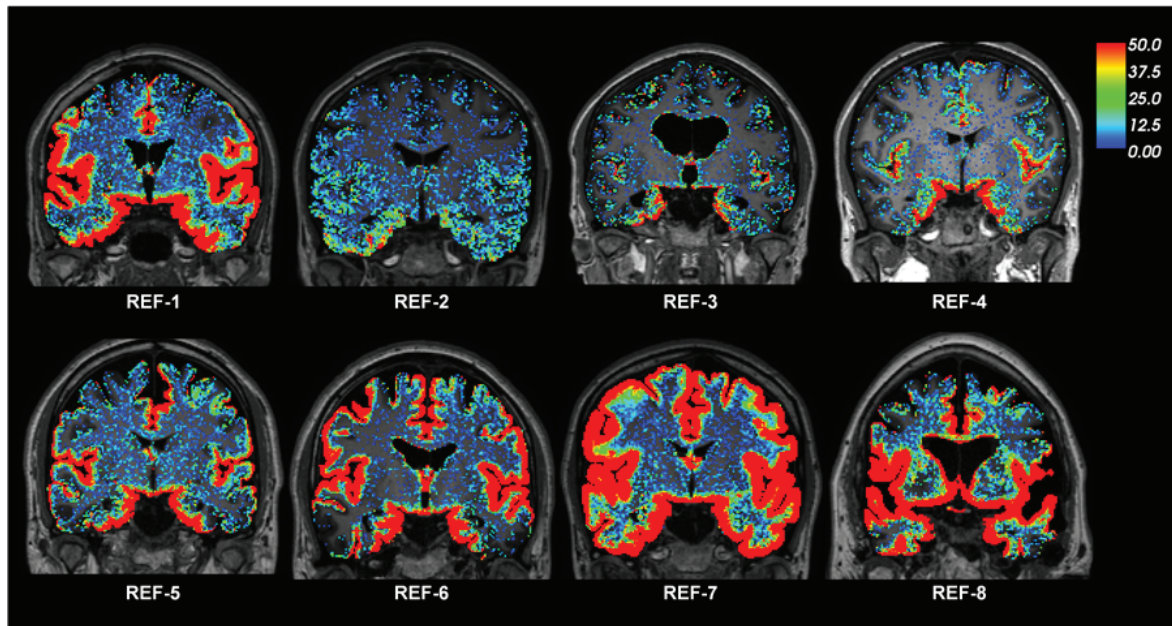


**Figure 2. CSF tracer enrichment in REF subjects shows a centripetal pattern.** The enrichment of CSF tracer after 6–9 hours is shown for 8 REF individuals. The percentage change in signal unit ratio is indicated by the color scale. The coronal sections illustrate that CSF tracer enrichment occurred in a centripetal pattern and primarily in brain regions adjacent to large artery trunks at the surface, i.e., the anterior, middle, and posterior cerebral arteries.

at 24 hours was significantly higher in cerebral white matter (Figure 6C), basal ganglia (Figure 6D), corpus callosum (Figure 6F), limbic system (Figure 6G), and hippocampus (Figure 6H), indicative of reduced tracer clearance. Supplemental Table 4 shows differences in percentages of change over time of normalized T1 signal for a wide range of brain regions.

*CSF tracer enrichment after 4 weeks.* We also compared the normalized T1 signal before and 4 weeks after intrathecal CSF tracer to look for signs of CSF tracer retention after 4 weeks. This was not found in any brain region examined for either REF or iNPH (Supplemental Table 5).

In a wide range of brain regions, the normalized T1 signal was consistently lower in iNPH individuals than in REF individuals before intrathecal gadobutrol and reached statistical significance for some of the regions (Supplemental Table 5). A lower T1 signal may be interpreted as indicative of higher brain parenchymal water content.

*Correlation between CSF tracer enrichment and brain volume.* The Pearson correlation coefficients between percentage change in signal unit ratios and tissue volume for white matter, gray matter, and CSF of lateral ventricles for REF and iNPH subjects are presented in Table 3. The correlation coefficients differ between REF and iNPH cohorts. In iNPH subjects, the volume of gray matter correlated negatively with CSF tracer enhancement in gray and white matter, i.e., with increasing volume the CSF tracer enhancement was lower.

## Discussion

*Brain-wide enhancement of CSF tracer in human brain.* In this human CSF tracer study, repeated MR imaging provides *in vivo* evidence of a route for macromolecules administered in CSF from the subarachnoid compartment to the entire brain. Any substance with features similar to the studied tracer, gadobutrol, should therefore be expected to access all brain regions when administered intrathecally. We have previously demonstrated that an equally small amount of MRI contrast agent injected intrathecally at the lumbar level typically reaches the intracranial subarachnoid compartment in approximately 20 minutes, where it primarily distributes along large artery trunks at the brain surface (13). These observations were reproduced in the present work. Moreover, we reproduced the finding of primary tracer entry into the brain in tissue adjacent to major artery trunks, indicating an important role of CSF pulsations for macromolecular transport within brain tissue. Here, we have extended our assessment to cover all brain subregions, demonstrating tracer enhancement in locations even several centimeters deep to the brain surface and tracer bulk flow through the cerebral mantle. The CSF tracer enhancement within the brain occurred in a centripetal pattern, with some regional differences, and peak

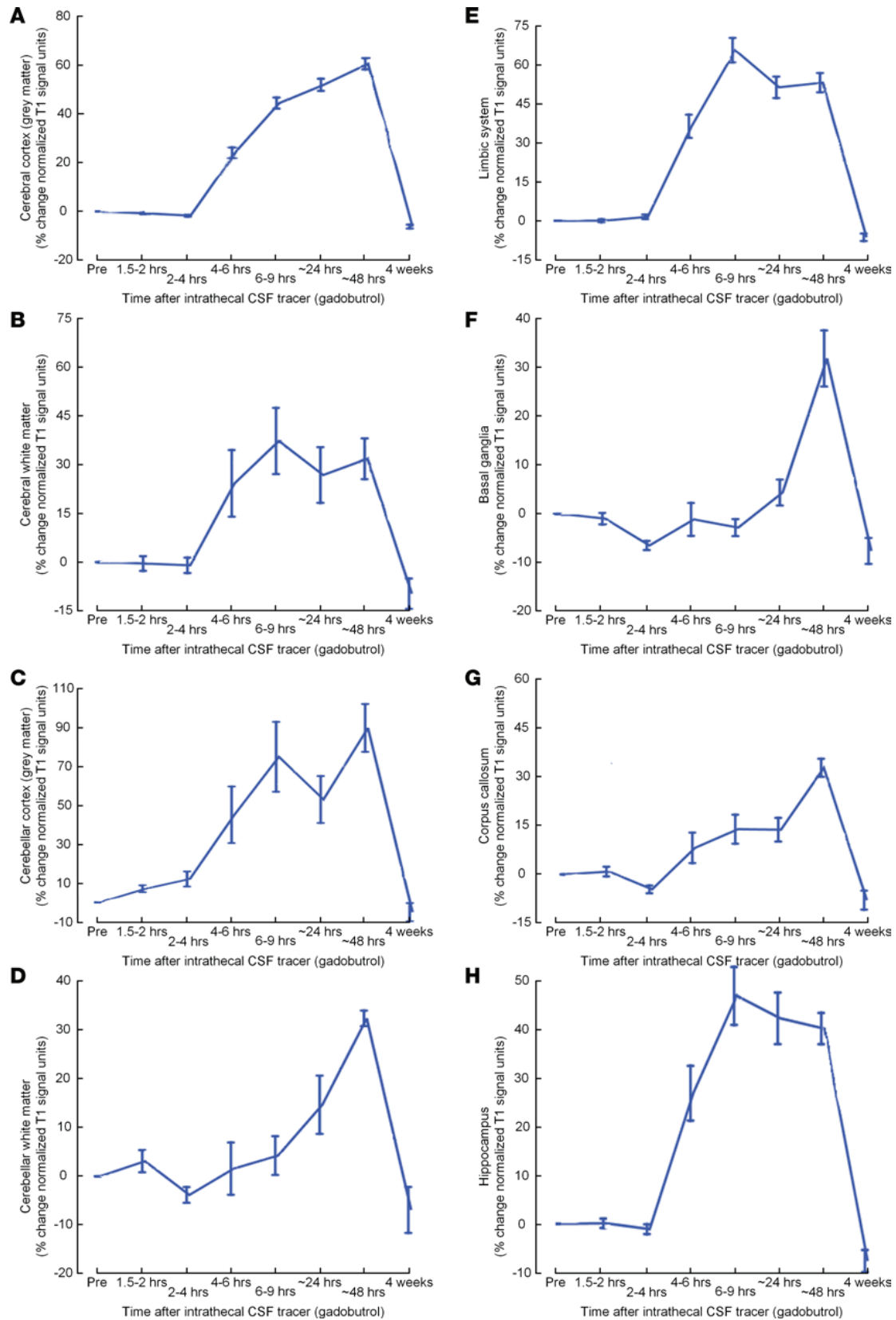


**Figure 3. CSF tracer enrichment in some brain regions of the REF cohort.** Trend plots of percentage change in signal unit ratio are presented for main regions within the supratentorial and infratentorial compartments, including (A) cerebral cortex (gray matter), (B) cerebral white matter, (C) cerebellar cortex, (D) cerebellar white matter, (E) limbic system, (F) basal ganglia, (G) corpus callosum, and (H) hippocampus. Trend plots are presented with mean  $\pm$  standard error (SE).  $n = 8$ .

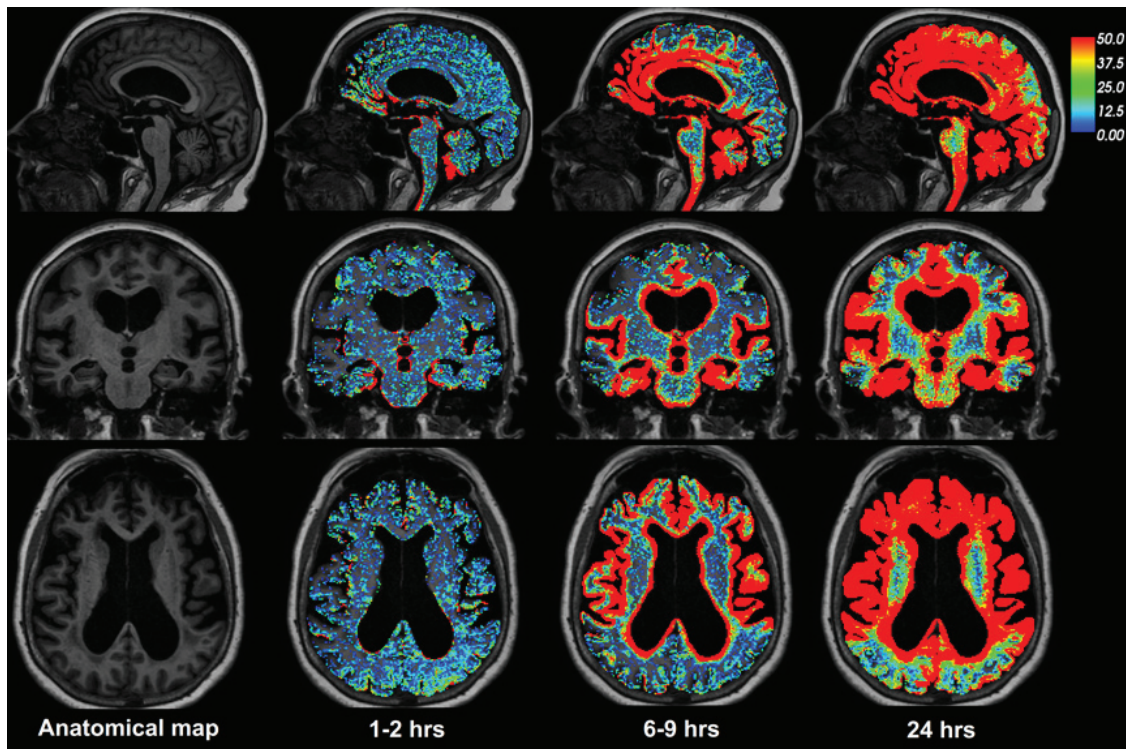


**Figure 4. CSF tracer enrichment over time in one iNPH subject.** The brain-wide enrichment of CSF tracer over time is shown in one iNPH individual. The percentage change in signal unit ratio is indicated by the color scale. The centripetal pattern of enrichment is comparable with that in REF individuals. In iNPH, there is also enrichment of periventricular white matter due to ventricular reflux of CSF tracer substance (ventricular CSF space is subtracted). While clearance of tracer was delayed in iNPH, enrichment occurred with at least the same rate as in REF. This may be attributed to enlarged perivascular spaces in iNPH, where neurodegeneration and vascular disease typically are important associated features. Regions with the initial, and most, tracer enrichment are nearby the course of large artery trunks at the brain surface (as further outlined in the legend to Figure 1), indicating the important role of CSF pulsations for brain tracer enrichment. These regions (entorhinal, hippocampus, insula, cingulum, etc.) also correspond to areas that traditionally are included in the limbic system (“limbic enhancement”) and also are areas typically susceptible to consecutive tau propagation in Alzheimer’s disease. This should be noted, as reduced clearance of CSF tracer through the glymphatic system has been proposed as instrumental in the pathogenesis of neurodegenerative disease.

enhancement typically occurred at 24 hours after tracer injection. Thereafter, the level of tracer in parenchyma declined, and tracer had been cleared from the brain after 4 weeks.

*Mechanisms behind brain cortex tracer enrichment.* The hydrodynamic diameter of gadobutrol has, to our knowledge, not been estimated previously. However, prediction of hydraulic diameter based on molecular weight (MW) is feasible (29). With a MW of 3,000 Da, dextran 3 is comparable to the highly hydrophilic molecule gadobutrol with respect to MW (MW = 604 Da), and the hydrodynamic diameter of dextran 3 has been experimentally calculated as 26 Å or 2.6 nm (30). Hydraulic diameter of gadobutrol is therefore not expected to exceed this, and further distribution within the brain cortex interstitial compartment should accordingly be expected to be predominantly driven by diffusive flux (1). Average in vivo width of extracellular space has been reported to be between 38 and 64 nm (31). In ref. 17, the timescale of the relative diffusive tracer distribution ( $C$ ) is estimated as follows:  $C = \operatorname{erfc}(x/(2 \times \sqrt{D \times t}))$ . Using this formula, assuming a diffusivity of  $D = 12 \times 10^{-7} \text{ cm}^2/\text{s}$ , with  $x$  and  $t$  corresponding to the length in cm and time in seconds, respectively, a 50% saturation of the extracellular space can be estimated to occur at around 55 hours. The assumptions underlying this formula are, however, that the length scale is such that the cortex can be considered flat and the tracer distribution uniform. These assumptions are not valid in our case, but it seems unlikely that diffusion alone explains the brain-wide distribution. Further, loss of the molecule across the BBB, uptake into cells, or binding to receptors all may modify diffusion (17).

It has been proposed that the perivascular compartment of human cortex is merely a potential space for movement of solutes (32–36), a view that recently was maintained based on observations made in fixed tissue specimens (37). In contrast, others have reported that the intrinsic hydraulic permeability of the human perivascular space is far greater than the width of the cortical extracellular space (1). The width of the perivascular space is suggested to be at least 2 orders of magnitude greater than neocortical extracellular

**Table 2. Percentage change in signal unit ratio at various time points after i.th. gadobutrol in iNPH individuals**

| Anatomical region   | Time after i.th. gadobutrol |           |           |           |           |           |         | Significance |
|---|-----------------------------|-----------|-----------|-----------|-----------|-----------|---------|--------------|
|   | 1.5–2 hours                 | 2–4 hours | 4–6 hours | 6–9 hours | 24 hours  | 48 hours  | 4 weeks |              |
| [FreeSurfer]  |                             |           |           |           |           |           |         |              |
| CSF [24]  | 23 ± 29                     | 94 ± 80   | 448 ± 346 | 755 ± 323 | 719 ± 363 | 256 ± 304 | 2 ± 16  | <0.001       |
| Cerebral cortex (gray matter) [1,000–1,035 (left) + 2,000–2,035 (right)]            | 4 ± 20                      | 3 ± 14    | 23 ± 25   | 37 ± 30   | 91 ± 46   | 66 ± 57   | 5 ± 17  | <0.001       |
| Cerebral white matter [2, 41]   | 3 ± 20                      | 3 ± 16    | 41 ± 39   | 53 ± 43   | 66 ± 38   | 34 ± 39   | 2 ± 16  | <0.001       |
| Basal ganglia [11, 12, 13, 50, 51, 52]  | 4 ± 21                      | 0 ± 15    | 4 ± 20    | 5 ± 27    | 27 ± 25   | 22 ± 25   | 2 ± 17  | <0.001       |
| Thalamus [10, 49]   | 5 ± 21                      | 2 ± 16    | 10 ± 22   | 10 ± 17   | 33 ± 27   | 20 ± 24   | 3 ± 17  | <0.001       |
| Hippocampus, amygdala, accumbens, entorhinal [17, 18, 26, 53, 54, 58, 1,006, 2,006] | 5 ± 22                      | 6 ± 16    | 42 ± 35   | 62 ± 46   | 92 ± 43   | 49 ± 53   | 4 ± 17  | <0.001       |
| Cerebellar cortex [8, 47]   | 7 ± 18                      | 9 ± 16    | 30 ± 28   | 53 ± 35   | 96 ± 38   | 52 ± 43   | 9 ± 16  | <0.001       |
| Cerebellar white matter [7, 46]   | 4 ± 19                      | 1 ± 15    | 6 ± 18    | 4 ± 16    | 27 ± 24   | 19 ± 17   | 4 ± 16  | <0.001       |

Continuous variables given as mean ± SD. Statistical differences determined by a linear mixed model for repeated measurements.  $n = 9$ . i.th., intrathecal. Numbers given in brackets refer to FreeSurfer predefined numbers for specific brain regions.

space width, and intrinsic hydraulic permeability of the perivascular space is suggested to be at least 10,000-fold higher than the extracellular space of the neuropil. It is therefore reasonable to assume that the cortical tracer enhancement in our human cohorts derives from the same mechanism as that reported in animal studies, where perivascular CSF tracer distribution in animal cortex is consistently demonstrated (6–8). Human cortical enhancement was, however, a much more durable process (days) than that of animals (hours) (14). The role of vascular pulsations being mediated to CSF for enrichment of perivascular spaces is underlined by the rich and early enhancement in parenchyma adjacent to large arterial vessels at the brain surface (Figures 1, 2, 4, and 5). Here, diffusion likely adds to advective pulsatile to-and-fro flow, i.e., dispersion (38). Dispersion by itself does not require net, convective flow. Based on animal studies (6, 7, 39), we expected further transport of tracer into the interstitial space to occur at the neurovascular interface through astrocytic inter-endfeet gaps, which allow for passage of solutes of up to 20-nm hydraulic diameter (38).

*Tracer enrichment in deep brain structures.* CSF tracer also propagated in brain tissue deeper than what can be attributed to perivascular spaces connected to the brain surface only. The present in vivo observations of contrast enhancement in deep white matter extends evidence from a similarly designed MRI study of rats, where lack of enhancement in deep portions of the brain white matter was attributed to concentrations of contrast agent probably being too small to be detected. (14). Image resolution of the MRI scan was 1 mm, while the sizes of paravascular and interstitial spaces are in the order of  $\mu\text{m}$ . A detailed assessment of molecular motion at a microscopic level was therefore beyond reach in this study.

Previous animal studies have indicated that axon tracts, in addition to perivascular spaces, can also act as preferential, low-resistance pathways for solutes through the brain (40). White matter has been identified as a major site for convective flow under normal conditions (41). In a recent study, interconnections between perivascular compartments of arterioles and veins, allowing small and large molecules to bypass the interstitial space, were demonstrated (42). Diffusion alone has also been proven inefficient at distances larger than a few millimeters, as in the human brain (43). Furthermore, tracers of different MW are cleared at similar speeds in the brain, which is not consistent with diffusion, but rather convective flow (44). Our study observations, with enrichment of CSF tracer over a range of several centimeters within 24 hours, may suggest that convective forces and bulk flow in general are more important for brain-wide tracer distribution than diffusion alone. Bulk flow has previously proven difficult to quantify (17) but is considered most likely to be restricted to the perivascular spaces (40). One study estimated the velocity of white matter bulk flow toward the ventricles as 10.5  $\mu\text{m}/\text{min}$  (approximately 15 mm per day) (41). In our REF subjects, enhancement in regions several cm deep to the brain surface was found at 24 hours (Figures 1–3; Table 1; and Supplemental Table 2), which by far exceeds previous estimates for bulk flow. Parenchymal migration of a substance over a distance much farther than previously shown in both animals and humans also has important implications for the potential of neurotransmitters at a synapse to reach receptors outside the immediate postsynaptic site. Such extrasynaptic volume transmission has not been explicitly identified before and has therefore remained an elusive concept with respect to intercellular communication in the CNS (17).

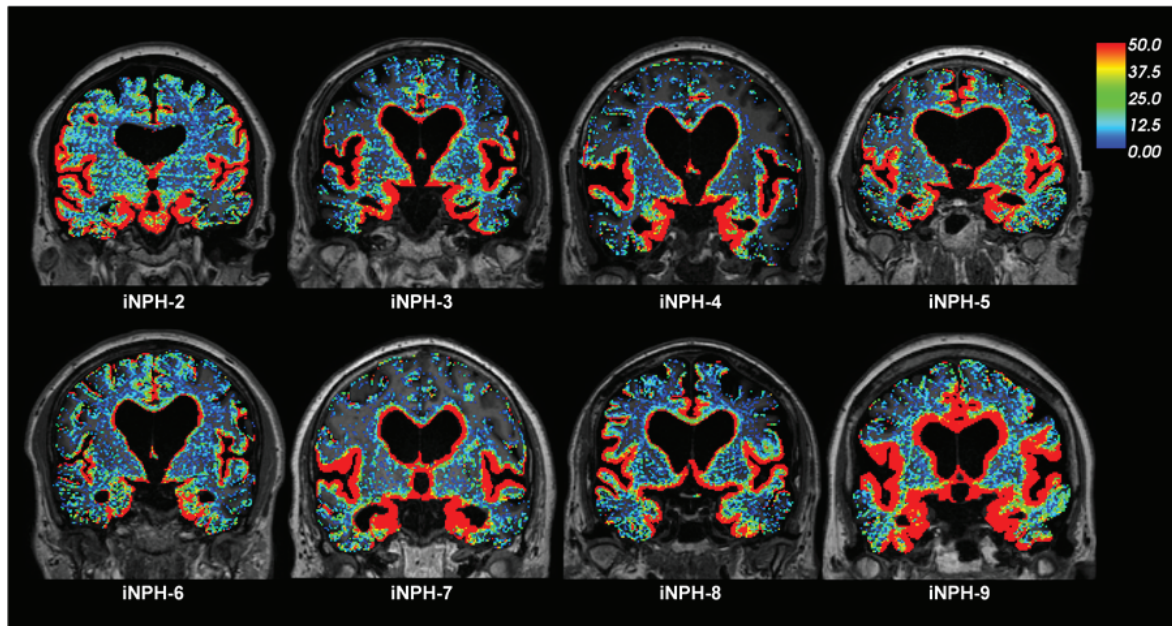


**Figure 5. CSF tracer enrichment in INPH subjects shows a centripetal pattern.** The enrichment of CSF tracer after 6–9 hours is shown for 8 INPH individuals (MRI after 6–9 hours was lacking in one INPH individual). The percentage change in signal unit ratio is indicated by the color scale. The coronal sections illustrate that CSF tracer enrichment occurred in a centripetal pattern and primarily in brain regions adjacent to large artery trunks at the surface, i.e., the anterior, middle, and posterior cerebral arteries. Periventricular tracer enhancement due to reflux of tracer into the ventricular system is a typical feature of INPH (13).

*Effect of sleep.* One mechanism behind the observed high bulk flow rate could be the effect of sleep. Natural sleep in animal studies has been shown to associate with increased size of the interstitial space, facilitating increased convective exchange of CSF with interstitial fluid and clearance of macromolecules (23). While we notice that the observed tracer enhancement in brain generally peaked after the first night (at 24 hours), which is remarkable, we do not have a sufficient number of MRIs in the time interval from 6–9 hours to 48 hours to conclude the exact time point of when peak enhancement truly occurred. It should also be noted that tracer enrichment of cortex and white matter was in progress before onset of sleep (Figures 1–3; Table 1; and Supplemental Table 2). Peak enhancement occurring at 24 hours differs significantly from that found in studies of rats, which typically was at 1–3 hours (14, 45).

*Tracer clearance routes from CSF and brain parenchyma.* The centripetal pattern of brain enhancement seems to contradict studies in which intraparenchymal tracers have been injected and described as leaving the brain centrifugally along the walls of arteries (15, 46). The findings made in these previous tracer studies have led to the hypothesis that pathological aggregates of amyloid- $\beta$  in walls of cortical arteries are indicative of AD pathogenesis. Widespread penetration of substances from CSF into brain parenchyma along perivascular spaces of arteries is, however, well supported by animal studies with a similar experimental setup to ours (1, 47–49). While our present study demonstrated declining levels of the tracer molecule after 24 hours, and no remains at 4 weeks, the routes for tracer clearance are still elusive. Uptake into arachnoid villi, as proposed more than one hundred years ago, seems to be of minor importance in humans, as reviewed by Brinker et al. (50) and as indicated in our recent study (13). In 2015, lymphatic vessels draining from CSF to neck lymph nodes were for the first time detected in walls of dural venous sinuses (51, 52). The full significance of these lymphatic drainage pathways has yet to be shown, but we have found that neck lymph node and brain tracer enhancement coincided in time, indicating this drainage is from the brain rather than directly from CSF (53). Should lymphatic drainage be directly from CSF, as suggested in a recent animal study (54), this would then occur much slower in humans than reported in animals. Our present findings of peak tracer enhancement in CSF at 6–9 hours, followed by a decline before peak enhancement in brain occurs (24 hours; Figure 3 and Figure 6), contradicts that the levels of tracer in CSF and parenchyma are merely balanced by diffusion between these compartments. Because CSF tracer clearance along veins is suggested in several studies (6–8, 39), we found it reasonable to hypothesize that perivenous compartments and lymphatic vessels are interconnected.

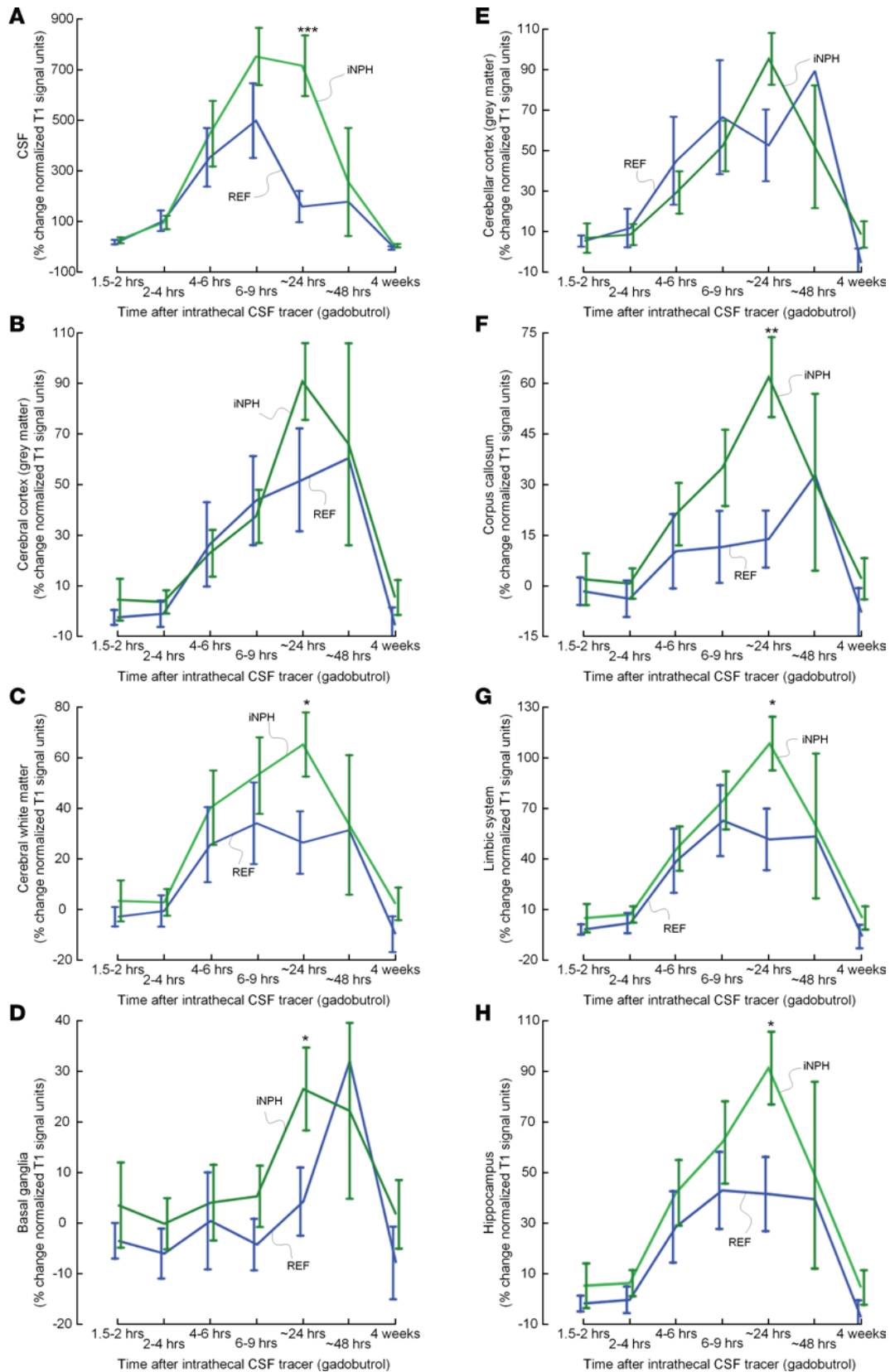


**Figure 6. Comparison of CSF tracer enrichment between REF and iNPH subjects within selected brain regions.** Trend plots of percentage change in signal unit ratio are presented for different regions within the supratentorial and infratentorial compartments, including (A) CSF, (B) cerebral cortex (grey matter), (C) cerebral white matter, (D) basal ganglia, (E) cerebellar cortex, (F) corpus callosum, (G) limbic system, and (H) hippocampus. Significant differences between REF (blue line) and iNPH (green line) groups were determined by linear mixed models for repeated measurements. \* $P < 0.05$ , \*\* $P < 0.01$ , \*\*\* $P < 0.001$ . Trend plots are presented with mean  $\pm$  standard error (SE).  $n = 8$ , REF;  $n = 9$ , iNPH.

**Table 3. Correlation between CSF tracer enrichment at 24 hours and volume of the specific brain region**

|   | CSF contrast enhancement in gray matter (%) | CSF contrast enhancement in white matter (%) | CSF contrast enhancement in lateral ventricles (%) |
|---|---|--|--|
| REF patients                                    |   |  |  |
| Volume of gray matter (mm <sup>3</sup> )        | R = 0.11 (NS)                               | R = 0.08 (NS)                                | R = -0.60 (NS)                                     |
| Volume of white matter (mm <sup>3</sup> )       | R = 0.21 (NS)                               | R = 0.25 (NS)                                | R = -0.31 (NS)                                     |
| Volume of lateral ventricles (mm <sup>3</sup> ) | R = -0.037 (NS)                             | R = -0.36 (NS)                               | R = 0.92 (P = 0.003)                               |
| iNPH patients                                   |   |  |  |
| Volume of gray matter (mm <sup>3</sup> )        | R = -0.78 (P = 0.012)                       | R = -0.81 (P = 0.008)                        | R = -0.13 (NS)                                     |
| Volume of white matter (mm <sup>3</sup> )       | R = -0.33 (NS)                              | R = -0.46 (NS)                               | R = -0.33 (NS)                                     |
| Volume of lateral ventricles (mm <sup>3</sup> ) | R = -0.37 (NS)                              | R = -0.21 (NS)                               | R = 0.41 (NS)                                      |

Pearson correlation coefficients, with significance level. Gray matter corresponds to FreeSurfer regions 1,000–2,999, white matter regions correspond to FreeSurfer regions 3,000–5,002, and lateral ventricles correspond to FreeSurfer regions 4 and 43. The CSF contrast enrichment refers to percentage change in signal unit ratios after 24 hours as compared with baseline.

*Therapeutic and diagnostic implications of brain-wide tracer enhancement.* The potential for administering drugs via the intrathecal route has been considered to be limited by some (55). Compared with the intravenous route, intrathecal delivery of drugs in treatment of neurological disease is still rare, and few drugs have been approved for this use. Because many neurological conditions primarily are diseases of the interstitial space, and do not cause breakdown of the BBB, brain-wide access to the extravascular CNS compartment via intrathecal delivery may show to have many benefits. An already established treatment regime is that of intrathecal monoclonal antibodies against multiple sclerosis (56). Other medications approved by the US Food and Drug Administration for intrathecal use include morphine, ziconotide, and baclofen (57). Studies of intrathecal treatment for infantile-onset spinal muscular atrophy are emerging with promising results (4), and intrathecal delivery of recombinant enzyme to patients with mucopolysaccharidosis type II (Hunter syndrome) has been proposed (47).

Knowledge of what extent an intrathecal substance with certain size and properties can distribute throughout the entire human brain may help pave the way for new treatment options. It is likely that monoclonal antibodies and viral vectors for gene therapy could provide new prospects for treatment of neurodegenerative disorders, such as Alzheimer's and Parkinson's disease (1, 58). Furthermore, neoplastic and inflammatory processes that primarily occur in the extravascular compartment could more readily be targeted for diagnostic purposes. For the latter, contrast-enhanced imaging of the extravascular space may increase sensitivity for detection of extravascular inflammatory (59) and neoplastic diseases (60), which probably are most likely missed with conventional MRI techniques. With contrast-enhanced imaging, disease-targeting substances may be conjugated with contrast agents to mark disease and monitor treatment.

There are to date no gadolinium-based MRI contrast agents approved for intrathecal use. In the present study, gadobutrol was used after special permission granted from the National Medicine Agency of Norway. Gadolinium accumulation in the brain after multiple intravenous administrations has been a major concern since it was first reported in 2014 (61). However, there have been no reports demonstrating brain toxicity (62); the US Food and Drug Administration and American College of Radiology have declared that there is no evidence to date that gadolinium accumulation in the brain is harmful and that there is no need to restrict its intravenous usage. In the present study, where intrathecal administration of an MRI contrast agent was utilized, no serious adverse events were noted among our study subjects, and at the 4-week MRI follow-up, no evidence of remaining gadobutrol within brain parenchyma or CSF was found (Supplemental Table 5). Interestingly, gadolinium deposits in brain tissue have recently been attributed to leakage from blood into CSF through the choroid plexus and entrance into the brain from the surface along perivascular spaces (62). In rats, gadolinium concentration has been shown to be higher in CSF than blood 4.5 hours after intravenous distribution and highest in brain after 24 hours (63). In principle, an intravenous dose could therefore potentially expose the brain perivascular compartment to a larger amount of contrast agent than a very small intrathecal dose, as used in this study. Macrocyclic contrast agents (including gadobutrol) are now generally preferred above linear agents, which are chemically less stable compounds and more susceptible to release into tissue (64, 65).

*Reduced clearance of CSF tracer in iNPH.* The other main finding of this study is the demonstration of reduced clearance of gadobutrol used as CSF tracer in a cohort of patients with dementia. Clearance of MRI contrast agents, such as gadobutrol, has previously been proposed to potentially resemble clearance of brain macromolecules with similar properties (14), including amyloid- $\beta$  (7) and tau (21, 66). These proteins are found pathologically accumulated as insoluble amyloid- $\beta$  and as component of neurofibrillary tangles, respectively, in brains of patients with Alzheimer's disease (67). There is large overlap of typical findings in brain specimens of patients with Alzheimer's disease and iNPH (68). We have recently demonstrated volume loss and reduced tracer clearance in a iNPH dementia cohort at the entorhinal area (69), where the first signs of neurodegeneration appear in Alzheimer's disease (70). The apparent important role of artery pulsations in parenchymal tracer propagation compares well with findings of vascular comorbidity (71) and reduced subarachnoid space propagation of CSF tracer in iNPH (13). Furthermore, brain subregions being closest to large artery trunks at the brain surface are regions traditionally considered as part of the limbic system (entorhinal cortex, hypothalamus, insula, amygdala, cingulum, etc.), representing the phylogenetically oldest part of the cerebral cortex (allocortex). On the MRIs, these regions enhanced earlier and enhancement was richer compared with other brain regions (Figures 1, 2, 4 and 5; Table 2; Supplemental Table 3). We find it compelling how this pattern of time-progressive "limbic enhancement" resembles the pattern of neurofibrillary tangle advancement in evolving Alzheimer's disease (72), which to date is incompletely understood. A contributing cause to disease evolution might therefore be that brain regions being most dependent on CSF pulsations for clearance of brain macromolecules are also the ones most susceptible to disease when pulsations are restricted or when paravascular pathways are blocked by any cause. To what extent restricted CSF pulsations and restricted paravascular flow may be instrumental in the pathogenesis behind Alzheimer's disease, iNPH, and other brain proteinopathies should be subject to future studies.

In the present study, the 24-hour time point showed the best discrimination between patients and REF individuals. Assessment of cerebral clearance with MRI by absolute quantities is, however, not possible at this level, as normalized T1 signal cannot be assumed to be strictly proportional with amount of contrast agent in each image voxel. Another important limitation of our comparison of iNPH patients with REF individuals is their different ages, and paravascular clearance has been shown to be impaired with ageing (22). Nevertheless, CSF flow patterns in iNPH patients also differ clearly from those of REF individuals by means of an early and persisting ventricular regurgitation of tracer, as well as by enhancement of periventricular tissue across the ependymal ventricular lining, which was particularly prominent on late scans (Figures 1, 2, 4 and 5). Net tracer flux into brain ventricles may be hypothesized to express a salvage route for CSF flow along the pathway of least resistance and subsequently lead to compromised brain paravascular flow. AQP4 density and its anchoring protein dystrophin 71 have been found to be reduced at astrocytic end feet in iNPH (73). AQP4 loss may cause swelling of end feet and thereby may reduce the distance of inter end feet gaps (74), which may in its turn deteriorate permeability for solutes. The 1-mm image resolution of our MRI exams prevents this direct observation and therefore remains speculative. Furthermore, we note that parenchymal enhancement in iNPH patients was comparable with that of REF individuals (Figure 6) and, in some regions, was more pronounced (Figure 6 and Supplemental Table 4). Increased width of perivascular spaces has been shown to be associated with increasing age (75) and may thus be a determining factor for parenchymal tracer enrichment more than clearance, which has rather been proposed to be dependent on convective forces and AQP4 status in the glymphatic system (7). Our finding is also analogous to those of an MRI study of rats with diabetes mellitus type 2, where perivascular tracer influx was comparable to that in nondiabetes mellitus rats (45). Based on previous data (14), it was suggested that diabetes mellitus type 2 rats have enlarged perivascular spaces owing to increased risk of small vessel disease. This enlargement may therefore reduce resistance to perivascular tracer influx (76).

Moreover, we also found that the correlation between percentage change in tracer enrichment after 24 hours and volume of brain region (gray and white matter and CSF; Table 3) was different between REF and iNPH individuals. For gray matter of iNPH patients, there were negative correlations between CSF tracer enrichment within the respective region and volume of the specific region, i.e., increased volume of gray matter was associated with lower CSF contrast enrichment. Reduced brain tissue volume in iNPH patients may therefore also have contributed to the observed stronger tracer enrichment in this group at 24 hours. In future studies, CSF tracer clearance assessment with MRI may preferably be compared in patients with minimal cognitive impairment and age-matched healthy controls. This would further reveal the full potential of MRI-based assessment of brain metabolic function to detect neurodegenerative disease in the presymptomatic phase.

*Conclusions.* In this study, we have used repeated MRI to demonstrate human brain-wide enrichment of a CSF tracer administered intrathecally. Our observations in human brain add to previous evidence from animal studies, with important distinctions. In humans, CSF tracer distributed centripetally from the surface toward structures in the deep parts of the brain, but over a much longer time course than that reported in animals. Vascular pulsations mediated to CSF seem to play an important role for tracer entry into brain parenchyma. Access of substances to the entire brain extravascular compartment may potentially have large implications for new therapeutic and diagnostic approaches to neurological disease. Delayed tracer clearance from brain parenchyma in patients with iNPH dementia suggests that intrathecal contrast-enhanced MRI could be used to diagnose preclinical neurodegenerative disease.

## Methods

The study was prospective and observational, including consecutive patients with tentative CSF leakage and idiopathic intracranial hypotension and patients with iNPH who underwent MRI before and at several time points following intrathecal lumbar injection of the MRI contrast agent gadobutrol. They were prospectively enrolled from October 2015 to September 2016. Exclusion criteria were history of hypersensitive reactions to contrast agents, history of severe allergy reactions in general, evidence of renal dysfunction, and age <18 or >80 years as well as pregnancy or breastfeeding for women.

*REF subjects.* The individuals with idiopathic intracranial hypotension were referred to the Department of Neurosurgery, Oslo University Hospital — Rikshospitalet, from local neurological departments, based on clinical symptoms and imaging findings indicative of idiopathic intracranial hypotension. They were referred for clinical workup of suspected CSF leakage and underwent MRI with intrathecal gadobutrol, with the primary goal to define site of CSF leakage. These patients were recruited prospectively and consecutively in parallel with iNPH patients. Five of eight REF individuals (REF nos. 1, 2, 4, 5, and 6) have been reported in a previous study (13), though with another method of assessing CSF contrast enrichment and a limited selection of brain regions.

*Patients with iNPH dementia.* The iNPH patients were referred to the Department of Neurosurgery, Oslo University Hospital — Rikshospitalet, from local neurological departments, based on clinical symptoms and findings indicative of iNPH and imaging findings of ventriculomegaly. Within the Department of Neurosurgery, a clinical assessment was done, and clinical severity was graded based on a previously described NPH grading scale (77, 78). Patients were selected for CSF diversion surgery based on a combination of clinical symptoms and findings indicative of iNPH, imaging findings, comorbidity, and results of intracranial pressure monitoring, as previously described (77, 78). Four of nine iNPH subjects (iNPH nos. 1, 2, 3, and 4) have been reported in a previous study (13), though with another method of assessing CSF contrast enrichment and a limited selection of brain regions.

*MRI protocol.* We used a 3 Tesla Philips Ingenia MRI scanner (Philips Medical Systems) with equal imaging protocol settings at all time points to acquire sagittal 3D T1-weighted volume scans. The imaging parameters were as follows: repetition time, “shortest” (typically 5.1 ms); echo time, “shortest” (typically 2.3 ms); Flip angle, 8 degrees; field of view, 256 × 256 cm; and matrix, 256 × 256 pixels (reconstructed 512 × 512). We sampled 184 overcontiguous (overlapping) slices with 1-mm thickness, which was automatically reconstructed to 368 slices with 0.5-mm thickness. The total duration of each image acquisition was 6 minutes and 29 seconds. At each time point, imagining stacks were planned using an automated anatomy recognition protocol based on landmark detection in MRI data (SmartExam, Philips Medical Systems) to secure consistency and reproducibility of the MRI slice placement and orientation.

Before gadobutrol administration, we also scanned patients with a sagittal 3D FLAIR volume sequence, where the main imaging parameters were as follows: repetition time = 4,800 ms; echo time, “shortest” (typically 318 ms); inversion recovery time, 1,650 ms; field of view, 250 × 250 mm; and matrix, 250 × 250 pixels (reconstructed 512 × 512). We sampled 184 overcontiguous slices with 1-mm thickness, which was automatically reconstructed to 365 slices with 0.5-mm thickness.

*Intrathecal administration of gadobutrol.* After the precontrast MRI, which was acquired approximately 8 a.m., an interventional neuroradiologist performed x-ray guided lumbar puncture. Correct position of the syringe tip in the SAS was verified by CSF backflow from the puncture needle, and injecting of a small amount (typically 3 ml) of 270 mg I/ml iodixanol (Visipaque, GE Healthcare) confirmed unrestricted distribution of radiopaque contrast agent in the lumbar SAS. Thereafter, intrathecal injection of 0.5 ml of 1.0 mmol/ml gadobutrol (Gadovist, Bayer) was performed. After needle removal, the study subjects were

instructed to rotate themselves around the long axis of the body once before transportation back to the MRI suite, while remaining in the supine position. Supplemental Video 3 illustrates the distribution of CSF tracer within the CSF space following intrathecal administration.

*Postcontrast MRI acquisitions.* Consecutive, identical MRI acquisitions using the previously outlined MRI protocol parameters were performed as soon as possible after intrathecal gadobutrol administration (typically with approximately 10 minutes delay) and performed approximately every 10 minutes during the first hour after contrast agent injection. The study participants were thereafter instructed to remain supine in bed. One pillow under the head was allowed, allowing for 15-degree head elevation. Repeated, identical image acquisitions were then performed approximately every 2 hours after intrathecal gadobutrol administration until afternoon, at approximately 4 p.m. All transfer of study subjects between the neurosurgical department and the MRI suite, and between the bed and the MRI table, was performed by the hospital staff to allow for the patient to remain in the supine position. The final MRI scanning was performed next morning (approximately 24 hours after contrast agent injection). Patients and controls were allowed to move without any restrictions between the 4 p.m. examination at the end of day 1 and the 24-hour scan next morning.

While the MRI exams, for practical reasons, could not be obtained at identical time points for every study subject, all exams were categorized into the following time intervals: precontrast, 1–2 hours, 2–4 hours, 4–6 hours, 6–9 hours, 24 hours, 48 hours, and after 4 weeks.

*Image analysis.* The FreeSurfer software (version 6.0) (<http://surfer.nmr.mgh.harvard.edu/>) was used for segmentation, parcellation, and registration/alignment of the longitudinal data (Supplemental Figures 2 and 3). The segmentation and parcellation acquired from FreeSurfer were used to investigate the increase of T1 intensity due to CSF tracer. The methods are documented in a review (79). This includes removal of nonbrain tissue using a hybrid watershed/surface deformation procedure (80), automated Talairach transformation, and segmentation of the subcortical white matter and deep gray matter volumetric structures (including hippocampus, amygdala, caudate, putamen, and ventricles) (81, 82).

The MR images of each patient were used to create a median template registered to the baseline, a process has been previously described (83). Hence, for each patient, the MR images were registered to the corresponding template using a rigid transformation (83). The registrations were subsequently checked manually by LMV, and no significant errors were visible.

The T2 images (for all iNPH patients except 3) were also used for the segmentation with FreeSurfer. Additionally, the specification of large ventricles was added to the segmentation processes for the NPH patients.

The segmentation of 7 iNPH patients was edited due to segmentation errors. These editions were due to severe segmentation errors, such as mislabeling of ventricle volume as white matter and the inclusion of dura as part of the parenchyma; other minor errors were not considered. These corrections were automatic based on the patient T2 image, except in the case of 1 iNPH patient, which was done manually.

*Parameters derived from gadobutrol enhancement.* For each segmented area, we computed the median T1 signal unit for each time point. Further, we divided the median signal unit against the signal unit of a REF ROI placed within the posterior part of the superior sagittal sinus in axially reconstructed images from the same T1 volume scan (Supplemental Figure 4). We referred to the result of this as normalized T1 signal units; this process corrects for any baseline changes of image gray scale due to image scaling. Previous observations indicate no measurable enhancement of contrast agent at MRI in the REF location after intrathecal injection of gadobutrol at this concentration (13).

*CSF contrast enrichment and volume of brain region.* For REF and iNPH subjects, we determined Pearson correlation coefficients by comparing the percentage change in signal unit ratio after 24 hours and the volume of the specific brain region (white and gray matter and CSF of lateral ventricles). Volumes were computed by summation of the number of voxels of every subregion in the segmentation and multiplication of the result by the voxel size of 1.0 mm<sup>3</sup>.

*Statistics.* Categorical data are shown as the number of observations (percentage) and continuous data are shown as mean (SD) or mean (SEM), as appropriate. We estimated from the image analysis the mean response for each patient at 0 (precontrast), 1.5–2.0, 2–4, 4–6, 6–9, 24, and 48 hours and at 4 weeks follow-up. The repeated measurements were assessed with linear mixed models using a random intercept, robust SEM, and maximum likelihood estimation. Due to few observations, the results at 48 hours were omitted from the statistical model. Using a linear combination from the statistical model, we tested the difference between the REF and iNPH groups at the different points of follow-up.

For the statistical analysis, we used SPSS version 22 (IBM Corporation) or Stata/SE 15.0 (StataCorp LLX). Statistical significance was accepted at the 0.05 level (2-tailed).

*Study approval.* The Regional Committee for Medical and Health Research Ethics of Health, South East Region, Norway (2015/96); the Institutional Review Board of Oslo University Hospital (2015/1868); and the National Medicines Agency, Norway (15/04932-7) approved the study. The study participants were included after written and oral informed consent.

### Author contributions

GR, LMV, KAM, and PKE conceptualized and designed the study. GR, LMV, AMD, AHP, SASV, KEE, KAM, and PKE provided investigation and formal analysis. GR, KAM, and PKE supervised and administrated the study and wrote the original draft. GR, LMV, AMD, AHP, SASV, KEE, KAM, and PKE wrote, reviewed, and edited the manuscript. All authors (GR, LMV, AMD, AHP, SASV, KEE, KAM, and PKE) approved the final manuscript.

### Acknowledgments

We thank Øivind Gjertsen, Bård Nedregård, and Ruth Sletteberg from the Department of Radiology, Oslo University Hospital — Rikshospitalet, who performed the intrathecal gadobutrol injections in all study subjects. We also sincerely thank the Intervention Centre and Department of Neurosurgery at Oslo University Hospital — Rikshospitalet for providing valuable support with MR scanning and care for all study subjects throughout the study. Finally, we sincerely thank the Nursing Staff and Hydrocephalus Outward Clinic, Department of Neurosurgery Oslo University Hospital — Rikshospitalet, for care of all study subjects throughout the study.

Address correspondence to: Per K. Eide, Department of Neurosurgery, Oslo University Hospital — Rikshospitalet, Pb 4950 Nydalen, N-0424 Oslo, Norway. Phone: 47.2307.4321; Email: p.k.eide@medisin.uio.no or peide@ous-hf.no.

1. Wolak DJ, Thorne RG. Diffusion of macromolecules in the brain: implications for drug delivery. *Mol Pharm.* 2013;10(5):1492–1504.
2. Schlageter KE, Molnar P, Lapin GD, Groothuis DR. Microvessel organization and structure in experimental brain tumors: microvessel populations with distinctive structural and functional properties. *Microvasc Res.* 1999;58(3):312–328.
3. Pangalos MN, Schechter LE, Hurko O. Drug development for CNS disorders: strategies for balancing risk and reducing attrition. *Nat Rev Drug Discov.* 2007;6(7):521–532.
4. Finkel RS, et al. Treatment of infantile-onset spinal muscular atrophy with nusinersen: a phase 2, open-label, dose-escalation study. *Lancet.* 2016;388(10063):3017–3026.
5. Pizzo ME, et al. Intrathecal antibody distribution in the rat brain: surface diffusion, perivascular transport and osmotic enhancement of delivery. *J Physiol (Lond).* 2018;596(3):445–475.
6. Rennels ML, Gregory TF, Blaumanis OR, Fujimoto K, Grady PA. Evidence for a 'paravascular' fluid circulation in the mammalian central nervous system, provided by the rapid distribution of tracer protein throughout the brain from the subarachnoid space. *Brain Res.* 1985;326(1):47–63.
7. Iliff JJ, et al. A paravascular pathway facilitates CSF flow through the brain parenchyma and the clearance of interstitial solutes, including amyloid  $\beta$ . *Sci Transl Med.* 2012;4(147):147ra111.
8. Bedussi B, Almasian M, de Vos J, VanBavel E, Bakker EN. Paravascular spaces at the brain surface: Low resistance pathways for cerebrospinal fluid flow. *J Cereb Blood Flow Metab.* 2018;38(4):719–726.
9. Smith AJ, Yao X, Dix JA, Jin BJ, Verkman AS. Test of the 'glymphatic' hypothesis demonstrates diffusive and aquaporin-4-independent solute transport in rodent brain parenchyma. *Elife.* 2017;6:e27679.
10. Dobson H, et al. The perivascular pathways for influx of cerebrospinal fluid are most efficient in the midbrain. *Clin Sci.* 2017;131(22):2745–2752.
11. Lam MA, Hemley SJ, Najafi E, Vella NGF, Bilston LE, Stoodley MA. The ultrastructure of spinal cord perivascular spaces: Implications for the circulation of cerebrospinal fluid. *Sci Rep.* 2017;7(1):12924.
12. Eide PK, Ringstad G. MRI with intrathecal MRI gadolinium contrast medium administration: a possible method to assess glymphatic function in human brain. *Acta Radiol Open.* 2015;4(11):2058460115609635.
13. Ringstad G, Vatnehol SAS, Eide PK. Glymphatic MRI in idiopathic normal pressure hydrocephalus. *Brain.* 2017;140(10):2691–2705.
14. Iliff JJ, et al. Brain-wide pathway for waste clearance captured by contrast-enhanced MRI. *J Clin Invest.* 2013;123(3):1299–1309.
15. Carare RO, et al. Solutes, but not cells, drain from the brain parenchyma along basement membranes of capillaries and arteries: significance for cerebral amyloid angiopathy and neuroimmunology. *Neuropathol Appl Neurobiol.* 2008;34(2):131–144.
16. Morris AW, et al. Vascular basement membranes as pathways for the passage of fluid into and out of the brain. *Acta Neuropathol.* 2016;131(5):725–736.
17. Syková E, Nicholson C. Diffusion in brain extracellular space. *Physiol Rev.* 2008;88(4):1277–1340.
18. Iliff JJ, et al. Cerebral arterial pulsation drives paravascular CSF-interstitial fluid exchange in the murine brain. *J Neurosci.* 2013;33(46):18190–18199.

19. Zeppenfeld DM, et al. Association of perivascular localization of aquaporin-4 with cognition and Alzheimer disease in aging brains. *JAMA Neurol.* 2017;74(1):91–99.
20. Xia M, Yang L, Sun G, Qi S, Li B. Mechanism of depression as a risk factor in the development of Alzheimer's disease: the function of AQP4 and the glymphatic system. *Psychopharmacology (Berl).* 2017;234(3):365–379.
21. Iliff JJ, et al. Impairment of glymphatic pathway function promotes tau pathology after traumatic brain injury. *J Neurosci.* 2014;34(49):16180–16193.
22. Kress BT, et al. Impairment of paravascular clearance pathways in the aging brain. *Ann Neurol.* 2014;76(6):845–861.
23. Xie L, et al. Sleep drives metabolite clearance from the adult brain. *Science.* 2013;342(6156):373–377.
24. Ju YE, et al. Obstructive sleep apnea decreases central nervous system-derived proteins in the cerebrospinal fluid. *Ann Neurol.* 2016;80(1):154–159.
25. He XF, et al. Voluntary exercise promotes glymphatic clearance of amyloid beta and reduces the activation of astrocytes and microglia in aged mice. *Front Mol Neurosci.* 2017;10:144.
26. Jin BJ, Smith AJ, Verkman AS. Spatial model of convective solute transport in brain extracellular space does not support a “glymphatic” mechanism. *J Gen Physiol.* 2016;148(6):489–501.
27. Holter KE, et al. Interstitial solute transport in 3D reconstructed neuropil occurs by diffusion rather than bulk flow. *Proc Natl Acad Sci USA.* 2017;114(37):9894–9899.
28. Mestre H, et al. Aquaporin-4 dependent glymphatic solute transport in rodent brain. bioRxiv. <https://www.biorxiv.org/content/early/2017/11/09/216499>. Published November 9, 2017. Accessed June 18, 2018.
29. Thorne RG, Hrabětová S, Nicholson C. Diffusion of epidermal growth factor in rat brain extracellular space measured by integrative optical imaging. *J Neurophysiol.* 2004;92(6):3471–3481.
30. Nicholson C, Tao L. Hindered diffusion of high molecular weight compounds in brain extracellular microenvironment measured with integrative optical imaging. *Biophys J.* 1993;65(6):2277–2290.
31. Thorne RG, Nicholson C. In vivo diffusion analysis with quantum dots and dextrans predicts the width of brain extracellular space. *Proc Natl Acad Sci USA.* 2006;103(14):5567–5572.
32. WOOLLAM DH, MILLEN JW. The perivascular spaces of the mammalian central nervous system and their relation to the perineuronal and subarachnoid spaces. *J Anat.* 1955;89(2):193–200.
33. MILLEN JW, WOOLLAM DH. On the nature of the pia mater. *Brain.* 1961;84:514–520.
34. Hutchings M, Weller RO. Anatomical relationships of the pia mater to cerebral blood vessels in man. *J Neurosurg.* 1986;65(3):316–325.
35. Zhang ET, Inman CB, Weller RO. Interrelationships of the pia mater and the perivascular (Virchow-Robin) spaces in the human cerebrum. *J Anat.* 1990;170:111–123.
36. Pollock H, Hutchings M, Weller RO, Zhang ET. Perivascular spaces in the basal ganglia of the human brain: their relationship to lacunes. *J Anat.* 1997;191(Pt 3):337–346.
37. Engelhardt B, Vajkoczy P, Weller RO. The movers and shapers in immune privilege of the CNS. *Nat Immunol.* 2017;18(2):123–131.
38. Asgari M, de Zélécourt D, Kurtcuoglu V. Glymphatic solute transport does not require bulk flow. *Sci Rep.* 2016;6:38635.
39. Bedussi B, et al. Paravascular channels, cisterns, and the subarachnoid space in the rat brain: A single compartment with preferential pathways. *J Cereb Blood Flow Metab.* 2017;37(4):1374–1385.
40. Abbott NJ. Evidence for bulk flow of brain interstitial fluid: significance for physiology and pathology. *Neurochem Int.* 2004;45(4):545–552.
41. Rosenberg GA, Kyner WT, Estrada E. Bulk flow of brain interstitial fluid under normal and hyperosmolar conditions. *Am J Physiol.* 1980;238(1):F42–F49.
42. Hannocks MJ, et al. Molecular characterization of perivascular drainage pathways in the murine brain. *J Cereb Blood Flow Metab.* 2018;38(4):669–686.
43. Cserr HF. Physiology of the choroid plexus. *Physiol Rev.* 1971;51(2):273–311.
44. Cserr HF, Cooper DN, Suri PK, Patlak CS. Efflux of radiolabeled polyethylene glycols and albumin from rat brain. *Am J Physiol.* 1981;240(4):F319–F328.
45. Jiang Q, et al. Impairment of the glymphatic system after diabetes. *J Cereb Blood Flow Metab.* 2017;37(4):1326–1337.
46. Bakker EN, et al. Lymphatic clearance of the brain: perivascular, paravascular and significance for neurodegenerative diseases. *Cell Mol Neurobiol.* 2016;36(2):181–194.
47. Calias P, et al. CNS penetration of intrathecal-lumbar idursulfate in the monkey, dog and mouse: implications for neurological outcomes of lysosomal storage disorder. *PLoS ONE.* 2012;7(1):e30341.
48. Papisov MI, Belov VV, Gannon KS. Physiology of the intrathecal bolus: the leptomeningeal route for macromolecule and particle delivery to CNS. *Mol Pharm.* 2013;10(5):1522–1532.
49. Papisov MI, et al. Investigation of intrathecal transport of NPT002, a prospective therapeutic based on phage M13, in nonhuman primates. *Drug Deliv Transl Res.* 2012;2(3):210–221.
50. Brinker T, Stopa E, Morrison J, Klinge P. A new look at cerebrospinal fluid circulation. *Fluids Barriers CNS.* 2014;11:10.
51. Aspelund A, et al. A dural lymphatic vascular system that drains brain interstitial fluid and macromolecules. *J Exp Med.* 2015;212(7):991–999.
52. Louveau A, et al. Structural and functional features of central nervous system lymphatic vessels. *Nature.* 2015;523(7560):337–341.
53. Eide PK, Vatnehol SAS, Emblem KE, Ringstad G. Magnetic resonance imaging provides evidence of glymphatic drainage from human brain to cervical lymph nodes. *Sci Rep.* 2018;8(1):7194.
54. Ma Q, Ineichen BV, Detmar M, Proulx ST. Outflow of cerebrospinal fluid is predominantly through lymphatic vessels and is reduced in aged mice. *Nat Commun.* 2017;8(1):1434.
55. Pardridge WM. The blood-brain barrier: bottleneck in brain drug development. *NeuroRx.* 2005;2(1):3–14.
56. Bielekova B, et al. Intrathecal effects of daclizumab treatment of multiple sclerosis. *Neurology.* 2011;77(21):1877–1886.
57. Bottros MM, Christo PJ. Current perspectives on intrathecal drug delivery. *J Pain Res.* 2014;7:615–626.
58. Robert R, Wark KL. Engineered antibody approaches for Alzheimer's disease immunotherapy. *Arch Biochem Biophys.* 2012;526(2):132–138.

59. Kilsdonk ID, et al. Increased cortical grey matter lesion detection in multiple sclerosis with 7 T MRI: a post-mortem verification study. *Brain*. 2016;139(Pt 5):1472–1481.
60. Cuddapah VA, Robel S, Watkins S, Sontheimer H. A neurocentric perspective on glioma invasion. *Nat Rev Neurosci*. 2014;15(7):455–465.
61. Kanda T, Ishii K, Kawaguchi H, Kitajima K, Takenaka D. High signal intensity in the dentate nucleus and globus pallidus on unenhanced T1-weighted MR images: relationship with increasing cumulative dose of a gadolinium-based contrast material. *Radiology*. 2014;270(3):834–841.
62. Kanda T, Nakai Y, Hagiwara A, Oba H, Toyoda K, Furui S. Distribution and chemical forms of gadolinium in the brain: a review. *Br J Radiol*. 2017;90(1079):20170115.
63. Jost G, Frenzel T, Lohrke J, Lenhard DC, Naganawa S, Pietsch H. Penetration and distribution of gadolinium-based contrast agents into the cerebrospinal fluid in healthy rats: a potential pathway of entry into the brain tissue. *Eur Radiol*. 2017;27(7):2877–2885.
64. Radbruch A, et al. Pediatric brain: no increased signal intensity in the dentate nucleus on unenhanced T1-weighted MR images after consecutive exposure to a macrocyclic gadolinium-based contrast agent. *Radiology*. 2017;283(3):828–836.
65. Radbruch A, et al. No signal intensity increase in the dentate nucleus on unenhanced T1-weighted MR images after more than 20 serial injections of macrocyclic gadolinium-based contrast agents. *Radiology*. 2017;282(3):699–707.
66. Yang L, et al. Evaluating glymphatic pathway function utilizing clinically relevant intrathecal infusion of CSF tracer. *J Transl Med*. 2013;11:107.
67. Lowe J, Mirra SS, Hyman BT, Dickson DW. Chapter 14: Ageing and Dementia. In: Love S, Louis D, Ellison DW, eds. *Greenfield's Neuropathology*. Boca Raton, FL, USA: CRC Press; 2008:1031–1152.
68. Eide PK, Ringstad G. Delayed clearance of cerebrospinal fluid tracer from entorhinal cortex in idiopathic normal pressure hydrocephalus: A glymphatic magnetic resonance imaging study [published online ahead of print February 27, 2018]. *J Cereb Blood Flow Metab*. <https://doi.org/10.1177/0271678X18760974>.
69. Golomb J, et al. Alzheimer's disease comorbidity in normal pressure hydrocephalus: prevalence and shunt response. *J Neurol Neurosurg Psychiatry*. 2000;68(6):778–781.
70. Pennanen C, et al. Hippocampus and entorhinal cortex in mild cognitive impairment and early AD. *Neurobiol Aging*. 2004;25(3):303–310.
71. Israelsson H, et al. Vascular risk factors in INPH: A prospective case-control study (the INPH-CRasH study). *Neurology*. 2017;88(6):577–585.
72. de Calignon A, et al. Propagation of tau pathology in a model of early Alzheimer's disease. *Neuron*. 2012;73(4):685–697.
73. Eide PK, Hansson HA. Astroglial impaired aquaporin-4 dystrophin systems in idiopathic normal pressure hydrocephalus [published online ahead of print June 19, 2018]. *Neuropathol Appl Neurobiol*. <https://doi.org/10.1111/nan.12420>.
74. Amiry-Moghaddam M, et al. An alpha-syntrophin-dependent pool of AQP4 in astroglial end-feet confers bidirectional water flow between blood and brain. *Proc Natl Acad Sci USA*. 2003;100(4):2106–2111.
75. Heier LA, Bauer CJ, Schwartz L, Zimmerman RD, Morgello S, Deck MD. Large Virchow-Robin spaces: MR-clinical correlation. *AJNR Am J Neuroradiol*. 1989;10(5):929–936.
76. Mestre H, Kostrikov S, Mehta RI, Nedergaard M. Perivascular spaces, glymphatic dysfunction, and small vessel disease. *Clin Sci*. 2017;131(17):2257–2274.
77. Eide PK, Sorteberg W. Diagnostic intracranial pressure monitoring and surgical management in idiopathic normal pressure hydrocephalus: a 6-year review of 214 patients. *Neurosurgery*. 2010;66(1):80–91.
78. Eide PK, Sorteberg W. Outcome of surgery for idiopathic normal pressure hydrocephalus: role of preoperative static and pulsatile intracranial pressure. *World Neurosurg*. 2016;86:186–193.e1.
79. Fischl B. FreeSurfer. *Neuroimage*. 2012;62(2):774–781.
80. Ségonne F, et al. A hybrid approach to the skull stripping problem in MRI. *Neuroimage*. 2004;22(3):1060–1075.
81. Fischl B, et al. Whole brain segmentation: automated labeling of neuroanatomical structures in the human brain. *Neuron*. 2002;33(3):341–355.
82. Fischl B, et al. Sequence-independent segmentation of magnetic resonance images. *Neuroimage*. 2004;23 Suppl 1:S69–S84.
83. Reuter M, Schmansky NJ, Rosas HD, Fischl B. Within-subject template estimation for unbiased longitudinal image analysis. *Neuroimage*. 2012;61(4):1402–1418.

Paper II

# **Delayed clearance of cerebrospinal fluid tracer from choroid plexus in idiopathic normal pressure hydrocephalus**

**Per K. Eide, Lars M. Valnes, Are H. Pripp, Kent-Andre Mardal,  
Geir Ringstad**





# Delayed clearance of cerebrospinal fluid tracer from choroid plexus in idiopathic normal pressure hydrocephalus

Per Kristian Eide<sup>1,2</sup> , Lars Magnus Valnes<sup>3</sup>, Are Hugo Pripp<sup>4</sup>, Kent-Andre Mardal<sup>3,5</sup> and Geir Ringstad<sup>2,6</sup>

Journal of Cerebral Blood Flow & Metabolism  
0(0) 1–10  
© Author(s) 2019  
Article reuse guidelines:  
sagepub.com/journals-permissions  
DOI: 10.1177/0271678X19874790  
journals.sagepub.com/home/jcbfm



## Abstract

Impaired clearance of amyloid- $\beta$  from choroid plexus is one proposed mechanism behind amyloid deposition in Alzheimer's disease. The present study examined whether clearance from choroid plexus of a cerebrospinal fluid tracer, serving as a surrogate marker of a metabolic waste product, is altered in idiopathic normal pressure hydrocephalus (iNPH), one subtype of dementia. In a prospective observational study of close to healthy individuals (reference cohort; REF) and individuals with iNPH, we performed standardized T1-weighted magnetic resonance imaging scans before and through 24 h after intrathecal administration of a cerebrospinal fluid tracer (the magnetic resonance imaging contrast agent gadobutrol). Changes in normalized T1 signal within the choroid plexus and cerebrospinal fluid of lateral ventricles were quantified using FreeSurfer. The normalized T1 signal increased to maximum within choroid plexus and cerebrospinal fluid of lateral ventricles 6–9 h after intrathecal gadobutrol in both the REF and iNPH cohorts (enrichment phase). Peak difference in normalized T1 signals between REF and iNPH individuals occurred after 24 h (clearance phase). The results gave evidence for gadobutrol resorption from cerebrospinal fluid by choroid plexus, but with delay in iNPH patients. Whether choroid plexus has a role in iNPH pathogenesis in terms of delayed clearance of amyloid- $\beta$  remains to be shown.

## Keywords

Idiopathic normal pressure hydrocephalus, choroid plexus, cerebrospinal fluid, CSF tracer, clearance, magnetic resonance imaging, intrathecal contrast agents, glymphatic, humans

Received 21 December 2018; Revised 29 June 2019; Accepted 1 July 2019

## Introduction

The choroid plexus is a highly vascularized tissue located in the cerebral ventricles and has traditionally been considered a main source of cerebrospinal fluid (CSF) production, thereby being a driving force behind CSF bulk flow from the ventricular system to the subarachnoid space.<sup>1–3</sup> More recently, the choroid plexus has emerged as a vital structure for neuroprotection, neuro-immune regulation, and homeostasis of the brain's chemical milieu in a broad sense.<sup>4</sup> Experimental research also provides evidence that the choroid plexus has a function in clearance of amyloid- $\beta$  from the CSF, thus playing a role in the pathogenesis of Alzheimer's disease.<sup>5,6</sup>

The description of the cerebral glymphatic system in 2012<sup>7</sup> and the demonstration of dural lymphatic vessels in 2015<sup>8,9</sup> have facilitated renewed interest in the mechanisms behind clearance of metabolic waste solutes

from the brain. Impaired glymphatic<sup>7</sup> and lymphatic<sup>10</sup> function may both lead to impaired clearance of metabolic waste products, such as amyloid- $\beta$ , which in

<sup>1</sup>Department of Neurosurgery, Oslo University Hospital – Rikshospitalet, Oslo, Norway

<sup>2</sup>Faculty of Medicine, Institute of Clinical Medicine, University of Oslo, Oslo, Norway

<sup>3</sup>Department of Mathematics, University of Oslo, Oslo, Norway

<sup>4</sup>Oslo Centre of Biostatistics and Epidemiology, Research Support Services, Oslo University Hospital, Oslo, Norway

<sup>5</sup>Center for Biomedical Computing, Simula Research Laboratory, Lysaker, Norway

<sup>6</sup>Division of Radiology and Nuclear Medicine, Department of Radiology, Oslo University Hospital – Rikshospitalet, Oslo, Norway

### Corresponding author:

Per Kristian Eide, Department of Neurosurgery, Oslo University Hospital – Rikshospitalet, PB 4950 Nydalen, Oslo 0424, Norway.  
Email: peide@ous-hf.no

neuro-degenerative disease may accumulate and cause toxic damage to the brain. We previously demonstrated impaired glymphatic clearance of a magnetic resonance imaging (MRI) contrast agent (gadobutrol), serving as a CSF tracer in individuals with idiopathic normal pressure hydrocephalus (iNPH).<sup>11–13</sup> This CSF tracer is a molecule of size 604 Da that may serve as a surrogate marker of clearance of metabolic waste products from brain. The disease iNPH is characterized by dementia, gait ataxia, urinary incontinence and enlarged size of the cerebral ventricles,<sup>14</sup> and is characterized by neuro-degeneration and deposition of amyloid- $\beta$  in a significant proportion of the patients.<sup>15</sup> Another feature of this entity is the significant alterations of the CSF circulation. Therefore, CSF diversion surgery may provide sustained clinical improvement even though with some reduction of treatment effect over time.<sup>16</sup>

Given the important role of impaired cerebral clearance function for evolution of neuro-degeneration and dementia, characterizing the underlying mechanisms seems crucial. While glymphatic clearance seems reduced in iNPH patients,<sup>11–13</sup> it remains unknown whether or not clearance from the choroid plexus is reduced. In this present study, we for the first time utilized a CSF tracer for in vivo assessment of choroid plexus clearance function in references and a cohort with a dementia disease.

## Materials and methods

### *Patients and study design*

The study was approved by the Regional Committee for Medical and Health Research Ethics (REK) of Health Region South-East, Norway (2015/96), the Institutional Review Board of Oslo university hospital (2015/1868), and the National Medicines Agency (15/04932-7). The conduct of the study was governed by ethical standards according to the Helsinki Declaration of 1975 (and as revised in 1983). Study participants were included after written and oral informed consent.

A prospective and observational study design was used, and included consecutive patients with suspected CSF leakage, causative of idiopathic intracranial hypotension, and patients with iNPH. All individuals underwent MRI before and at several time points following intrathecal lumbar injection of the MRI contrast agent gadobutrol during a study period from October 2015 to September 2016.

Exclusion criteria were: History of hypersensitivity reactions to contrast agents, history of severe allergy reactions in general, evidence of renal dysfunction, pregnant or breastfeeding women, and age <18 or >80 years.

The reference (REF) subjects had a tentative diagnosis of idiopathic intracranial hypotension and were referred to the Department of Neurosurgery, Oslo University Hospital – Rikshospitalet, Oslo, Norway, from local neurological departments for clinical work-up of suspected CSF leakage. They underwent MRI with intrathecal gadobutrol with the primary indication to define site of CSF leakage, and were recruited prospectively and consecutively in parallel with iNPH patients. Patients with iNPH were referred to the Department of Neurosurgery, Oslo University Hospital – Rikshospitalet, Oslo, Norway, from local neurological departments, based on clinical symptoms and findings indicative of iNPH, and imaging findings of ventriculomegaly. Within the Department of Neurosurgery, clinical severity was graded based on a previously described NPH grading scale.<sup>16,17</sup> Patients were selected for shunt surgery based on assessing clinical symptoms and findings, imaging findings, co-morbidity, and results of intracranial pressure (ICP) monitoring, as previously described.<sup>16,17</sup>

### *MRI protocol*

A 3 Tesla Philips Ingenia MRI scanner (Philips Medical systems, Best, The Netherlands) with equal imaging protocol settings at all the time points was applied to acquire sagittal 3D T1-weighted volume scans with ultrafast gradient echo and preparation pulse (T1 FFE). The following imaging parameters were used: repetition time (TR) = “shortest” (typically 5.1 ms), echo time (TE) = “shortest” (typically 2.3 ms), inversion time = 853 ms, flip angle (FA) = 8 degrees, field of view (FOV) = 256 × 256 mm, and matrix = 256 × 256 pixels (reconstructed 512 × 512). We sampled 184 over-contiguous (overlapping) slices with 1 mm thickness, which was automatically reconstructed to 368 slices with 0.5 mm thickness.

In addition, a T2-weighted volume acquisition (T2 VISTA) was obtained with the following parameters: TR = 2500 ms, TE = 330 ms, FA = 90 degrees, FOV = 250 × 250 mm, matrix size = 252 × 250 pixels.

### *Intrathecal administration of gadobutrol*

After the pre-contrast MRI exam, an interventional neuroradiologist performed X-ray-guided lumbar puncture. Correct position of the syringe tip in the sub-arachnoid space was verified by CSF backflow from the puncture needle, and a small amount (typically 3 ml) of 270 mg I/ml iodixanol (Visipaque<sup>TM</sup>, GE Healthcare, USA) was injected to confirm unrestricted distribution of radiopaque contrast agent in the lumbar SAS. Then, 0.5 ml of 1.0 mmol/ml gadobutrol (Gadovist<sup>TM</sup>, Bayer Pharma AG, Berlin, Germany) was injected

intrathecally through the same needle. Following removal of the needle, the study subjects were instructed to rotate themselves around the long axis of the body once before transportation back to the MRI suite, while remaining in the supine position.

### Post-contrast MRI acquisitions

Consecutive, identical MRI acquisitions using the previously outlined MRI protocol parameters were performed after intrathecal gadobutrol administration. The study participants were instructed to remain supine in bed. One pillow under the head allowed for up to 15 degrees head elevation, and all transfer of study subjects between the neurosurgical department and the MRI suite, and between the bed and the MRI table, was performed by the hospital staff to help the patient remain in the supine position. Patients and controls were allowed to move without any restrictions between the 4 p.m. examination at the end of day one and the 24 h scan next morning.

While the MRI exams, for practical reasons, could not be obtained at identical time points for every study subject, all exams were categorized into the following time intervals: Pre-contrast, 1.5–2 h, 2–4 h, 4–6 h, 6–9 h, 24 h and 48 h.

### Image analysis

The FreeSurfer software (version 6.0) (<http://surfer.nmr.mgh.harvard.edu/>) was used for segmentation, parcellation, and registration/alignment of the longitudinal data. The segmentation and parcellation acquired from FreeSurfer were used to investigate the increase of T1 signal intensity due to CSF tracer enhancement. The methods are documented in a review.<sup>18</sup> In this study, we segmented the choroid plexus within the lateral ventricles as well as the CSF within the lateral ventricles.

The MR images of each patient were used to create a median template registered to the baseline, the process of which has been previously described.<sup>19</sup> Hence, for each patient, the MR images were registered to the corresponding template using a rigid transformation.<sup>19</sup> The registrations were subsequently checked manually by one of the co-authors (LMV), and no significant errors were visible.

The T2-weighted images (except for three iNPH patients who had no T2 images) were also used for the segmentation with FreeSurfer. Additionally, the specification of large ventricles was added to the segmentation processes for the iNPH patients.

The segmentation of seven iNPH patients was edited due to segmentation errors. The corrections were automatic based on the patients T2 image, except in one iNPH patient who had no T2 image, which required

manual editing to correct. Notably, the segmentation procedure did not impact the measured T1 signal units within the regions of interest (Supplementary Figure 1).

We determined the volume of choroid plexus and lateral ventricles, which was done by summarizing all voxels with the same segmentation. The corrections of the lateral ventricle volumes were done by labeling voxels in the near vicinity of the lateral ventricles, such as white matter and choroid plexus.

### T1 signal derived parameters

For each segmented area, the median T1 signal unit was computed for each time point. Further, the median signal unit was divided against the signal unit of a reference ROI placed within the posterior part of the superior sagittal sinus in axially reconstructed images from the same T1 volume scan. The ratio refers to as *normalized T1 signal units* and corrects for any baseline changes of image grey scale due to potential image scaling between single scans. Previous observations indicate no measureable enhancement of contrast agent at MRI in the reference location after intrathecal injection of gadobutrol at this concentration.<sup>11</sup>

### Estimation of CSF tracer concentration in lateral ventricle

The CSF tracer concentration (C) causes the T1 time to be shortened with the following relation

$$1/T1 = 1/T1(0) + R \times C \quad (1)$$

According to Lu et al.,<sup>20</sup> we assumed that  $T1(0) = 4300$  ms, and with reference to Rohrer et al.,<sup>21</sup> the relaxivity constant  $R = 3.2 \text{ mM}^{-1}\text{s}^{-1}$ . Since imaging parameters are the same for each T1 image, the T1-time becomes the only variable in the T1 protocol signal equation (equation (1)) in Gowland et al.<sup>22</sup> Then the concentration C is estimated by computing the normalized T1 signal increase from baseline that is needed to achieve the average signal increase.

### Statistical analysis

A linear mixed model for repeated measurements with a random intercept for study participant using maximum likelihood estimation with robust standard errors analyzed the effect of segment (i.e. choroid plexus versus CSF) and cohort (i.e. REF versus iNPH) on normalized T1 signal units at the time interval from 4 to 24 h. In addition to the main fixed effects of segment, cohort and age, the statistical model included an interaction term between segment and cohort. The interaction term assessed the modifying effect of cohort on normalized

T1 signal units in segment. Thus, a statistical significant interaction term could indicate that the mean difference in normalized T1 signal units between choroid plexus and CSF was different in the iNPH and REF cohort.

Statistical significance was accepted at the 0.05 level. The descriptive statistics was performed using the SPSS software version 20 (IBM Corporation, Armonk, NY), and the linear mixed model analysis was performed with Stata/SE 15.0 for Windows (Stata Corp LLC, College Station, TX).

## Results

The study included two cohorts of eight REF and nine iNPH patients, respectively (Table 1). The REF individuals had a tentative diagnosis of idiopathic intracranial hypotension due to CSF leakage, which was confirmed in 3/8 individuals. No CSF leakage was seen in 5/8 individuals, who we consider close to healthy. However, the patient cohorts differed in several respects (Table 1).

Table 2 presents measures of ventriculomegaly/CSF circulation failure (Evans index, callosal angle, and disproportionately enlarged subarachnoid space hydrocephalus, DESH), as well as volume of choroid plexus in lateral ventricle and lateral ventricular volume size in REF and iNPH individuals. We found no differences in volume of choroid plexus between patient cohorts, while volumes of CSF spaces were larger in the iNPH cohort (Table 2).

After intrathecal administration of the CSF tracer (i.e. MRI contrast agent), tracer propagated into the ventricular system and enriched the choroid plexus of both REF and iNPH individuals (Figure 1). This was, however, markedly more pronounced in iNPH than REF subjects. The changes in signal unit ratios within

choroid plexus of lateral ventricles and the CSF of lateral ventricles of the (a) REF and (b) iNPH cohorts are illustrated in Figure 2. For both locations, the tracer enrichment was more pronounced in the iNPH than in REF individuals (Figure 2). Moreover, Table 3 presents the percentage change in normalized T1 signal from before CSF tracer administration within choroid plexus and lateral ventricle of the REF and iNPH cohorts. While tracer enrichment within the lateral ventricle of REF individuals was close to significant ( $P=0.052$ ), the MRI signal increased significantly ( $P<0.001$ ) at the other locations (Table 3).

While a CSF leakage was verified in 3/8 REF patients, the presence of CSF leakage seemed not to impact the measured T1 signal units. We found no differences in normalized T1 signal units between those individuals with/without verified leakage at any time

**Table 2.** Radiological measures and volumes of cerebral ventricles and choroid plexus of REF and iNPH cohorts.

|                          | REF           | iNPH          | Significance |
|--------------------------|---------------|---------------|--------------|
| Evans index              | 0.30 ± 0.05   | 0.38 ± 0.04   | 0.001        |
| DESH (Y/N)               | 0/8           | 6/3           | ns           |
| Callosal angle (degrees) | 117.3 ± 14.3  | 76.3 ± 29.0   | 0.003        |
| Volume measures (ml)     |               |               |              |
| Choroid plexus           | 0.75 ± 0.22   | 0.88 ± 0.23   | ns           |
| CSF, lateral ventricle   | 14.83 ± 14.43 | 68.85 ± 18.52 | <0.001       |

Note: Categorical data presented as numbers; continuous data presented as mean ± standard deviation. Significant differences between groups were determined by Pearson Chi-square test for categorical data and by independent samples t-test for continuous data. CSF: cerebrospinal fluid; DESH: disproportionate enlargement of subarachnoid spaces hydrocephalus; iNPH: idiopathic normal pressure hydrocephalus; REF: reference patients.

**Table 1.** Demographic and clinical information about the REF and iNPH cohorts at the time MRI.

|  | REF         | iNPH        | Significance |
|--|-------------|-------------|--------------|
| N  | 8           | 9           |              |
| Sex (F/M)                                  | 6/2         | 1/8         | 0.008        |
| Age (years)                                | 38.4 ± 17.3 | 68.3 ± 9.5  | <0.001       |
| Symptoms reported by patient and/or family |             |             |              |
| Gait disturbance                           | 2 (25%)     | 9 (100%)    | 0.001        |
| Urinary incontinence                       | 0 (0%)      | 6 (67%)     | 0.004        |
| Cognitive impairment                       | 0 (0%)      | 8 (89%)     | <0.001       |
| Duration of symptoms (months)              | 42.4 ± 40.6 | 21.3 ± 10.4 | ns           |
| NPH score                                  | 15 (14–15)  | 13 (11–13)  | <0.001       |

Note: Categorical data presented as numbers; continuous data presented as mean ± standard deviation. Significant differences between groups were determined by Pearson Chi-square test for categorical data and by independent samples t-test for continuous data. iNPH: idiopathic normal pressure hydrocephalus; REF: reference patients.

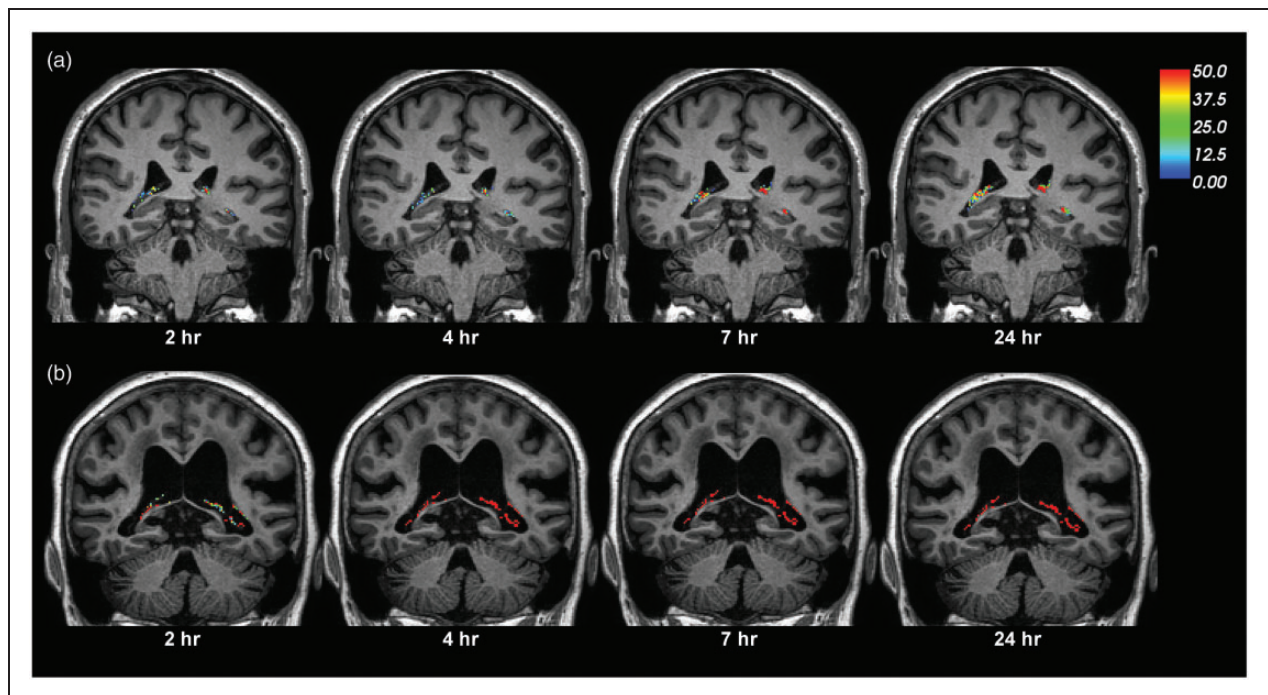


**Figure 1.** CSF tracer enrichment over time within the choroid plexus of a REF and an iNPH subject. The enrichment of CSF tracer within choroid plexus over time is shown for (a) a REF and (b) an iNPH subject. The percentage change in signal unit ratio is indicated at the color scale. Signal change within the CSF spaces is extracted in order to only present the percentage signal change within the choroid plexus.

point, neither the choroid plexus (lowest P-value 0.34) nor the CSF of the lateral ventricle (lowest P-value 0.21) (data not shown).

Figure 2 indicates that both choroid plexus enhancement and clearance of CSF tracer was different from REFs in the iNPH patients. Significant differences were seen during the enhancement phase after 4–6 and 6–9 h, as well as during the clearance phase at 24 h (Table 3). In particular, the most pronounced difference between REF and iNPH in choroid plexus was seen after 24 h, indicative of delayed clearance of CSF tracer from choroid plexus in iNPH disease.

Estimation of CSF tracer concentration and level also gave evidence for delayed clearance from lateral ventricle in iNPH. Table 4 presents the concentration and level of CSF tracer in lateral ventricle of iNPH and REF individuals, estimated according to equation (1). Concentrations for REF individuals were 0.0079 and 0.0022 mM after 6–9 and 24 h, respectively, while corresponding numbers in iNPH were 0.031 and 0.024 mM. As such, the reduction of tracer in lateral ventricles during this period in iNPH and REF was 23% and 72%, respectively, in a relative sense. On the other hand, in iNPH, the combination of increased volume of lateral ventricles and more pronounced CSF tracer enrichment resulted in increased absolute amounts of CSF tracer of 2.13 and 1.65  $\mu\text{mol}$  after 6–9 and 24 h,

respectively. In an absolute sense, the corresponding reduction in CSF tracer levels from 6–9 to 24 h after tracer administration was  $-0.48$  and  $-0.0057 \mu\text{mol}$ , respectively.

To further test whether the clearance of CSF tracer from choroid plexus per se was significantly different in iNPH, we determined the interaction term whether the iNPH diagnosis itself modified the CSF tracer enrichment within the choroid plexus and CSF of lateral ventricle. As indicated in Figure 3, a significant interaction term provided evidence for delayed clearance of CSF tracer from choroid plexus of iNPH compared to REF. Hence, in iNPH, enhancement was higher in CSF compared to choroid plexus, while in REF subjects, enhancement was higher in choroid plexus compared to CSF (Figure 3). Moreover, after correcting the interaction presented in Figure 3 for age-differences between REF and iNPH cohorts, the interaction term between REF and iNPH individuals remained significant. That is, the differences in CSF tracer enhancement within choroid plexus could not be explained by age-differences between REF and iNPH subjects.

## Discussion

The present data indicate that the MRI contrast agent gadobutrol is resorbed from CSF by the choroid plexus

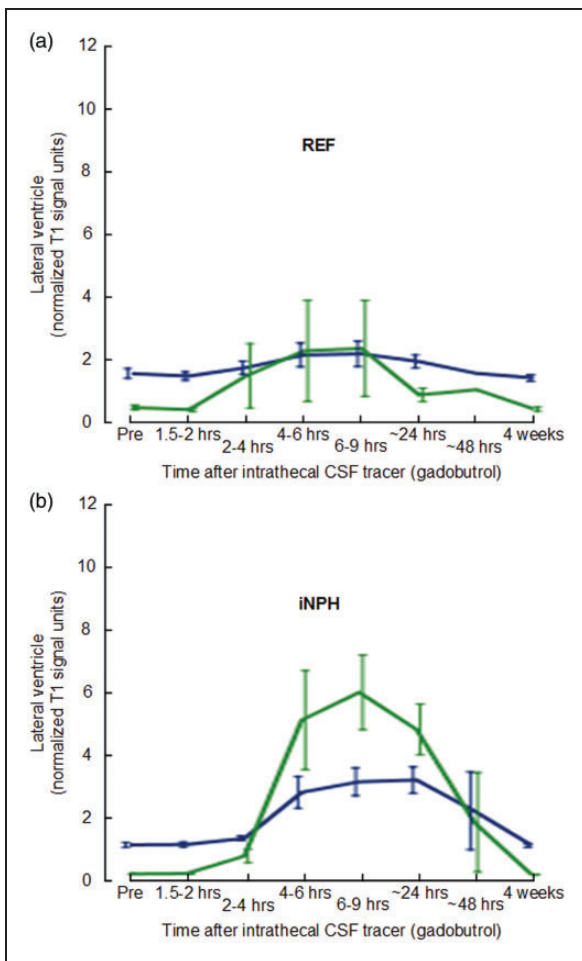


**Figure 2.** CSF tracer enrichment in choroid plexus and CSF of lateral ventricle in the REF and iNPH cohorts. Trend plots of signal unit ratios are shown for choroid plexus (blue lines) and CSF (green lines) within lateral ventricle of (a) REF and (b) iNPH subjects. The trend plots are shown as mean  $\pm$  standard error (SE). iNPH: idiopathic normal pressure hydrocephalus; REF: reference patients.

of the lateral ventricles. In iNPH patients, CSF enrichment of gadobutrol exceeded that of choroid plexus and was opposite to observations made in a cohort of healthy, or close to healthy, subjects. The findings suggest delayed clearance of molecules with similar features from choroid plexus in iNPH.

### Patients

The iNPH cohort was older than the reference cohort. An effect of age on results of CSF tracer clearance could therefore be anticipated. However, the differences in CSF tracer enrichment within choroid plexus and CSF of REF and iNPH individuals remained consistent after adjusting for age in the statistical analysis.

**Table 3.** Percentage change in signal unit ratios at various time points after intrathecal gadobutrol in REF and iNPH patients.

| Anatomical region<br>[FreeSurfer] | Time after i.th. gadobutrol |             |    |               |                 |                 |       |                 |       |                 |       |                | Overall<br>significance |    |         |
|-----------------------------------|-----------------------------|-------------|----|---------------|-----------------|-----------------|-------|-----------------|-------|-----------------|-------|----------------|-------------------------|----|---------|
|                                   | Enhancement phase           |             |    |               | Clearance phase |                 |       |                 |       |                 |       |                |                         |    |         |
|                                   | Group                       | 1.5–2h      | P  | 2–4h          | P               | 4–6h            | P     | 6–9h            | P     | 24h             | P     | 48h            |                         | P  | 4 weeks |
| Choroid plexus<br>[31, 63]        | REF                         | $-3 \pm 8$  | ns | $22 \pm 65$   | ns              | $57 \pm 107$    | 0.055 | $56 \pm 118$    | 0.019 | $24 \pm 34$     | 0.004 | 39             | $-8 \pm 15$             | ns | <0.001  |
|                                   | iNPH                        | $7 \pm 25$  |    | $21 \pm 26$   |                 | $162 \pm 127$   |       | $191 \pm 121$   |       | $185 \pm 112$   |       | $108 \pm 141$  | $0 \pm 18$              |    | <0.001  |
| CSF: lateral ventricle<br>[4, 43] | REF                         | $-10 \pm 8$ | ns | $342 \pm 957$ | ns              | $641 \pm 1415$  | 0.023 | $656 \pm 1438$  | 0.002 | $173 \pm 325$   | 0.001 | 228            | $-10 \pm 12$            | ns | 0.052   |
|                                   | iNPH                        | $11 \pm 28$ |    | $296 \pm 350$ |                 | $2598 \pm 2179$ |       | $3041 \pm 1808$ |       | $2272 \pm 1217$ |       | $869 \pm 1104$ | $-7 \pm 19$             |    | <0.001  |

Note: Continuous variables given as mean  $\pm$  standard deviation. P: Statistically significant differences determined by a linear mixed model for repeated measurements with time interval as fixed effect and a random intercept for patient. Numbers in brackets refer to FreeSurfer regions. iNPH: idiopathic normal pressure hydrocephalus; REF: reference patients.

**Table 4.** Estimated concentration of CSF tracer within lateral ventricles of REF and iNPH patients.

|  | REF     |        | iNPH   |       |
|--|---------|--------|--------|-------|
| Volume CSF, lateral ventricles (ml)                                  | 14.287  |        | 68.845 |       |
| Time after i.th. CSF tracer  | 6–9 h   | 24 h   | 6–9 h  | 24 h  |
| Signal increase from baseline (ratio)                                | 7.56    | 2.73   | 31.41  | 23.72 |
| Concentration, CSF tracer (mM)                                       | 0.0079  | 0.0022 | 0.031  | 0.024 |
| Change in concentration of CSF tracer from 6–9 h to 24 h (mM)        | –0.0057 |        | –0.007 |       |
| Level of CSF tracer ( $\mu\text{mol}$ )                              | 0.11    | 0.033  | 2.13   | 1.65  |
| Change in level of CSF tracer from 6–9 h to 24 h ( $\mu\text{mol}$ ) | –0.077  |        | –0.48  |       |

Note: The concentrations and levels of CSF tracer within the lateral ventricles were computed according to equation (1), see Materials and Methods section. CSF: cerebrospinal fluid; iNPH: idiopathic normal pressure hydrocephalus; REF: reference patients.

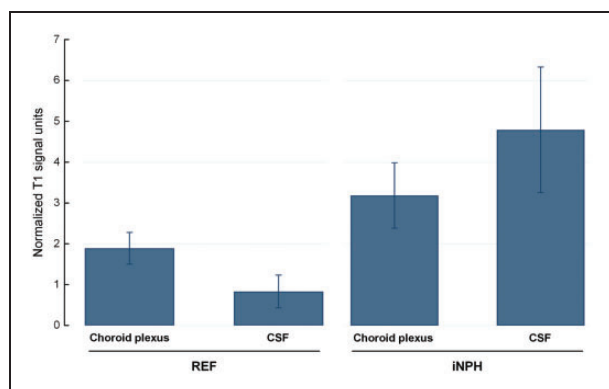


**Figure 3.** Analysis of interaction between signal unit ratio within CSF of lateral ventricle and choroid plexus in REF and iNPH cohorts at 24 h. The mean relative signal unit ratios within choroid plexus and CSF of the lateral ventricle are shown for the REF and iNPH subjects. Hence, the mean difference in normalized T1 signal unit between choroid plexus and CSF was different in the iNPH than REF subjects (interaction term,  $P < 0.001$ ), and the mean normalized T1 signal in choroid plexus was higher in the iNPH than REF subjects ( $P = 0.004$ ). The observation suggests impaired clearance of CSF tracer from choroid plexus of iNPH than REF individuals. Error bars are 95% CI.

iNPH: idiopathic normal pressure hydrocephalus; CSF: cerebrospinal fluid; REF: reference patients.

### Clearance of molecules from lateral ventricles

In the present study, the combined increased lateral ventricular volume and increased CSF tracer enrichment gave 19.4 and 50.0 times higher CSF tracer amounts in the lateral ventricles of iNPH patients, as compared with REF individuals after 6–9 and 24 h, respectively. The increased CSF tracer enhancement in lateral ventricles is related to CSF flow alterations in iNPH. We are currently investigating whether the retrograde aqueductal flow of CSF in iNPH patients, as previously reported by us,<sup>11,23</sup> explains the increase.

The present results extended previous data showing that during clearance phase (from 6–9 h to 24 h after CSF tracer administration), the relative reduction of CSF tracer concentration in lateral ventricles of iNPH was one third that of REF, but was much larger in absolute terms. Accordingly, while the relative reduction of CSF tracer was reduced in iNPH compared to REF individuals, the reduction of CSF tracer in absolute terms was higher in iNPH, due to the stronger enrichment of ventricular CSF tracer in this latter patient group. First, we assume that clearance of CSF tracer is both trans-ependymal and via choroid plexus. The trans-ependymal route is indicated by strong periventricular tracer enrichment in iNPH.<sup>11,12</sup> Second, since the CSF tracer is biologically inert, it may seem less likely that the choroid plexus has an active role in removing CSF tracer; rather, the relative reduction is by passive clearance of tracer.

### Clearance of molecules from choroid plexus

Several studies have demonstrated that reduced function of choroid plexus may be involved in disease processes causing neurodegeneration and Alzheimer's disease.<sup>4,6,24,25</sup> The present results provide in vivo evidence of reduced clearance of a molecule from choroid plexus of iNPH individuals. While tracer supply in CSF was higher in iNPH due to ventricular reflux, tracer enhancement in plexus was proportionally lower than in REF (Figure 3). In line with this assumption, experimental studies have shown reduced clearance of amyloid- $\beta$  from choroid plexus, suggesting a role in the pathogenesis of Alzheimer's disease.<sup>5,6</sup> We consider the CSF tracer used in this study as a surrogate marker of cerebral waste products in general, but how well the present CSF tracer depicts the behavior of soluble amyloid- $\beta$  has not been determined. It has already been established that the choroid plexus has a role in absorption of a range of other macromolecules from

CSF, for example, drugs such as penicillin and other endogenous and exogenous solutes.<sup>2</sup>

While this study provides evidence for transfer of an MRI contrast agent over the CSF–blood–barrier, transport of MRI contrast agents in the other direction, i.e. from blood to CSF, has recently been seen in several studies.<sup>26–28</sup> In rats, the concentration of MRI contrast agent in CSF was clearly higher than in blood after 4.5 h, and most likely leaked into ventricular CSF through the choroid plexus.<sup>28</sup> It may not seem reasonable that the highly vascularized choroid plexus should be a site for one-way traffic of substances from blood to CSF. Others have previously provided evidence of bidirectional exchange of substances from the choroid plexus,<sup>29–31</sup> i.e. both from the blood and into the CSF and from the CSF into the blood.

Absorption of CSF by the choroid plexus was first suggested almost one hundred years ago by Foley in 1921 (reviewed by McComb<sup>32</sup>) and later in hydrocephalic infants,<sup>31</sup> but has been contradicted by others.<sup>33</sup> A recent review<sup>34</sup> concluded that further investigation is required to establish the role of the choroid plexus in absorption of CSF.

### Role of choroid plexus in CSF production

It has traditionally been considered that the choroid plexus is the main source of CSF production,<sup>35–37</sup> while minor contributions to CSF production have been attributed to extra-ventricular sources such as the brain ependyma and parenchyma,<sup>32,38</sup> and spinal cord ependyma.<sup>39</sup> However, the traditional view of choroid plexus being the main producer of CSF has been heavily criticized.<sup>3,36,40</sup> It is now clear that the subarachnoid CSF compartment is continuous with the entire paravascular compartment of the brain and spinal cord not only in animals<sup>7,41–43</sup> but also in humans.<sup>12</sup> New insights of continuous bi-directional fluid exchange over the entire blood–brain barrier clearly render for extra-choroidal CSF production.<sup>36</sup>

The present observations of significantly increased enhancement and delayed clearance of CSF tracer might also be attributed to reduced CSF tracer washout due to reduced CSF production in choroid plexus of iNPH. Experimental data from ageing rats and humans with iNPH or Alzheimer's disease have shown reduced production of CSF from choroid plexus and impaired turnover of CSF.<sup>44</sup> After intrathecal administration of an MRI contrast agent as CSF tracer, clearance of the CSF tracer from CSF spaces was significantly reduced, indicative of reduced CSF turnover in iNPH.<sup>11–13</sup> The reduced CSF turnover within CSF spaces in iNPH was accompanied with delayed brain-wide clearance of CSF tracers that were interpreted as impaired glymphatic clearance,<sup>11,12</sup> and suggested a common pathway

behind iNPH and Alzheimer's dementia and explains why amyloid- $\beta$  deposits in brain tissue overlap significantly in these conditions.<sup>45</sup>

Others have reported that the function of choroid plexus changes during ageing and in CSF circulation failure.<sup>40</sup> The iNPH cohort in this study was significantly older than the REF group. Furthermore, reduced CSF production in iNPH might be associated with increased pulsatile ICP and to lesser extent, increased static ICP, which is characteristic of iNPH patients responding to CSF diversion surgery.<sup>17</sup> Several authors have previously reported that CSF production can be reduced as response to an increased ICP caused by hydrocephalus.<sup>46–48</sup>

A link between CSF production and glymphatic function is to be expected. Probably, a certain magnitude of CSF production is required to maintain sufficient CSF pressure to drive paravascular clearance pathways throughout the brain<sup>7,49,50</sup> and to drive lymphatic efflux of waste molecules from the cranio-spinal compartment.<sup>51</sup> This view is in contrast to the previous concept that CSF production is primarily required for mechanical protection of the brain and maintenance of the electrolytic environment and acid–base balance.<sup>52</sup>

### Limitations

It should be noted that different levels of CSF tracer enhancement do not directly reflect changes in the concentration levels of the CSF tracer. The present results do therefore not provide measures by absolute quantities, even though such quantities may be estimated according to equation (1). T1 maps might be used for absolute quantifications of CSF tracer in future studies.

While the choroid plexus is present in all cerebral ventricles, this study only examined choroid plexus in lateral ventricles. We would, however, expect results to be similar for all compartments.

### Conclusions

The present study indicates that the MRI contrast agent gadobutrol is absorbed by the choroid plexus when utilized as CSF tracer. In patients with iNPH, this CSF tracer enhanced more strongly and was cleared with slower rate, from choroid plexus as compared to in REF subjects. Delayed CSF clearance of brain metabolites through choroid plexus may be instrumental for neurodegeneration in iNPH dementia.

### Funding

The author(s) received no financial support for the research, authorship, and/or publication of this article.

## Acknowledgements

We thank Dr. Øivind Gjertsen, Dr. Bård Nedregaard and Dr. Ruth Sletteberg from the Department of Radiology, Oslo University Hospital – Rikshospitalet, who performed the intrathecal gadobutrol injections in all study subjects. We also sincerely thank the Intervention Centre and Department of Neurosurgery at the Oslo University Hospital – Rikshospitalet for providing valuable support with MR scanning and care-taking of all study subjects throughout the study. Finally, we sincerely thank the Nurse Staff and Hydrocephalus outward clinic, Department of Neurosurgery, Oslo University Hospital – Rikshospitalet for care-taking of all study subjects throughout the study.

## Declaration of conflicting interests

The author(s) declared no potential conflicts of interest with respect to the research, authorship, and/or publication of this article.

## Authors' contributions

Conceptualization and design: PKE, LMV, KAM, GR. Investigation, formal analysis and visualization: PKE, LMV, KAM, GR. Supervision, Administration and writing – original draft: PKE, GR. Statistical analysis: AHP. Writing, review and editing: PKE, LMV, AHP, KAM, GR. All authors (PKE, LMV, AHP, KAM, GR) approved the final version of the article. Correspondence and material requests: PKE.

## ORCID iD

Per Kristian Eide  <https://orcid.org/0000-0001-6881-9280>

## Supplemental material

Supplemental material for this paper can be found at the journal website: <http://journals.sagepub.com/home/jcb>

## References

- Praetorius J. Water and solute secretion by the choroid plexus. *Pflugers Arch* 2007; 454: 1–18.
- Spector R, Keep RF, Robert Snodgrass S, et al. A balanced view of choroid plexus structure and function: focus on adult humans. *Exp Neurol* 2015; 267: 78–86.
- Oreskovic D, Rados M and Klarica M. Role of choroid plexus in cerebrospinal fluid hydrodynamics. *Neuroscience* 2017; 354: 69–87.
- Gherzi-Egea JF, Strazielle N, Catala M, et al. Molecular anatomy and functions of the choroidal blood-cerebrospinal fluid barrier in health and disease. *Acta Neuropathol* 2018; 135: 337–361.
- Crossgrove JS, Li GJ and Zheng W. The choroid plexus removes beta-amyloid from brain cerebrospinal fluid. *Exp Biol Med* 2005; 230: 771–776.
- Serot JM, Zmudka J and Jouanny P. A possible role for CSF turnover and choroid plexus in the pathogenesis of late onset Alzheimer's disease. *J Alzheimer's Dis* 2012; 30: 17–26.
- Iliff JJ, Wang M, Liao Y, et al. A paravascular pathway facilitates CSF flow through the brain parenchyma and the clearance of interstitial solutes, including amyloid beta. *Sci Transl Med* 2012; 4: 147ra111.
- Louveau A, Smirnov I, Keyes TJ, et al. Structural and functional features of central nervous system lymphatic vessels. *Nature* 2015; 523: 337–341.
- Aspelund A, Antila S, Proulx ST, et al. A dural lymphatic vascular system that drains brain interstitial fluid and macromolecules. *J Exp Med* 2015; 212: 991–999.
- Da Mesquita S, Louveau A, Vaccari A, et al. Functional aspects of meningeal lymphatics in ageing and Alzheimer's disease. *Nature* 2018; 560: 185–191.
- Ringstad G, Vatnehol SAS and Eide PK. Glymphatic MRI in idiopathic normal pressure hydrocephalus. *Brain* 2017; 140: 2691–2705.
- Ringstad G, Valnes LM, Dale AM, et al. Brain-wide glymphatic enhancement and clearance in humans assessed with MRI. *JCI Insight* 2018; 3: 1–16.
- Eide PK and Ringstad G. Delayed clearance of cerebrospinal fluid tracer from entorhinal cortex in idiopathic normal pressure hydrocephalus: a glymphatic magnetic resonance imaging study. *J Cereb Blood Flow Metab* 2019; 39: 1355–1368.
- Malm J and Eklund A. Idiopathic normal pressure hydrocephalus. *Pract Neurol* 2006; 6: 14–27.
- Leinonen V, Koivisto AM, Savolainen S, et al. Amyloid and TAU proteins in cortical brain biopsy and Alzheimer's disease. *Ann Neurol* 2010; 68: 446–453.
- Eide PK and Sorteberg W. Outcome of surgery for idiopathic normal pressure hydrocephalus: role of preoperative static and pulsatile intracranial pressure. *World Neurosurg* 2016; 86: 186–193.e181.
- Eide PK and Sorteberg W. Diagnostic intracranial pressure monitoring and surgical management in idiopathic normal pressure hydrocephalus: a 6-year review of 214 patients. *Neurosurgery* 2010; 66: 80–91.
- Fischl B. FreeSurfer. *Neuroimage* 2012; 62: 774–781.
- Reuter M, Schmansky NJ, Rosas HD, et al. Within-subject template estimation for unbiased longitudinal image analysis. *Neuroimage* 2012; 61: 1402–1418.
- Lu H, Nagae-Poetscher LM, Golay X, et al. Routine clinical brain MRI sequences for use at 3.0 Tesla. *J Magn Reson Imaging* 2005; 22: 13–22.
- Rohrer M, Bauer H, Mintorovitch J, et al. Comparison of magnetic properties of MRI contrast media solutions at different magnetic field strengths. *Invest Radiol* 2005; 40: 715–724.
- Gowland PA and Leach MO. Fast and accurate measurements of T1 using a multi-readout single inversion-recovery sequence. *Magn Reson Med* 1992; 26: 79–88.
- Lindstrom EK, Ringstad G, Mardal KA, et al. Cerebrospinal fluid volumetric net flow rate and direction in idiopathic normal pressure hydrocephalus. *NeuroImage Clin* 2018; 20: 731–741.
- Gonzalez-Marrero I, Gimenez-Llort L, Johanson CE, et al. Choroid plexus dysfunction impairs beta-amyloid clearance in a triple transgenic mouse model of Alzheimer's disease. *Front Cell Neurosci* 2015; 9: 17.

25. Krzyzanowska A and Carro E. Pathological alteration in the choroid plexus of Alzheimer's disease: implication for new therapy approaches. *Front Pharmacol* 2012; 3: 75.
26. Berger F, Kubik-Huch RA, Niemann T, et al. Gadolinium distribution in cerebrospinal fluid after administration of a gadolinium-based MR contrast agent in humans. *Radiology* 2018; 288: 703–709.
27. Nehra AK, McDonald RJ, Bluhm AM, et al. Accumulation of gadolinium in human cerebrospinal fluid after gadobutrol-enhanced MR imaging: a prospective observational cohort study. *Radiology* 2018; 288: 416–423.
28. Jost G, Frenzel T, Lohrke J, et al. Penetration and distribution of gadolinium-based contrast agents into the cerebrospinal fluid in healthy rats: a potential pathway of entry into the brain tissue. *Eur Radiol* 2017; 27: 2877–2885.
29. Dichiro G. Movement of the cerebrospinal fluid in human beings. *Nature* 1964; 204: 290–291.
30. Hassin GB. Notes on the nature and origin of the cerebrospinal fluid. *J Nerv Ment Dis* 1924; 59: 113–121.
31. Milhorat TH, Mosher MB, Hammock MK, et al. Evidence for choroid-plexus absorption in hydrocephalus. *N Engl J Med* 1970; 283: 286–289.
32. McComb JG. Recent research into the nature of cerebrospinal fluid formation and absorption. *J Neurosurg* 1983; 59: 369–383.
33. Eisenberg HM, McLennan JE and Welch K. Ventricular perfusion in cats with kaolin-induced hydrocephalus. *J Neurosurg* 1974; 41: 20–28.
34. Hladky SB and Barrand MA. Mechanisms of fluid movement into, through and out of the brain: evaluation of the evidence. *Fluids Barriers CNS* 2014; 11: 26.
35. Spector R, Robert Snodgrass S and Johanson CE. A balanced view of the cerebrospinal fluid composition and functions: focus on adult humans. *Exp Neurol* 2015; 273: 57–68.
36. Brinker T, Stopa E, Morrison J, et al. A new look at cerebrospinal fluid circulation. *Fluids Barriers CNS* 2014; 11: 10.
37. Cushing HW. The third circulation and its channels. In: *Studies in intracranial physiology & surgery: the third circulation, the hypophysics, the gliomas*. Oxford: H. Milford, Oxford University Press, 1925, pp.1–51.
38. Igarashi H, Tsujita M, Kwee IL, et al. Water influx into cerebrospinal fluid is primarily controlled by aquaporin-4, not by aquaporin-1: 170 JJVCPE MRI study in knockout mice. *Neuroreport* 2014; 25: 39–43.
39. Sonnenberg H, Solomon S and Frazier DT. Sodium and chloride movement into the central canal of cat spinal cord. *Proc Soc Exp Biol Med* 1967; 124: 1316–1320.
40. Trillo-Contreras JL, Ramírez-Lorca R, Hiraldo-González L, et al. Combined effects of aquaporin-4 and hypoxia produce age-related hydrocephalus. *Biochim Biophys Acta (BBA) – Mol Basis Dis* 2018; 1864: 3515–3526.
41. Bedussi B, van der Wel NN, de Vos J, et al. Paravascular channels, cisterns, and the subarachnoid space in the rat brain: a single compartment with preferential pathways. *J Cereb Blood Flow Metab* 2017; 37: 1374–1385.
42. Rennels ML, Gregory TF, Blaumanis OR, et al. Evidence for a 'paravascular' fluid circulation in the mammalian central nervous system, provided by the rapid distribution of tracer protein throughout the brain from the subarachnoid space. *Brain Res* 1985; 326: 47–63.
43. Lam MA, Hemley SJ, Najafi E, et al. The ultrastructure of spinal cord perivascular spaces: implications for the circulation of cerebrospinal fluid. *Sci Rep* 2017; 7: 12924.
44. Johanson CE, Duncan JA 3rd, Klinge PM, et al. Multiplicity of cerebrospinal fluid functions: new challenges in health and disease. *Cerebrospinal Fluid Res* 2008; 5: 10.
45. Golomb J, Wisoff J, Miller DC, et al. Alzheimer's disease comorbidity in normal pressure hydrocephalus: prevalence and shunt response. *J Neurol Neurosurg Psychiatry* 2000; 68: 778–781.
46. Tulassay T, Khoor A, Bald M, et al. Cerebrospinal fluid concentrations of atrial natriuretic peptide in children. *Acta Paediatr Hung* 1990; 30: 201–207.
47. Silverberg GD, Huhn S, Jaffe RA, et al. Downregulation of cerebrospinal fluid production in patients with chronic hydrocephalus. *J Neurosurg* 2002; 97: 1271–1275.
48. Johanson CE, Szymdynger-Chodobska J, Chodobski A, et al. Altered formation and bulk absorption of cerebrospinal fluid in FGF-2-induced hydrocephalus. *Am J Physiol* 1999; 277: R263–R271.
49. Plog BA, Dashnaw ML, Hitomi E, et al. Biomarkers of traumatic injury are transported from brain to blood via the glymphatic system. *J Neurosci* 2015; 35: 518–526.
50. Lundgaard I, Lu ML, Yang E, et al. Glymphatic clearance controls state-dependent changes in brain lactate concentration. *J Cereb Blood Flow Metab* 2017; 37: 2112–2124.
51. Ma Q, Ineichen BV, Detmar M, et al. Outflow of cerebrospinal fluid is predominantly through lymphatic vessels and is reduced in aged mice. *Nat Commun* 2017; 8: 1434.
52. Tumani H, Huss A and Bachhuber F. The cerebrospinal fluid and barriers – anatomic and physiologic considerations. In: de Vries LS and Glass HC (eds) *Handbook of clinical neurology*. Amsterdam: Elsevier, 2018, pp.21–32.

Book excerpt III

# **An introduction to basic meshing and mathematical modeling for the human brain**

**Kent-Andre Mardal, Marie E. Rognes, Travis B. Thompson,  
Lars M. Valnes**





Paper IV

# **Can diffusion alone explain brain-wide distribution of CSF tracers within 24 hours?**

**Lars Magnus Valnes, Sebastian K. Mitusch, Geir Ringstad,  
Per K. Eide, Simon W. Funke, Kent-Andre Mardal.**

